Stony Brook University

OFFICIAL COPY

The official electronic file of this thesis or dissertation is maintained by the University Libraries on behalf of The Graduate School at Stony Brook University.

© All Rights Reserved by Author.

Engineering Interface and Analysis in Orthopedic Surgery: Resection of Bone Tumors and Reconstruction using Biomimetic Implants

A Dissertation Presented
by
Carlos Gabriel Helguero Alcivar

to
The Graduate School
in Partial Fulfillment of the
Requirements
for the Degree of

Doctor of Philosophy
in
Mechanical Engineering

Stony Brook University
August 2016

Stony Brook University

The Graduate School

Carlos Gabriel Helguero Alcivar

We, the dissertation committee for the above candidate for the
Doctor of Philosophy degree,
hereby recommend acceptance of this dissertation.

Dr. Imin Kao, Advisor
Mechanical Engineering, SUNY at Stony Brook

Dr. Jeffrey Ge
Mechanical Engineering, SUNY at Stony Brook

Dr. Nilanjan Chakraborty
Mechanical Engineering, SUNY at Stony Brook

Dr. Fazel Khan
Department of Orthopedics, SUNY at Stony Brook

Dr. Srinivas N. Pentyala
Mechanical Engineering, SUNY at Stony Brook

Dr. David E. Komatsu
Department of Orthopedics, SUNY at Stony Brook

This dissertation is accepted by the Graduate School

Nancy Goroff
Interim Dean of the Graduate School

Abstract of the Dissertation

Engineering Interface and Analysis in Orthopedic Surgery: Resection of Bone Tumors and Reconstruction using Biomimetic Implants

by

Carlos Gabriel Helguero Alcivar

Doctor of Philosophy

in

Mechanical Engineering

Stony Brook University

2016

As healthcare grows more advanced, the next step is an individualized approach to patient care. Skeletal tumor resection provides complex challenges for surgeons. The goal of providing an accurate wide resection in sarcomas from preoperative plans while trying to preserve as much functionality remains a difficult task. We propose to leverage new developments in 3-D printing, computer aided design (CAD), and finite element analysis (FEA) to design and manufacture personalized cutting guides in order to increase the accuracy of childhood bone cancer resections, minimize post-resection fracture risk, and maximize allograft osteointegration. On the other side, after proper resection, successful reconstruction of the defect left in the bone is the next step to complete the surgical procedure. Recent technological advancements in three-dimensional (3D) printing have opened many possibilities for bone engineering. 3D printing is one of the best techniques for custom design of synthetic bone because it is highly specific to the implantable structure. Synthetic bone scaffolds have been used to replace diminished bone stock, aid in fracture repair, and assist in the integration of orthopedic implants with native bone. The best bone scaffolds should be able to withstand heavy loads and allow for osteoconductivity. However, current 3D

printing bone technologies can create either hard inert bone structures that are structurally compatible but functionally inert, or fragile soft structures that have osteoconductive properties but are extremely weak in structure. We present a novel technique to create artificial bone that can mimic natural bone. Our work is guided by two main goals: 1) Increase the quality of life for patients by precisely removing the minimum amount of healthy tissue without compromising the surgeons ability to remove the entire tumor; 2) Provide a biomimetic and biocompatible implant with an optimal fit.

Table of Contents

List of Figures **ix**

List of Tables **xii**

List of Abbreviations **xiv**

Acknowledgments **xv**

1 Introduction and Literature Review 1

1.1 Introduction and background: bone tumor resection and reconstruction . . . 1

1.2 Bioprinting . . . 3

1.3 Preview and outline for the following chapters . . . 5

1.4 Literature survey . . . 6

1.4.1 Customized guides of surgery . . . 6

1.4.2 Bone tissue regeneration using 3D printing . . . 7

1.4.3 Previous use of digital image processing in medicine . . . 8

1.5 Glossary . . . 9

2 Bone Tumor Resection Using 3D-Printed Customized Cutting Guides 12

2.1 Introduction . . . 12

2.2 Reverse engineering: from CT scan to 3D-printed cutting guide . . . 17

2.3 Parameters of the cutting guide and cutting path . . . 20

2.3.1 Straight cutting path vs. tapered cutting path 22
2.3.2 Calculating the compression force using FEA 23
2.3.3 FEA for tapered cutting path 27
2.4 Testing accuracy of cutting guide in comparison with current resection technique 29
2.4.1 Experimental study 32
2.4.2 Discussion 39
2.5 Summary 40

3 Kinematic Modeling and Error Analysis for the Positioning of Cutting-Guide 41
3.1 Introduction 41
3.2 Setup of the coordinate frames 42
3.3 Positioning process and restrictions in the operating room 44
3.4 Kinematic modeling and error analysis 45
3.5 Experimental Study: Improving accuracy by accounting for soft tissue . . . 51
3.5.1 Experimental setup and procedure 51
3.5.2 Calculate rotations 54
3.5.3 Calculate the $\boldsymbol{X}$ and $\boldsymbol{Z}$ translations 54
3.5.4 The $\boldsymbol{Y}$ translation 57
3.6 Results of experimental study 57
3.6.1 Results of rotation 59
3.6.2 Results of translation 60
3.6.3 Results of the yaw angle 62
3.7 Revisit the kinematic modeling 62
3.7.1 Behavior of the error vector according to kinematic model 63
3.7.2 Estimation of error vector based on experiments 66
3.7.3 Discussion 68
3.8 Summary 68

4 Intraoperative Technique to Accurately Position Cutting Guides 70

4.1 Introduction and justification 70

4.2 Digital image processing technique to quantify accuracy of cutting guide positioning 71

4.2.1 Defining a digital image 71

4.2.2 Digital image processing and boundary tracing 72

4.3 Experimental Study 76

4.3.1 Experimental setup 78

4.3.2 Experimental procedure 78

4.4 Experimental results 81

4.5 Comparison of results and discussions 83

4.5.1 Discussion 85

4.6 Summary 85

5 Bone Reconstruction Using Biomimetic Implants 87

5.1 Introduction and justification 87

5.2 Designing process of 3D-printed ABS scaffolds using bone's trabecular pattern 88

5.3 Cellular growth on 3D-printed ABS scaffolds: preliminary studies 90

5.3.1 Protocol for cell-seeding scaffolds 91

5.4 Depositioning of 3D-printed scaffolds with cellular bone matrix 93

5.4.1 Protocol for inducing cellular bone-matrix formation on 3D-printed scaffolds 94

5.5 Evidence of succesfull seeding and osteogenesis: staining and imaging . . . 95

5.6 Evaluation of CRFP effect on bone formation regulators 95

5.6.1 Preparing cell extracts for immunoblot studies 98

5.6.2 Immunoblotting 99

5.7 Summary 99

6 Mechanical Properties of Biomimetic Scaffolds 102

6.1 Introduction 102

6.2 Testing anisotropy of scaffolds 103

6.3 Compression test overview 105

6.4 Test setup 107

6.5 Results 107

6.6 Discussion 112

6.7 Summary 114

7 Concluding Remarks 116

8 Proposed Future Work 117

8.1 Resection using 3D-printed cutting guides 117

8.2 Reconstruction using biomimetic implants 118

Bibliography 120

List of Figures

1.1 Methods for tumor resection 4

1.2 Bony features of the femur 10

2.1 Metaphysis of the distal femur with osteosarcoma 14

2.2 Contact interface between bone and implant 16

2.3 Workflow for cutting guide fabrication 18

2.4 3D representation of femur edited in Geomagic 19

2.5 Cutting guide design in Solidworks 20

2.6 Superior ridge or articular cartilage sketched on cutting guide 21

2.7 Comparison between tapered and straight cutting paths 22

2.8 Analysis of forces acting on human leg 24

2.9 Free body diagram of femur to calculate internal compression force 26

2.10 Interest points for FEA and tapered cut angle variation 27

2.11 Disposition of elements for FEA 29

2.12 FEA: results of the edge *ab* 30

2.13 FEA: results of the edge *ac* 31

2.14 Cadaveric resection: experimental setup 34

2.15 Ilustration of normal vectors to estimate deviation from pre-operative plan . 35

2.16 Planes defined to obtain normal vectors orientations 36

2.17 Qualitative assessment of implant fitting 38

3.1 Coordinate frames used in the kinematic modeling 43
3.2 Cutting guide positioning process 44
3.3 Cutting guide as a rigid body, having 6 degrees of freedom in the space . . 46
3.4 Definition of error vector and error zone 49
3.5 Error zone as an aid to plan the cutting path during design phase of cutting guides 50
3.6 Different types of cutting guides used in positioning experiment 52
3.7 Different surface conditions of bones for positioning experiment 53
3.8 Calculating rotations of cutting guide after positioning using CT-scans . . . 55
3.9 Calculating the X and Z translations of cutting guide before and after the placement of the guide on the surface of the bone, using CT-scans and Steinmann pins holes 56
3.10 Translation of cutting guide along Y axis 58
3.11 Magnitude of error vector with respect to cutting guide rotation: Fixing rotations in zero 64
3.12 Trayectory of T' for different rotations: Fixing rotations in zero 65
3.13 Magnitude of error vector with respect to cutting guide rotation: Fixing rotations in average values 65
3.14 Trayectory of T' for different rotations: Fixing rotations in average values . 67
3.15 Cutting path trayectory changes after accounting for error vector 67

4.1 The concept of a digital gray-scale image 72
4.2 The use of markers in the cutting guide to record its position 73
4.3 Digital image processing steps for marker extraction 75
4.4 Boundary tracing to detect contour of circular marker placed on guide . . . 75
4.5 Marker detection in cutting guides using image processing 77
4.6 Distal line of capsular reflection on femur 79
4.7 Experimental setup. Validation of digital image processing technique 80

4.8 Coding labels and references used in image processing experiment 82

5.1 Flowchart for Biomimetic Implants Project 88
5.2 Designing process of Trabecular Scaffolds 89
5.3 CAD editing of trabecular scaffolds 89
5.4 Evolution of scaffold design 90
5.5 Cell seeding protocol 92
5.6 Treatment of MC3T3 cells with osteogenic inducers 94
5.7 Microscopy results over treated scaffolds 96
5.8 Mineralization results using Alizarin red stain 96
5.9 Bovine serum albumim standard curve with BIORAD protein assay 98
5.10 Protein expression experimental results 100

6.1 Simplified mechanical model of springs to calculate stiffness of scaffolds . 103
6.2 Testing anisotropy of 3D-printed scaffolds 104
6.3 Relationship between bone and scaffold axis of compression 104
6.4 Compression test: experimental setup 108
6.5 Compression test results: Flat vs. Trabecular scaffolds compressed through different axis 110
6.6 Compression test results for different axis of compression for either flat or trabecular scaffolds 111
6.7 Compression test results: treated vs untreated scaffolds 113

List of Tables

2.1 Parameters in FEA 28

2.2 Comparative results of implant fit in which absolute values of the differences between θ and θ' are presented as well as mean angles for each plane **1**, **2**, and **3** 39

3.1 Mean and standard deviation (SD) of the errors of rotation after positioning on smooth surface of the bone (*cf.* Figure 3.7*a*). All values are in degrees. . 59

3.2 Mean and standard deviation (SD) of the errors of rotation after positioning on tissue-covered surface of the bone (*cf.* Figure 3.7*b*). All values are in degrees. 60

3.3 Influence of soft tissue in positioning errors; showing the average of the mean values of the rotational errors for different type of guides 61

3.4 Mean and standard deviation (SD) of the errors in translation after positioning on smooth surface of the bone (*cf.* Figure 3.7*a*). All values are in *mm*. 61

3.5 Mean value and standard deviation (SD) of the errors in translation after positioning on the tissue-covered surface of the bone (*cf.* Figure 3.7*b*). All values are in *mm*. 62

3.6 Comparison of results of rotational error in the yaw direction using the approach depicted in Figure 3.8(*b*) vs. the procedure presented in Figure 3.9. All values are in degrees. 63

4.1 The mean and standard deviation (SD) of α, β and γ of the cutting guide after positioning, calculated using the image processing and boundary tracing algorithm; all values are in degrees 82
4.2 The mean and standard deviation (SD) of the translational errors of cutting guides after positioning, calculated with the image processing and boundary tracing algorithm; All values are in *mm* 83
4.3 Comparing values of rotational errors obtained by processing CT-Scan medical images versus still pictures; values are in degrees 84
4.4 Comparing values for translational errors obtained by processing CT-Scan medical images versus still pictures; values are in *mm* 84

6.1 Measures of scaffolds used in ISO 604 compression test. All values in *mm* . 105
6.2 Number of scpecimens per anisotropy testing approach 106
6.3 Compression test results: Flat vs Trabecular scaffolds. Average values for σ_M and E_c for each axis of compression. Standard deviation values are shown in parenthesis. Values in MPa 109
6.4 Compression test results: treated vs untreated scaffolds. Standard deviation values are shown in parenthesis. Values in MPa 112

List of Abbreviations

Abbreviation	Description
CAD	Computer Aided Design
FEA	Finite Element Analysis
OR	Operating Room
FDA	US Food and Drug Administration
CT Scan	Computed Tomography Scan
MRI	Magnetic Resonance Imaging
MEM	Minimum Essential Media
FBS	Fetal Bovine Serum
BMP-7	Bone Morphogenic Peptide-7
TGF	Transforming Growth Factor
OPN	Osteopontin
BSA	Bovine Serum Albumim

Acknowledgements

After all these years of research I can think of so many people that have walked next to me during this journey. First and foremost, I would like to deeply thank my advisor, Professor Imin Kao, for his guidance through this research. His patience and hard work inspired me day after day and his insights and intuition regarding our research have made my experience at Stony Brook an enrichment process.

I would also like to express my gratitud to my co-advisors Dr. Fazel Khan, Dr. Srinivas Pentyala and Dr. David Komatsu. Working with them everyday has been a great blessing as I have learned from their vast experience. I can proudly say they are among my friends now.

It is my pleasure to acknowledge the members of my committee, Prof. Jeffrey Ge and Prof. Nilanjan Chakraborty for their thoughtful comments and suggestions about my research.

The road to the Ph.D. has been colored by the company of my friends and colleagues in the Manufacturing and Automation Lab. We have shared nothing but good moments full of hard work and laughs.

I cannot forget my family in Ecuador, my brother Manolo and my sister Carmen, who has always been supporting me from overseas. They have share everymoment of my years of study at Stony Brook. My mother Zulema, who has always had time to listen about my triumphs and defeats, sharing them with me and providing nothing but pure love. My father Manuel, who is the responsible of seeding the idea of getting a Ph.D. in my mind, I am here because of him, he is the light of my path, my role model, my hero forever.

Last but not least, I would like to greatly and deeply thank the support of my wife, Carolina. I cannot think of going through these years without her, encouranging me everyday, sharing my tears and laughs, working together during endless hours through the night and watching our sons Gabriel and Carlos growing. This is 100% mine and 100% hers.

Chapter 1

Introduction and Literature Review

1.1 Introduction and background: bone tumor resection and reconstruction

Researchers in medicine and engineering have worked closely to solve complex challenges in surgery. Specifically, Computer Aided Design (CAD) and three-dimensional (3D) printing have been widely used, in combination with medical imaging, to provide robust solutions in the customization and implant-design area. Our aim is to aid medical doctors to: (*i*) accurately reproduce a pre-operative plan for osteosarcoma (a type of cancerous bone tumor, likely to appear during childhood) resection, and (*ii*) reconstruct the defect left in bone after the surgical procedure by introducing a bioprinting technique for implants creation. Our ultimate purpose is to increase the accuracy of childhood bone cancer resection, minimize post-resection fracture risk, and maximize allograft osteointegration.

Previous studies have shown that standard protocols for tumor resection are far less accurate than computerized and cutting-guide based protocols [1]. In order to maintain safe margins using current resection procedures, surgeons must rely on imprecise landmarks and the use of inaccurate measuring techniques. The most common method currently utilized by surgeons to reconstruct intercalary defects of bones involves predominantly 'freehand' techniques. For a cadaver structural allograft bone reconstruction, the surgeon gradually whittles down a piece of allograft bone to fit a given defect; whereas, for a customized

endoprosthetic implant reconstruction the surgeon tries to make the host bone defect the appropriate dimensions so as to allow the fit of the custom pre-manufactured implant.

The imprecision arising from current procedures can have serious consequence for the patient. For example, if the surgeon mistakenly cuts through the tumor, the cancer is more likely to spread, which drastically increases mortality. In contrast, if too much bone and adjacent tissue is removed, more complex and less durable reconstructions are resulted. Consequently, quality of life can greatly suffer due to the necessity for multiple revision surgeries throughout the patient's life. During resection, the sacrifice of critical anatomical structures (such as joint surfaces) and failures of the reconstruction construct, such as endoproshtetic loosening or non-union/fracture of allograft reconstructions can result in lifelong morbidity for patients [2] [3]. This dissertation is guided by three main goals based on the factors mentioned above:

(1) Increase the quality of life for patients by removing the minimum amount of healthy tissue without compromising the surgeon's ability to remove the entire tumor,

(2) Provide an allograft with an optimal fit, and

(3) Promote allograft integration into host bone by optimizing the local loading environment.

In order to improve the accuracy in pre-operative plan reproduction and fit a custom implant into host bone after resection of a bone tumor, we propose to leverage new development in 3D printing, CAD, and finite element analysis (FEA) to design and manufacture custom generated 3D-printed cutting guides [4] to change the way these types or surgery are planned nowadays. As depicted in Figure 1.1, current resection techniques will likely end in complicated procedures like a total knee arthroplasty. Instead, our proposed method focuses on minimizing the deleterious impact on patient's quality of life. With advances in

medical imaging and 3D printing, customized surgical cutting guides can be the future of tumor resections or any surgery requiring extremely high accuracy.

1.2 Bioprinting

The medical community has been interested in artificial bones that can mimic natural bone for a long time. Recent technological advancements in 3D printing have opened many possibilities for bone engineering. 3D printing is one of the best techniques for custom design of synthetic bone because it is highly specific and independent. Synthetic bone scaffolds have been used to replace diminished bone stock, aid in fracture repair, and to assists in the integration of orthopedic implants to the native bone [5].

The 3D bio-printing is being used in regenerative medicine to address the need for tissues and organs, particularly bone. Implantable bone technology has a tremendous potential in health care. It is estimated that current global orthopedic implant market is $34.9 billion and the market is expected to grow at a rate of 4.9% over the next five years [6]. The aging population and increased risk for osteoporosis, osteoarthritis, bone injuries, and obesity are significant contributors to orthopedic implants.

Biocompatible implants will help decrease morbidity associated with implant surgeries. Demand for 3D-printed bone will increase in the coming years as the structures can be tailored for patient specific and defect specific clinical needs. Currently, artificial bone is being used to treat segmental defects, particularly for trauma and oncology patients. Several materials are available to treat segmental defects, but all are encumbered by significant problems that limit their efficacy [7]. While numerous materials are clinically available, or under development to treat segmental defects, each carries a unique constellation of benefits and drawbacks that forces the surgeon to compromise some aspect of patient care upon selection. They can resorb too quickly, are prone to prolonged drainage issues, can be hard to keep in place, and despite offering some structural support in compression, are generally brittle [8].

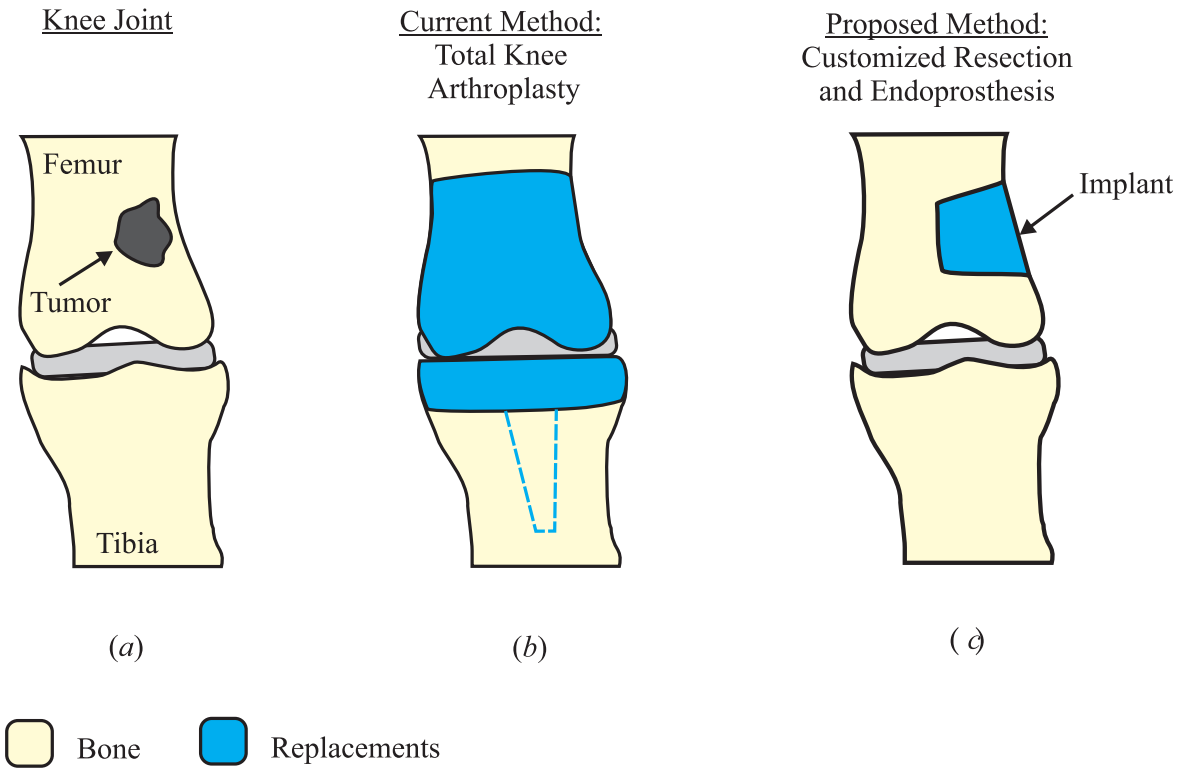

Figure 1.1: Methods for tumor resection: (*a*) Hypothetical tumor on distal femur, (*b*) Current resection technique and, (*c*) Proposed method using customized guides

To overcome these difficulties and to create a biomimetic and biocompatible artificial bone, we propose to create implantable scaffolds seeded with bone producing cells that are enhanced by osteogenic agents and perform *in vitro* and *in vivo* preclinical studies. Results from these studies will aid in creating custom made artificial 3D bone implants that can be used clinically.

1.3 Preview and outline for the following chapters

In Chapter 2, an extensive explanation about the reverse engineering technique used to create 3D-printed cutting guides is presented. The road from medical images (DICOM files) to the physical guides is explained step by step in order to give the reader a broader understanding of our work. After that, justification of the chosen geometry of the cutting path is presented. Finite Element Analysis (FEA) was used to illustrate that a tapered cutting path responds better under typical gait forces and stresses, as compared to a straight cutting path. Finally, a series of experiments are considered to assess the accuracy of a given resection plan using 3D-printed guides in comparison to typical 'freehand' techniques used in the operative room. The results of the experiments are displayed showing that, indeed, cutting guides help surgeons to replicate a pre-operative plan more accurately.

In Chapter 3, a simplified kinematic model is presented in order to predict the accuracy of the positioning process of the cutting guide over bone's surface. It is our belief that most of the error found in the results of the experiments in Chapter 2 comes from the process of positioning the guide on top of the bone. In order to predict the error that this process carries to the cutting operation, a typical homogeneous transformation matrix is utilized in the analysis, based on the given coordinates and axis of reference. Towards validation of the proposed model, four different guide-designs are inspected in a series of experiments in which subjects are asked to position the guides over model femurs. Surfaces of the models were ornamented with modeling clay mimicking typical soft tissue found over bone's surface.

In Chapter 4, an image processing technique to extract information about the error in positioning of the cutting guide during surgery is presented. The aim is to create a fast, affordable and easy-to-use technique that will help surgeons to accurately position the cutting guide prior resection.

In Chapters 5 and 6, the reconstruction of the defect left in bone after resection is appraised. To overcome this, we introduce the design process of 3D-printed scaffolds in which the trabeculae pattern of the bone is replicated by using the same reverse engineering techniques introduced in Chapter 2. Later, the cellular integration into these scaffolds is evaluated with a series of experiments, showing credible evidence of it. After cell seeding, osteogenesis is induced on treated scaffolds and the process associated is explained in details. Finally, the mechanical properties of these hybrids scaffolds (inorganic material + cells) are investigated and results are reported.

1.4 Literature survey

1.4.1 Customized guides of surgery

The customized cutting guides have been used to improve reproduction of a certain pre-operative plan. For instance, Khan *et al.* [4] have reported the use of resection 3D-printed guides for bone tumor resection in which, reverse engineering software was used to obtain 3D digital images of bones. Six pairs of cadaveric femurs were resected in two groups: one using the guide-assisted technique and the other using the traditional manual technique. To compare the accuracy of resection, a best-fit planes technique was used. Results favored the guide-assisted technique.

Wong *et al.* [9] reported the design of a customized 3D-printed guide based on the surface of the bone obtained with computer tomography (CT). Their guide was designed to perform straight cuts on the distal and proximal part of a femur. A case study was reported in which the guide was used for a bone resection and posterior prosthetic reconstruction. Cartiaux [10] described a simulated resection using patient-specific 3D-printed instruments

that worked as cutting guides. In this case, a comparison between 'freehand,' computer navigation and guide resections was performed with results favoring the use of guides. Kunz *et al.* [11] created a 3D-printed guide design for hip resurfacing. In this case, guides were merely used as drill templates. Again, reverse engineering was used to mimic femoral head surface.

1.4.2 Bone tissue regeneration using 3D printing

The field of bone tissue regeneration has been widely and extensively investigated by several researches around the world. The introduction of 3D-printing has opened a vast number of options regarding bone-shape resembling scaffold creation and implant design. Hutmacher *et al.* [12] evaluated the mechanical properties and cell cultural response of polycaprolactone (PCL) scaffolds fabricated with fused deposition modeling (a 3D-printing technique). Material was selected based on its favorable thermoplastic characteristics. Cellular response was positive leading to conclude that PCL scaffolds are suitable for bone tissue engineering. Tellis *et al.* [13] proposed design scaffolds with trabecular patterns. In this case, polybutylene terephthalate was used. Mechanical testing was also reported and a comparison between dry scaffolds and scaffolds soaked in NaCl solution was presented. However, no cell seeding was explored.

Pati *et al.* [14] go further and induce mineralization and extracellular matrix formation in their PCL scaffolds. Evidence in the form of medical imaging and staining was presented; however, no report on mechanical properties of their scaffolds is shown. A very interesting approach in Pati's research is their *in vivo* regeneration attempt. In order to do so, scaffolds were implanted on the calvaria of a rat. Defects filled with the threated scaffolds showed a better closure than non-treated scaffolds showing the biocompatibility of these procedures.

1.4.3 Previous use of digital image processing in medicine

Image processing techniques have been studied extensively for several years. Currently, the vast majority of diagnoses made by medical doctors rely on their experience and expertise. Most of the time, an exhaustive visual analysis of a medical image (*i.e.* X-rays, CT Scans, MRI, etc) is enough for the doctor to diagnose a patient and to design a treatment plan. However, special cases sometimes require further and assisted analysis [26]. Also, the fatigue of doctor after several working hours may be alleviated by automating certain processes of diagnosis.

Many studies and recent advances of image analysis in medical imaging are med possible due to the benefits of computational analysis of medical images. Some commonly used applications [27] were presented in interpretation and diagnosis of *mammographies* often suffers from false negatives and false positives results. This is mainly related to the difficulty of interpreting healthy or unhealthy landmarks on the images, due to doctors' lack of experience or even fatigue. Segmentation, one of the most common image processing technique, is widely used in mammographies to classify and analyze suspicious abnormalities prior to doctor's final diagnosis [28].

Another field where image processing has been used with remarkable results is *bone strength and osteoporosis*. Bone mineral density is the key parameter to diagnose osteoporosis, and one of the main factors to measure it is the loss of trabecular bone. Resolutions of CT scanners are not capable of accurately quantify such loss. However, image processing techniques such as fractal dimension [29], overcome this problem and returns a reliable result.

Other medical problems such as *vascular tortuosity* [30], *scoliosis* [31] and *osteoarthitis* [32] have also been solved by means of digital image processing. In fact, image processing has become the standard to help doctors in diagnosing these pathologies.

This survey suggests that mathematical modeling for processing medical images is widely used and accepted among the medical community. Our approach is somewhat dif-

ferent as we are not using typical medical images such as X-rays or CT scans that require special instruments to obtain. On the contrary, we are proposing the use of typical snapshots of the patients anatomy in the OR, taken with a regular amateur camera of a smartphone.

1.5 Glossary

Some medical terms pertaining to research and presentation in this dissertation are briefly described in this section.

Allograft: the transplant of an organ or tissue from one individual to another of the same species with a different genotype

Endoprosthesis: a synthetic insert or implant

Femur Bone: the bone of the leg that is closest to the center of the body, as illustrated in Figure 1.2(*a*)

Distal: situated away from the center of the body or any point of reference; applied to the extremes of a given bone, as illustrated in Figure 1.2(*b*)

Proximal: situated near to the center of the body or any point of reference; applied to the extremes of a given bone, as illustrated in Figure 1.2(*b*)

Metaphysis: the wide part at the end of the shaft of a long bone, as illustrated in Figure 1.2(*b*)

Epiphysis: the end of a long bone, usually wider than the shaft, as illustrated in Figure 1.2(*b*)

Stress Shielding: the reduction of bone density due to removal of normal stress from the bone by an implant

Osteotomy: a surgical resection where a bone is cut to a desire shape

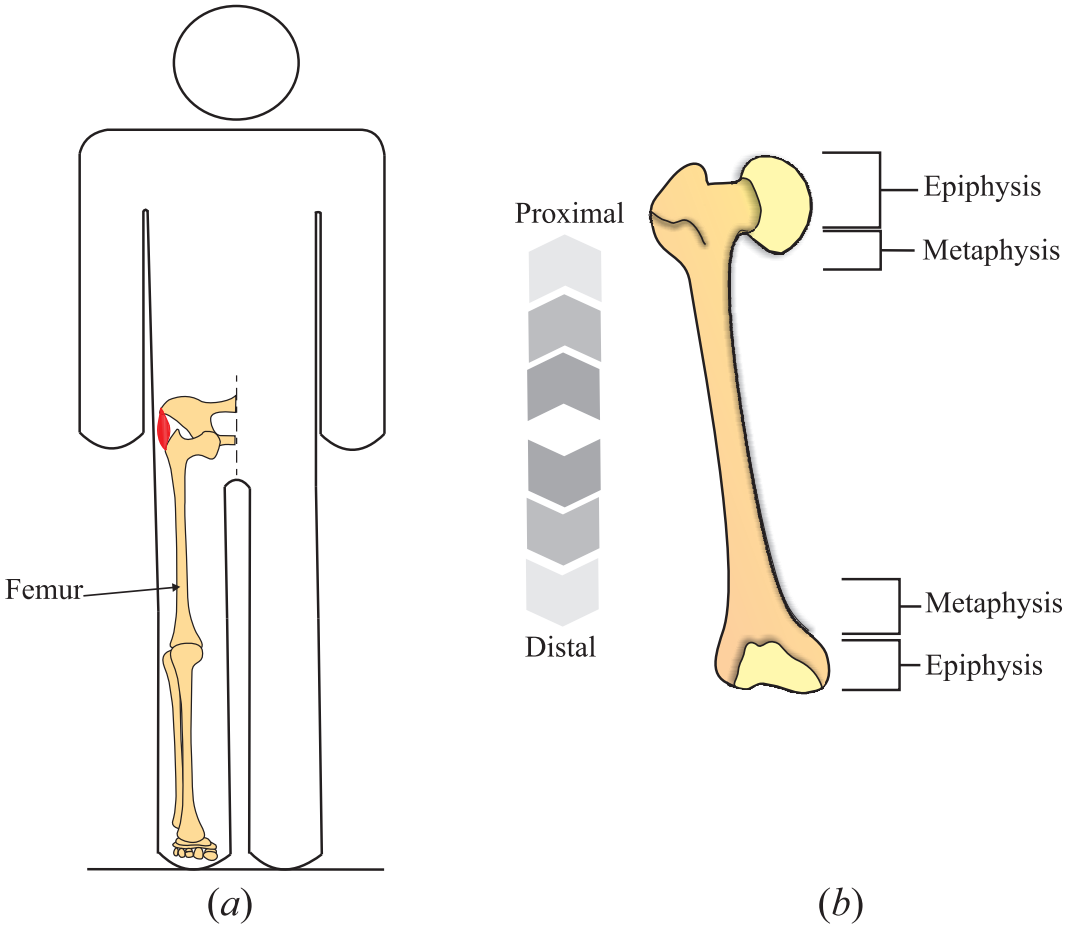

Figure 1.2: Bony features of the femur (*a*) location of the femur in the human body, and (*b*) parts of femur

DICOM: acronym for Digital Imaging and Communication in Medicin, refering to the standard for medical imaging file system and communication protocol

Negative margins resection: a clean or clear tumor resection in which no cancer cells are seen at the outer edge of the removed tissue

Osteoblast: a type of cell that have the capability of produce, or synthesize, bone

Cell differentiation: the process in which a cell changes from one type to another, commonly going from a less specialized type to a more specialized type

Osteogenesis: the process of producing new bone material by osteoblasts

F-actin: a multi-functional protein essential for important cellular functions as mobility and contraction of cells during differentiation

DAPI (4',6-diamidino-2-phenylindole): a fluorescent stain used in microscopy, specially to dye cell nucleus

Chapter 2

Bone Tumor Resection Using 3D-Printed Customized Cutting Guides

2.1 Introduction

Thirty years ago, almost all patients presented with osteosarcoma or Ewings sarcoma, the two most common primary bone cancers in children, were treated with an amputation. Furthermore, approximately 80% of patients died of their disease even with this aggressive treatment [15]. In stark contrast, more than 90% of children presented with osteosarcoma or Ewings sarcoma today can have a limb-salvage operation (i.e., avoiding amputation). With appropriate adjuvant chemotherapy, close to 80% will be cured of their disease [16, 17]. While these advances are a great success story, the fact that most of these children go on to live a full life, with a reconstructed limb, has posed new challenges. The surgical treatment of childhood bone cancer is 'wide resection,' where the entire tumor plus the surrounding 'reactive zone' is removed *en bloc* [18]. The skeletal defect left after tumor removal must be reconstructed, which is done either with metal ('endoprosthesis') or with a block of cadaveric bone ('structural bone allograft'). In general, the more extensive the resection, the more extensive the reconstruction. With existing technology, however, current methods of limb reconstruction simply do not have the durability to last a lifetime. Thus, most patients are forced to undergo multiple subsequent surgeries, sometimes even ultimately an amputation (of the originally salvaged limb). One of the great remaining

challenges in the treatment of childhood bone cancers is to develop methods that will (1) safely limit the amount of normal bone and soft tissue that must be removed during the cancer resection, and (2) provide a durable, high-functioning reconstruction that has a small risk of failure.

A wide resection of a primary bone cancer that preserves as much normal bone and soft tissue as possible would be expected to produce a better functional result for the patient. As a discrete example, consider Figure 2.1 where a tumor is growing in the metaphysis of the distal femur, which is the most common site for osteosarcoma. Although it may be clear from pre-operative imaging that a particular tumor does not enter the epiphysis (the joint-containing portion of the bone), the surgeon is typically reluctant to perform an epiphysis-sparing procedure (green line) because limitations in current intraoperative technology place the surgeon at high risk for inadvertently cutting into tumor and spilling malignant cells. Instead, a distal femoral resection is performed (red line), removing the entire epiphysis including the entire articular surface and all proximal ligament attachments. This aggressive resection requires a joint-replacing reconstruction, either a distal femoral metal joint replacement or an osteoarticular (cartilage plus bone) allograft. The problem is that the former reconstruction is likely to loosen within the patients lifetime and requires several revision procedures; whereas, the latter reconstruction is likely to develop degeneration of the allograft articular surface and also require multiple extensive revision procedures beginning with total knee replacement.

In stark contrast, if the surgeon was able to reliably spare the epiphysis, the entire joint surface could be spared along with attached ligament origins. Reconstruction would then simply consists of an intercalary allograft placed into the metaphyseal defect. If union is achieved and fracture does not occur, this reconstruction has a real potential to provide a lifelong reconstructive solution for the patient. Analogous arguments can be made in other common sites of presentation of primary bone sarcomas. Thus, in many instances, the child with primary bone cancer would be expected to benefit greatly from techniques

Figure 2.1: Metaphysis of the distal femur with osteosarcoma.

that would afford maximum preservation of normal bone and soft tissues. Intraoperative surgical tools and technology have lagged markedly behind the great advances in imaging. MRI allows the surgeon to know pre-operatively the exact extent of the bone tumor with a remarkable degree of accuracy. In contrast, the surgeon performing a wide resection relies on very simple tools and techniques in the operating room (OR): identification of visible and palpable landmarks, basic handheld rulers, and intraoperative X-rays (which have poor sensitivity for detection of tumor extent). This profound lag in intraoperative technology makes it difficult or impossible for the surgeon to precisely reproduce the pre-operative plan at the time of surgery, despite having highly accurate pre-operative imaging.

In many cases, appropriate bone-conserving surgeries combined with structural bone allograft reconstruction can obviate the need for more aggressive reconstructions and thereby improve the longevity of the reconstructed limb. Structural bone allograft is a whole segment of bone obtained from a cadaver and is commonly used in orthopedics as an alternative to purely metal endoprosthetic reconstruction. If the allograft is successfully incorporated into the host bone, it has the distinct advantage of restoring bone stock, whereas metallic endoprostheses permanently replace bone. Moreover, endoprostheses typically loosen with time whereas an allograft that has united to host bone is unlikely to fail due to loosening. Despite these theoretical advantages, endoprostheses are often chosen because of the many complications associated with structural allograft. Nonunion and fracture are the two major mechanical complications in structural allograft surgery, with an 8% to 17% nonunion rate and a 5% to 20% fracture rate. Successful union of allograft to host bone has been shown in clinical and basic science studies to be related both to the ‘quantity’ and to the ‘quality’ of contact interface. Quantity of contact interface refers to the overall surface area of contact between allograft and host bone, as shown in green in Figure 2.2, with the goal being its maximization by eliminating gaps between the two bones. Quality of contact refers to the observation that the application of compressive mechanical forces across the allograft-host junction directly favors healing in a manner analogous to a heal-

ing fracture. These compressive stresses can be generated at the contact interface during external loading (i.e., when the patient bears weight) but also can be generated 'intrinsically' by tightly 'wedging' the allograft into the host bone (much like a nail being driven into a wall). This is analogous to compression plating of a fractured tibia: the compression plating construct generates 'inherent' compressive stresses across the fracture site while patient weight-bearing generates external compressive stresses.

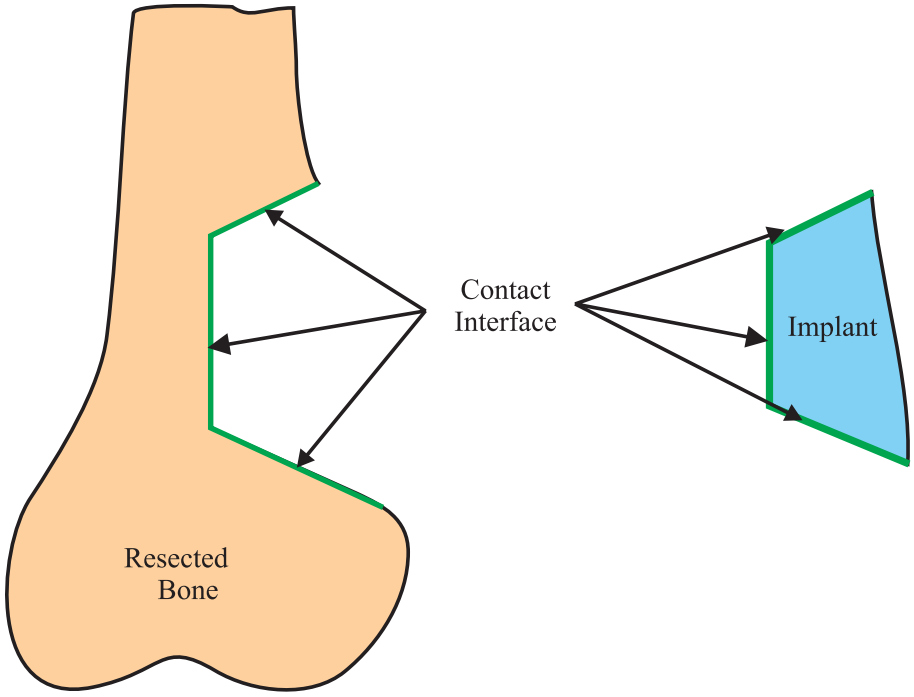

Figure 2.2: Contact interface between bone and implant showed in green

Revascularization and resorption of the allograft are important factors which contribute to allograft fracture. For example, drilling holes into or placing screws through an allograft can increase the fracture rate due to both mechanical discontinuity from the hole and the formation of an entry portal for blood vessels into the allograft, which can lead to rapid resorption of the graft. Improving the inherent mechanical stability of the allograft-host junction by creating a tight 'wedge fit' reconstruction may obviate the need for such screws and thus may also help decrease the risk of allograft fracture. The use of a custom fitted cutting guide may enable patients such as those depicted above in Figure 2.1 to have

a joint-sparing operation. The benefit of these guides is that they will be individualized to each patient's unique skeletal anatomy and tumor location. This will enable the surgeon to more precisely prepare and follow a pre-operative plan and improve the likelihood of performing a successful joint-sparing surgery without compromising the surgeon's ability to entirely remove the cancer. In a joint-sparing operation, an intercalary allograft is used to replace the resected bone. Currently, intercalary allografts are ordered pre-operatively and cut to size in the operating room by hand. The use of a second cutting guide to prepare the allograft will allow the surgeon to better match the allograft to the host bone, increasing allograft integration and minimizing the need for further surgeries due to issues such as allograft nonunion and skeletal fracture. The ability to precisely match allograft geometry to the host bone gives us a greater degree of freedom in the future to design curved jigs or cutting guides to minimize stress concentration.

2.2 Reverse engineering: from CT scan to 3D-printed cutting guide

From computer tomography (CT) scans, we can develop fully modifiable 3D CAD files by following a few simple steps. A flow chart for the entire process from imaging to pre-operative planning and surgery is illustrated in Figure 2.3. CT scans are slice representation of an organ. They have to be converted into a 3D representation, and after that into a modifiable CAD file. In this process, different software packages are used such as Invesalius (Software Público de Imagens Médicas, Brazil), Geomagic (3D Systems, USA) and SolidWorks (Dassault Systèmes, France).

I A computer tomography is a very common procedure to obtain medical images from a patient. It is used to obtain detail scans of sections inside the patient's body. The ouput is a series of files (also called DICOM files), each one describing a slice (cross-section) representation of the site being imaged. All these slices are two-dimensional (2D) images.

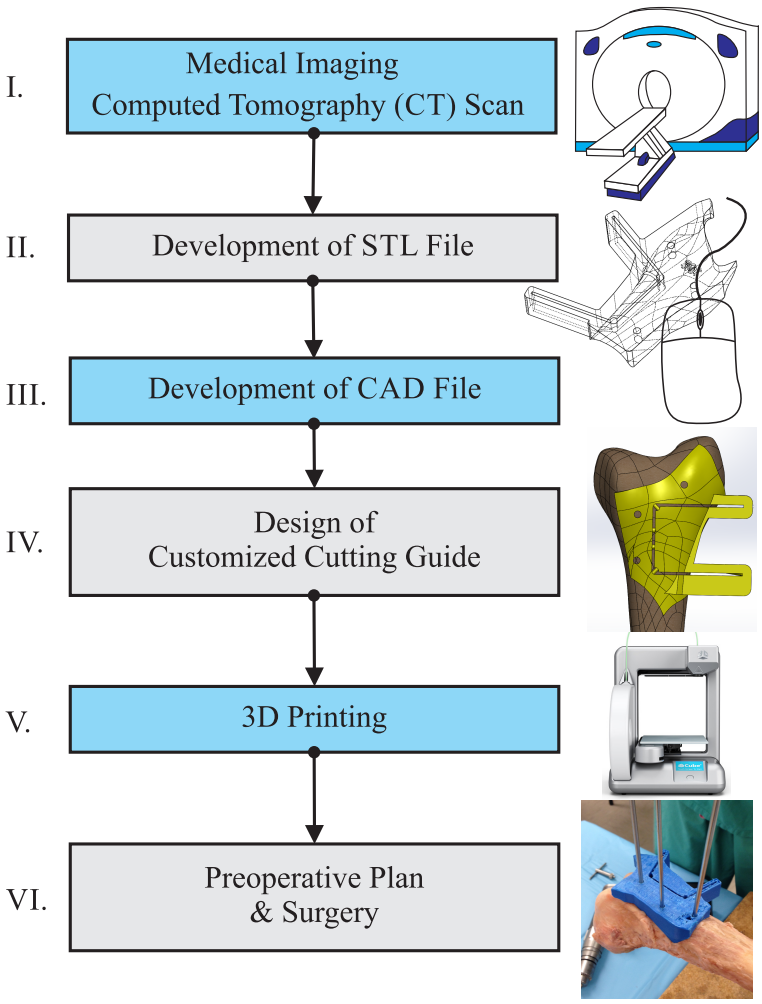

Figure 2.3: Workflow for cutting guide fabrication from CT scan

II Invesalius is a public, open source, software from the Brazilian government. It is a medical imaging reconstruction software that takes the DICOM files from the CT scan and creates a three-dimensional (3D) surface representation of a particular part of the patient. That 3D image can be easily exported in a stereolitography (STL) format, which is a standard among CAD softwares and 3D-printing.

III To reduce the noise from the DICOM files, Geomagic can be used as a STL image processing software. The software delivers STL data into CAD-base file that can be later edited in any engineering CAD software. Geomagic treats the STL image as a cloud of polygons, making it easier to edit, smooth, correct and clean in order to convert it to a CAD file. Figure 2.4 illustrates a 3D representation of a femur bone before and after editing in Geomagic.

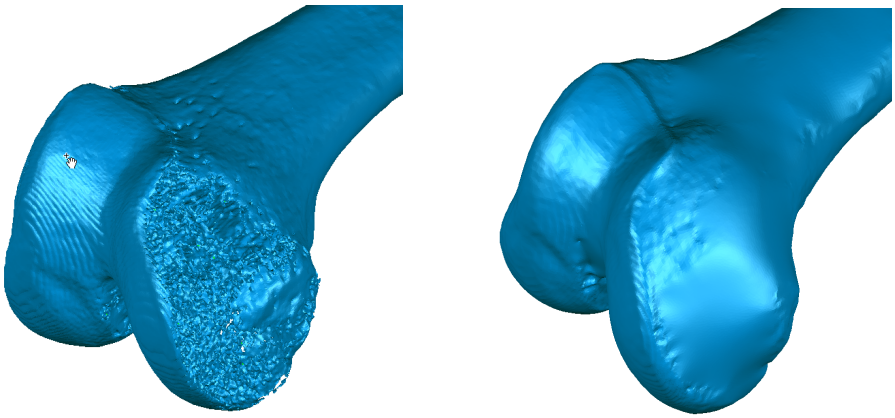

Figure 2.4: 3D representation of femur edited in Geomagic
(*a*) Before editing, and (*b*) After editing.

IV Once the noise of the STL file is completely reduced (or even eliminated), Geomagic can compute an algorithm to export it as a CAD file.

V This file is uploaded to Solidworks, a typical solid modeling CAD engineering software in which the cutting guide is designed based on the bone's surface features, as shown in Figure 2.5.

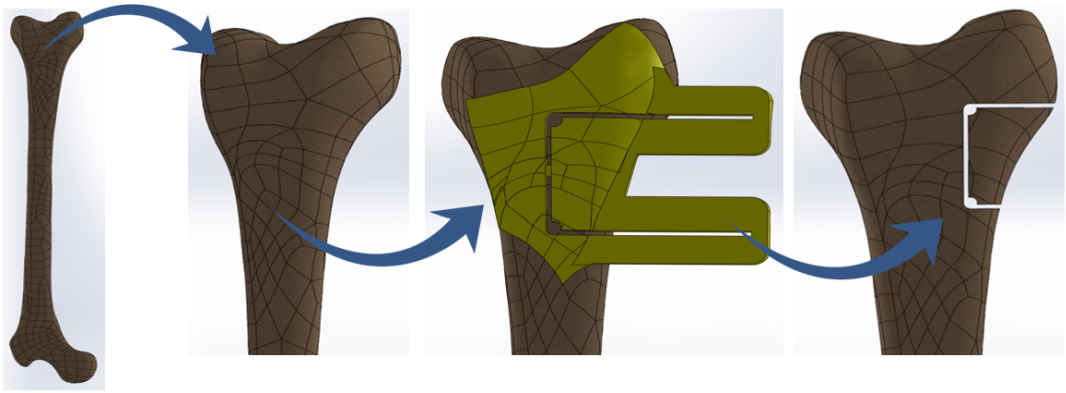

Figure 2.5: Cutting guide design using Solidworks software

VI Once the design is complete, Solidworks will be able to export it as STL file which can be used by any 3D printer.

VII Finally, Once the guide is printed, it can be used in the patient during surgery in the OR.

2.3 Parameters of the cutting guide and cutting path

The design of the cutting guide must consider several factors to accomplish a successful resection. Since the form of the guide is based on the patient's anatomy, the topology of the surface of the bone is the first parameter to study. This complex surface could be replicated according the steps depicted in Section 2.2. However, the morphology of bone's surface alone is not enough as soft tissue surrounding it must be also considered. Depending on the extension of the tumor, soft tissue could also be compromised and, therefore, surgeons would not be able to strip to bone until the cortical surface. Cutting guide must consider the added thickness of the muscle enclosing the bone and also must allow for a correct and stable fitting. Form closure principles could be applied to restrict relative displacement between bone and cutting guide.

Once the morphology of bone's surface has been replicated on the guide's design, the next step is to find a bone landmark that will aid surgeon to position the guide. In our

experiments, we focused on femur bones. Every femur features in its epiphysis a curve formed by the superior ridge or the articular cartilage. This curve differs from subject to subject making it a very particular landmark. As depicted in Figure 2.6, replicating the trajectory of this curvature in the top edge of the guide will serve as a location feature to position the guide. Osteosarcoma is likely to appear either in distal femur or proximal tibia and always around the knee articulation (sites of bone growth) due to high cellular activity around that area. Therefore, cutting guide will always have this aid for positioning as tibia also have similar landmarks.

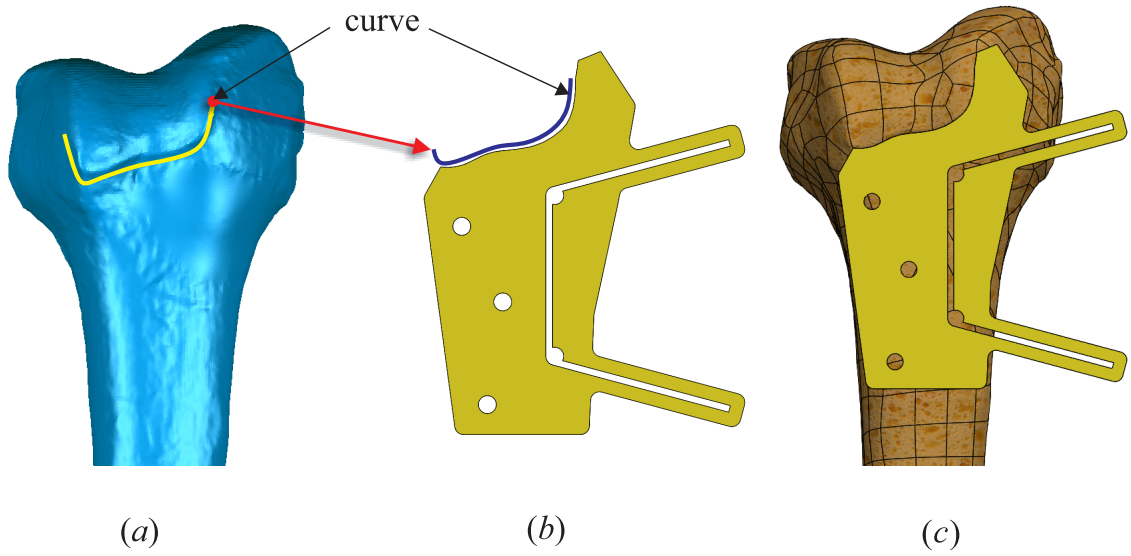

Figure 2.6: Superior ridge or articular cartilage sketched on cutting guide: (*a*) Femur with depicted cartilage line, (*b*) Cartilage line replicated on cutting guide, and (*c*) Cutting guide in position over bone using cartilage line as reference

Finally, the cutting path trajectory must also be included in the guide. Sketching the cutting path depends largely on the location of the tumor and it must allow for negative margins resections (meaning that after surgery, no tumor remains on bone). The tolerance between the cutting path edges and the tumor boundaries must be studied and discussed. Although location of tumor is very important, the geometry of the cutting path needs to be revised as well. A geometry that allows for sharp corners, for example, will introduce stress

concentrators in the bone after resection which, eventually, will become fracture initiator. Cutting path must eliminate sharp corners and also must favor integration between bone and implant. For instance, a cutting path that produces a defect that could increase stress shielding (see Section 1.5) is not acceptable.

2.3.1 Straight cutting path vs. tapered cutting path

A tapered cutting path is proposed as an alternative to a straight path, as illustrated in Figure 2.7, in order to increase the contact area between the resected bone and the implant, effectively maximizing the implant fit. Increased normal stresses encourage bone healing [19] and bone ingrowth, and greater contact area diminishes stress shielding at the bone-implant interface [20]. Also, during surgery, an implant is easier to fit in a tapered cut defect due to the 'wedge' shape. Our objective is to create an implant that will theoretically best resist implant loosening. The 2D approximation and uniaxial compression tests were simulated for different increments in taper angle α (0, 5, 8, 10, 12 and 15°).

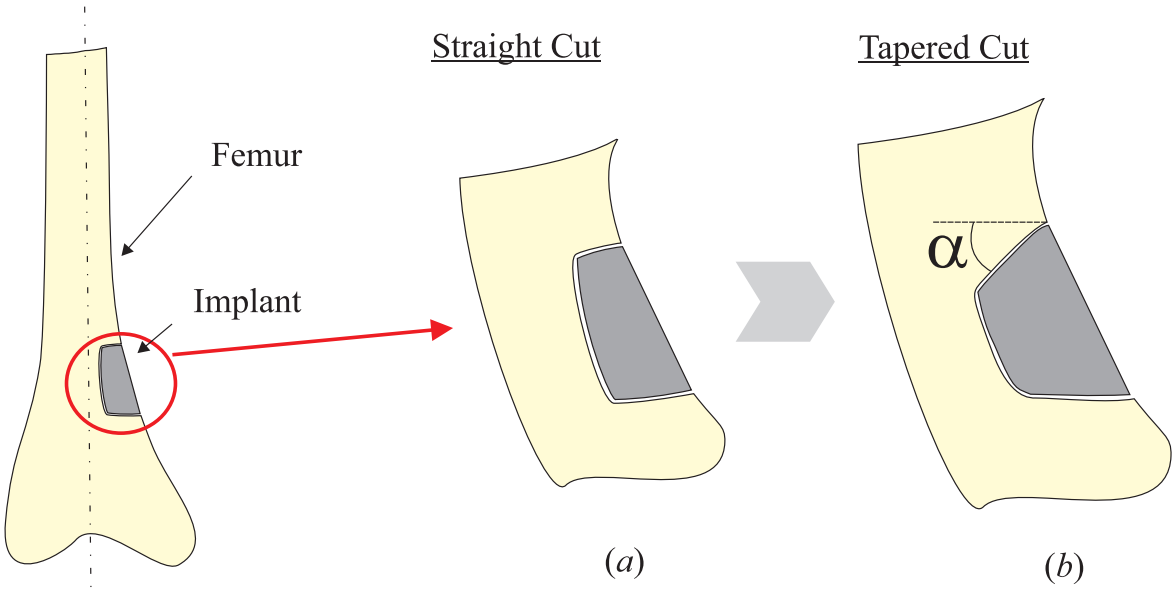

Figure 2.7: Comparison between tapered and straight cutting paths (*a*) straight cut vs. (*b*) tapered cut of a resection

2.3.2 Calculating the compression force using FEA

A straightforward analysis to calculate the forces acting on leg is proposed [21]. Since we are focusing on Femur's anatomy in this study, forces acting on leg need to be analyzed. In Figure 2.8, a schematic of the features of the anatomy of leg and the corresponding forces acting on it for a person standing on one foot is considered. During normal walking, there is always a moment where only one foot is in the air while the other one is withstanding the body weight. According to Williams and Lissner [22], the center of gravity of the person could be located at the midline of the body and as the person walks, the reaction force exerted from the floor to the foot must be directly over that midline so no torque is produced (to prevent the person from falling). This is an unnoticed process in which every person is involved during everyday walking. The notations in Figure 2.8 are explained in the following:

F : Net force acting on the greater trochanter exerted by abductor muscles

R : The force of the pelvis socket (acetabulum) on the femoral head

W_L : The weight of the leg; this value is related to the total weight of the body W as $W_L \approx \frac{W}{7}$ [22]

N : The reaction force of the floor opposed (and equal) to W

The force produced by abductor muscles F is acting with an angle of 70° with respect to the X-axis [21]. Also, average distance values shown in Figure 2.8 corresponds to the adult biotype. From the free body diagram, we can formulate the following equations of

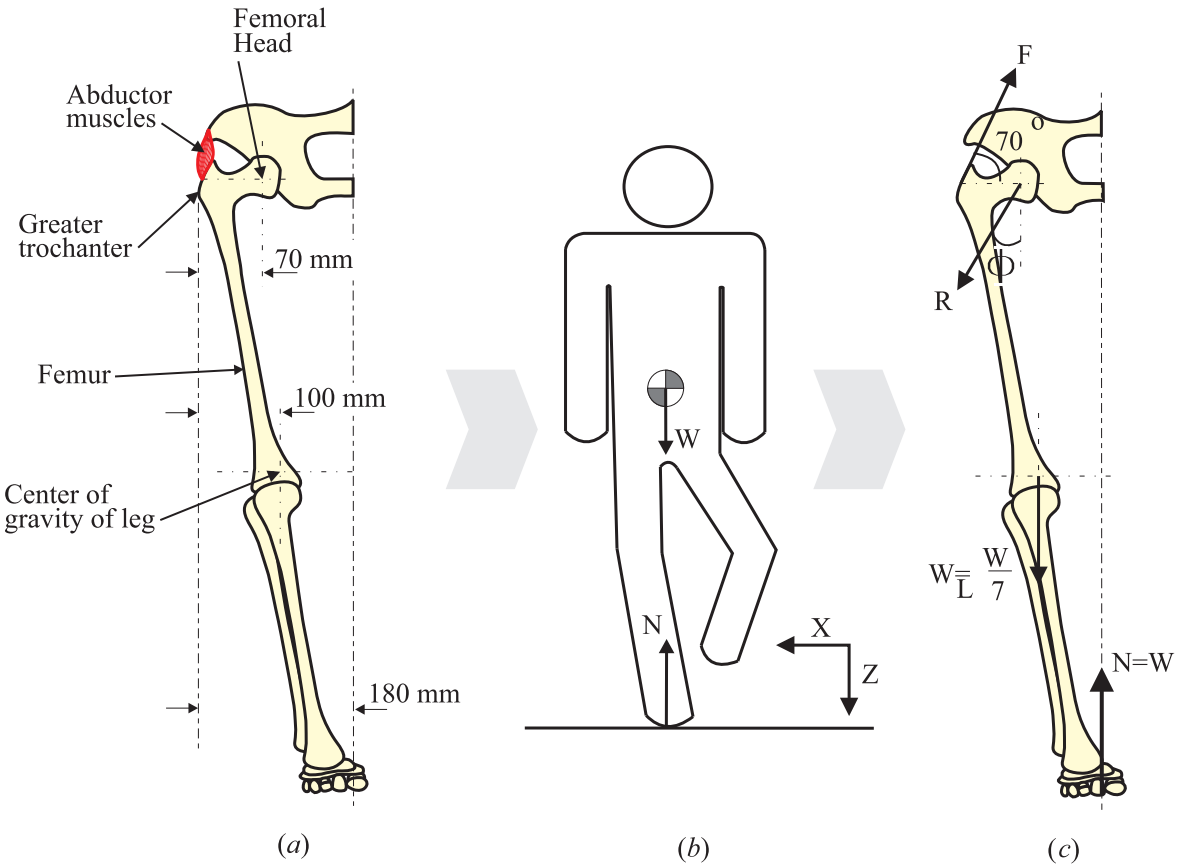

Figure 2.8: Analysis of forces acting on human leg: (*a*) Features of the anatomy of the leg, (*b*) schematic of a one-foot standing person, and (*c*) free body diagram of forces acting on the leg

equilibrium:

$$\begin{aligned}
\sum F_x &= F\cos(70^\circ) - R_x = 0 && (2.1)\\
\sum F_z &= F\sin(70^\circ) - R_y - \frac{W}{7} + W = 0 && (2.2)\\
\sum \tau &= -F\sin(70^\circ)(7) - \left(\frac{W}{7}\right)(10-7) + W(18-7) = 0 && (2.3)\\
&= -6.6F - \frac{3}{7}W + 11W = 0
\end{aligned}$$

From Equation (2.3), it is easy to obtain $F = 1.6W$, which can be substituted into Equations (2.2) and (2.1) to yield

$$\begin{aligned}
R_z &= F\sin(70^\circ) + \frac{6}{7}W = (1.6W)(0.939) + 0.857W = \underline{2.36W}\\
R_x &= F\cos(70^\circ) = (1.6W)(0.342) = \underline{0.55W}
\end{aligned}$$

We will consider only the femur[1] to calculate the internal compression force that will be used in the finite element analysis. As shown in Figure 2.9, the compression force F_c can be readily obtained with an equilibrium equation about the Z-axis, as follows

$$F_c + (1.6W)(\sin(70^\circ)) = 2.36W \qquad (2.4)$$

Equation (2.4) can be solved to find $F_c \approx \frac{6}{7}W$. For an average male with height 1.75 m and weight of 73 kg, the compression force will be $F_c \approx 600N$. An uniaxial compression test is modeled with FEA to obtain stress behavior around cutting path for half femur in Section 2.3.3.

[1] Ultimately, we will consider only a portion of that femur to simplify our analysis.

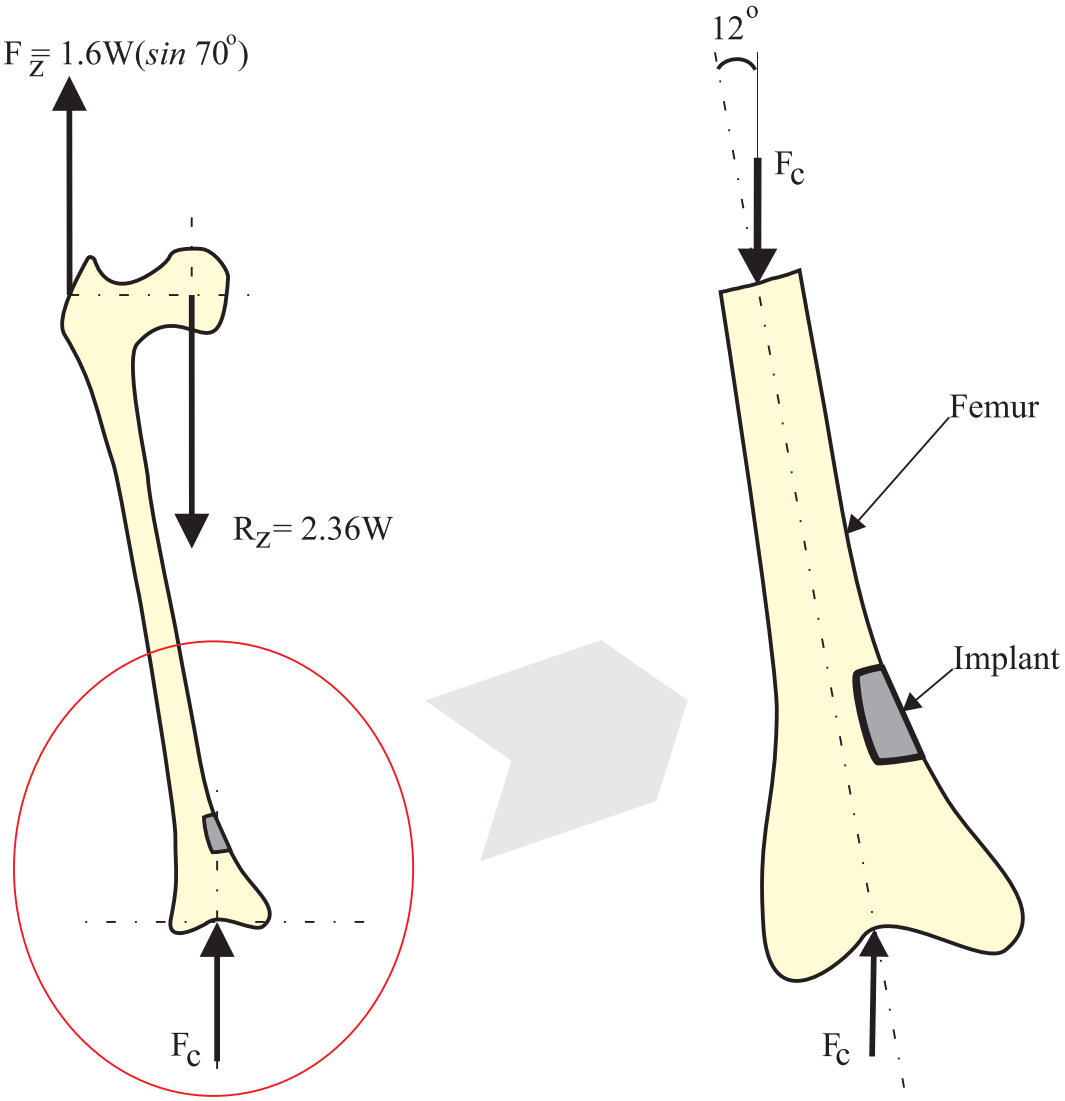

Figure 2.9: Free body diagram of femur to calculate internal compression force F_c

2.3.3 FEA for tapered cutting path

FEA software is used to simulate a compression force exerted over the femur bone. The magnitude of the compression force F_c was obtained according to the procedure in Section 2.3.2. Only the 2D case is considered for this study as it is a good approximation. The simulation is performed over a femur bone that has been cut, meaning that the extracted portion that encloses the tumor cell is missing. Our points of interest for this simulation are presented in Figure 2.10, *i.e.* points a, b and c. These points typically behave as stress concentrators since they are corners of the cutting path with discontinuity between line segments. Compression stress will be recorded along the edges $\overline{ab}$ and $\overline{ac}$.

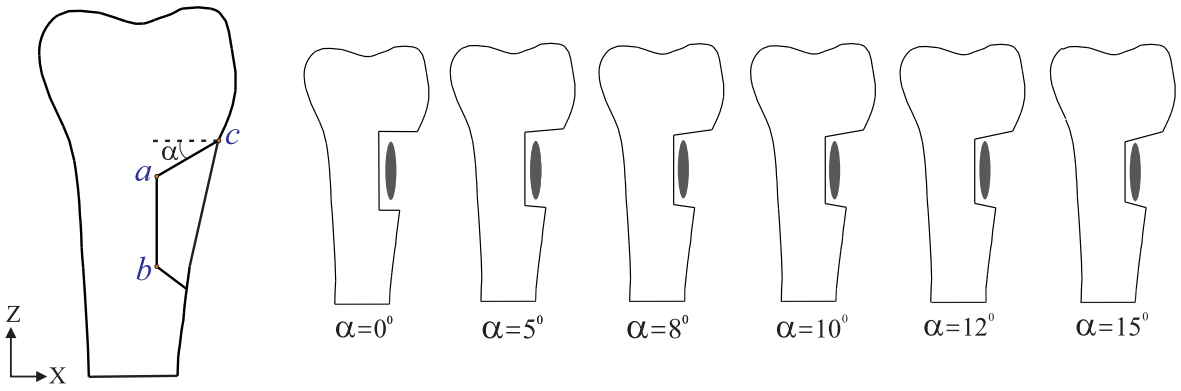

Figure 2.10: Interest points for FEA and tapered cut angle variation from $\alpha = 0^\circ$ to $\alpha = 15^\circ$

Table 2.1 shows the parameters used during FEA [23]. Normal stress was recorded along the edges $\overline{ab}$ and $\overline{ac}$ for compression tests with typical forces during walking. Figure 2.11 shows the disposition of the elements in the FEA mesh. FEA showed increments of normal stress at the points of interest. The results of FEA are presented in Figures 2.12 and 2.13 for each increment in the taper angle. Point c reports zero stress. As it gets closer to point a, the magnitude of compression stress increases, as shown in Figure 2.13. The magnitude of compression stress are reported along both edges $\overline{ab}$ and $\overline{ac}$ with maximum values at the corners (points a and b), as expected because of the stress concentration. As illustrated in Figure 2.12 minimum values for the edge $\overline{ab}$ are located around the midpoint

Parameters	Values
Compression force (F_c)	600 N
Poisson ratio (ν)	0.42
Young's Modulus (E)	17.5 GPa
Bone density (ρ)	2000 kg/m^3
Number of nodes	$25,000$
Element size	0.25 mm
Type of element	Triangular
Type of test	Compression, plane stress analysis
Boundary conditions	One end fixed (No rotations, no translations) and one end loose (translation only in the direction of the longitudinal axis of the bone)

Table 2.1: Parameters in FEA

of the edge with a small shift, towards the proximal part of femur, as the tapered angle increases.

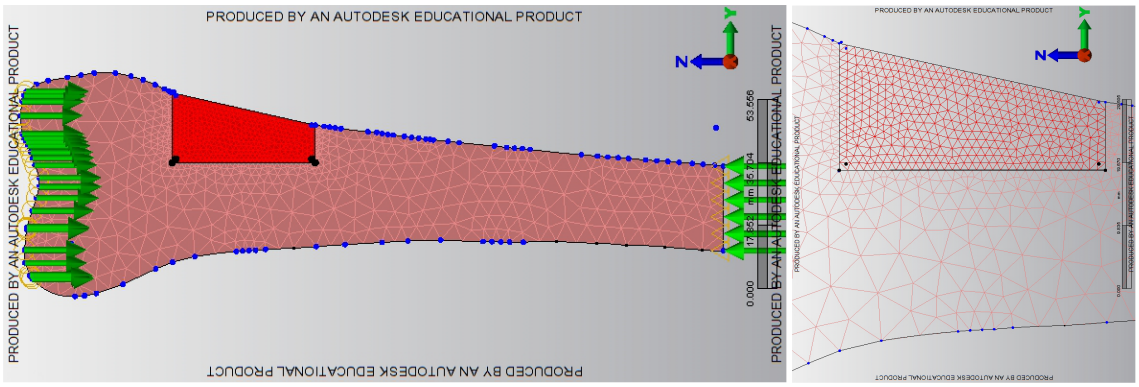

(*a*) (*b*)

Figure 2.11: Disposition of elements for FEA (*a*) uniaxial compression test and 2D approximation and (*b*) zoom-in view indicating element distribution and stress concentration around the points of interest

This analysis confirms that the contribution of the normal stress increases as edge $\overline{ac}$ tilts accordingly with the angle α. From the stress and mechanics point of view, a tapered cut favor the bone healing as normal stress is larger.

2.4 Testing accuracy of cutting guide in comparison with current resection technique

The next step is to test the accuracy of cutting guides and compare it with the current and 'manual' resection technique. We hypothesized that customized cutting guides will increase the accuracy of skeletal tumor resection in comparison with the freehand techniques; therefore, the use of customized cutting guides will also improve posterior implant fitting. Results of an experimental case study are presented in Section 2.4.1 to prove this hypothesis.

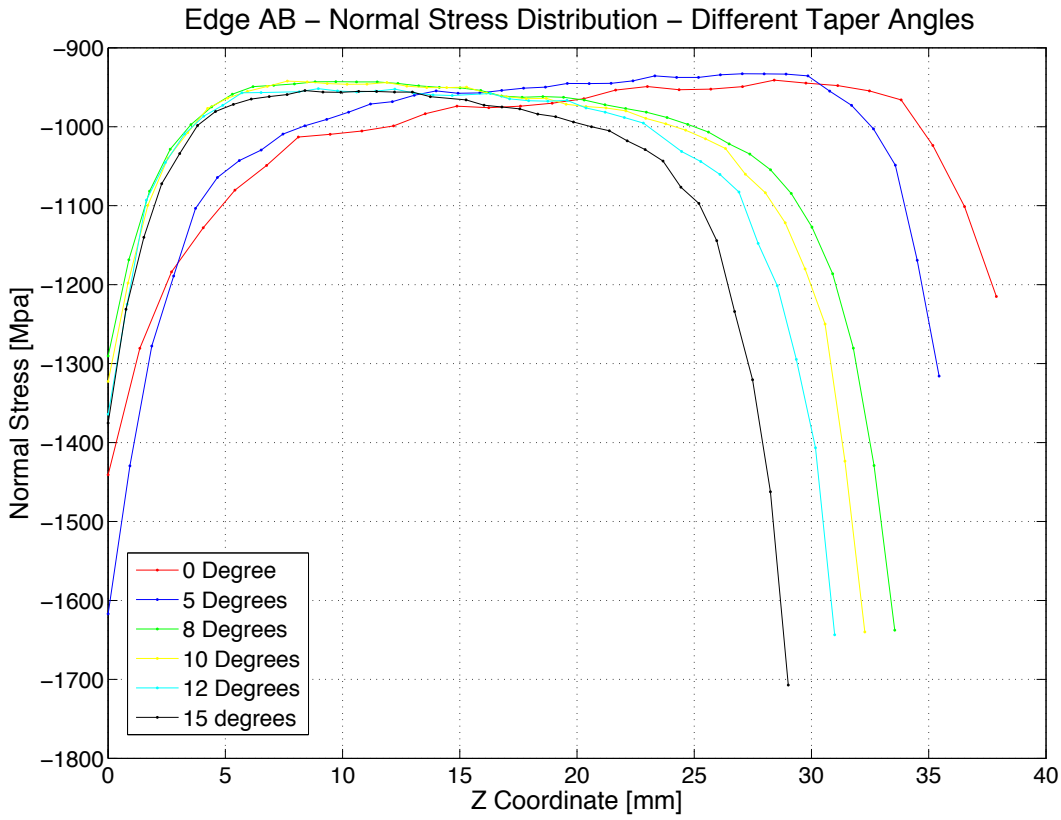

Figure 2.12: FEA results of the edge $\overline{ab}$ under different taper angles of $\alpha =$ 0°, 5°, 8°, 10°, 12°, and 15°

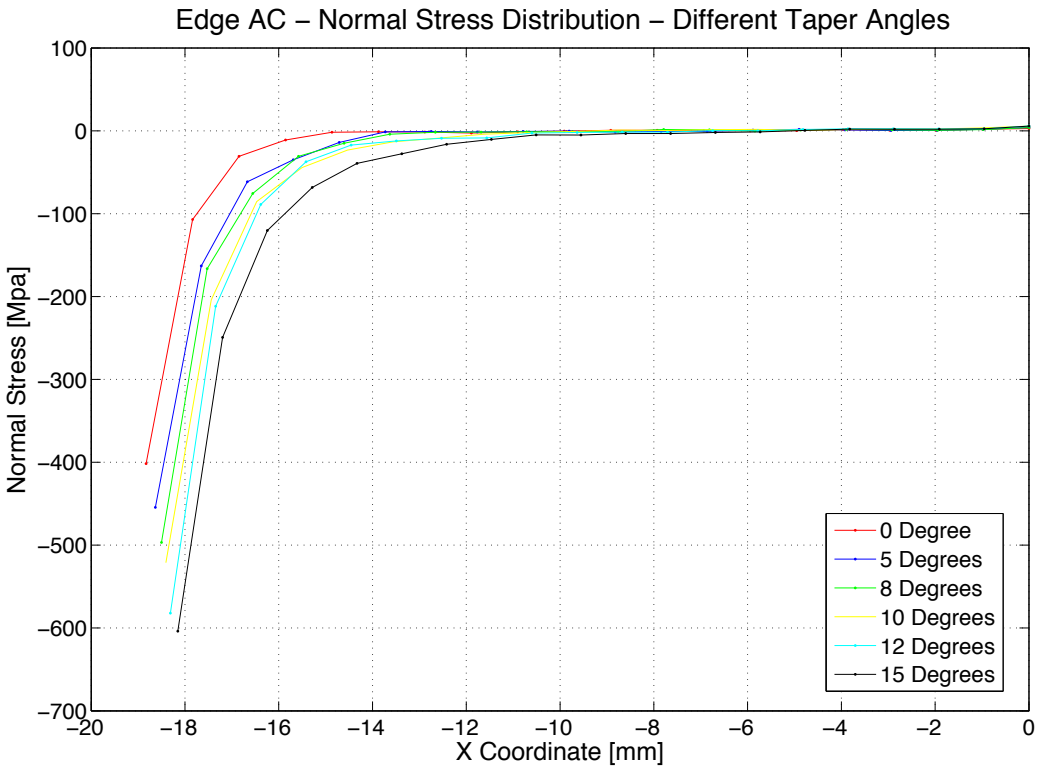

Figure 2.13: FEA: results of the edge $\overline{ac}$ under different taper angles of $\alpha = 0°, 5°, 8°, 10°, 12°$, and $15°$

2.4.1 Experimental study

Nine pairs of skeletonized cadaveric femurs were utilized for this study. The flowchart used to design and manufacture the cutting guides and implants is shown in Figure 2.3, and explained in Section 2.2. The images of femora were first obtained using a clinical CT scanner (GE VCT) running a standard bone algorithm with a 0.625 *mm* slice thickness, 0.5° pitch, and small field of view (FOV). The images were then exported from the PACS server as DICOMS and imported into InVesalius to transform the files into stereolithography (STL) files. The STL files were then imported into Geomagic and transformed into 3D CAD models. Finally, the resulting 3D files were imported into SolidWorks. At this point, virtual bone tumors ($10 \times 10 \times 25$ *mm* ellipsoids) were positioned on the distal medial metaphases. Surgical resection plans were then outlined virtually on the computer by the surgeon. While the resection plans were unique to each femur, they all had approximately the same shape and dimension. The shape was trapezoidal (tapered) according to Section 2.3.1 with an angle $\alpha = 15°$. Resections were planned with full thickness through the femora on the anterior-posterior axis.

Cutting guides were then designed for one femur from each pair (alternating left and right) using SolidWorks. The undersurface of each guide was designed to match the anterior surface of the femur and the top was a flat surface with a slot to guide a saw blade in accordance with the pre-operative plan. In order to facilitate proper placement of the guides, the distal edges were designed to align with the superior ridge of the medial femoral articular surface and three holes were placed to attach the guides to the bone using medical pins. Implants corresponding to each of the resection plans were also designed. The guides and implants were then printed in acrylonitrile butadiene styrene (ABS) using a Cube 2nd Generation 3D printer (3D Systems, Rock Hill, SC).

In the following Sections 2.4.1.1 and 2.4.1.2 we discuss the experimental setup and corresponding procedure to process the data obtained; and later, in Section 2.4.1.3 we present the results obtained.

2.4.1.1 Experimental setup and procedure

A senior orthopedic surgical resident performed the resections in two separate sessions and alternated between cutting guides and freehand in order to minimize the role of experience. The femora were stabilized in the operative field by a tabletop vise, as illustrated in Figure 2.14(*b*). The cutting guide was aligned with the superior ridge of the articular surface, seated, and held in place by three bicortical 5 *mm* Steinmann pins as shown in Figure 2.14(*d*). An oscillating sagittal saw (Stryker, Kalamazoo, MI) equipped with a 0.89 *mm* sagittal saw blade, shown in Figure 2.14(*a*), was used to perform the resection through the slots in the jig. Once the resection was completed, the pins and guide were removed.

For the freehand resection group, the surgeon was given a printout of the preoperative plan showing the distances of each osteotomy (see Section 1.5) line from major palpable and identifiable landmarks (*e.g.*, cartiladge line, bone surface, etc). The surgeon then used a ruler and a marking pen to draw the pre-operative plan on the femur. The region was then resected manually with the sagittal saw.

Upon completion of each resection, the surgeon attempted to press-fit the implant into the resulting defect. In those cases when the defect was too small, the surgeon was allowed to make additional improvements until a satisfactory implant fit was achieved.

2.4.1.2 Data processing

The femurs were re-scanned after surgery using the same CT scanner and settings. The images were then imported into SolidWorks, as previously described in Section 2.2, to quantify the accuracy of the implant fit. This was done by comparing the directions of vectors normal to cut planes of the resected bone with their corresponding vectors on the sides of the implant. First, each of the three planar surfaces of the implant was defined by a normal vector $\overrightarrow{n_x}$, where x represented the number of the surface as shown in Figure 2.15. The surface of the implant corresponding to the proximal cut plane was labeled

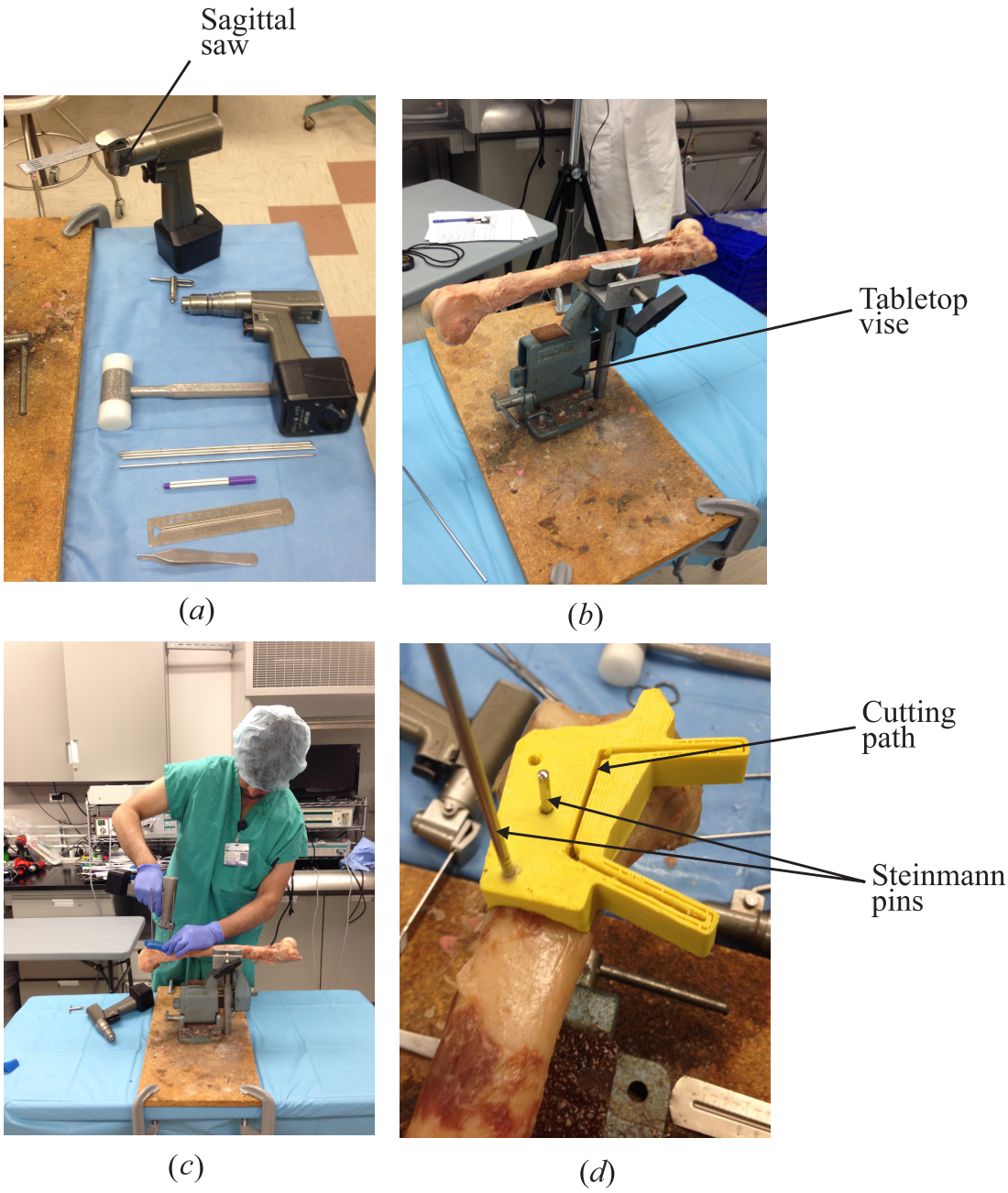

Figure 2.14: Photos of cadaveric resection (*a*) the instruments used in the surgery; (*b*) a femur mounted in a vise for stability; (*c*) the surgeon fixing the cutting guide to the femur with a pin; (*d*) a close up of the cutting guide positioned on the femur prior to resection

with subscript **1**, the sagittal plane **2**, and the distal plane **3**. Each value for $\overrightarrow{n_x}$ was obtained by determining the cross product of the vectors defined by points $P_1 - P_2$ and $P_1 - P_3$ that defined each plane. Based on the preoperative plans, the ideal angle for these vectors was 15° for $\overrightarrow{n_1}$ and $\overrightarrow{n_3}$, and 0° for $\overrightarrow{n_2}$, with respect to the Z-axis.

$$\overrightarrow{n_x} = \overrightarrow{P_1P_2} \times \overrightarrow{P_1P_3} \tag{2.5}$$

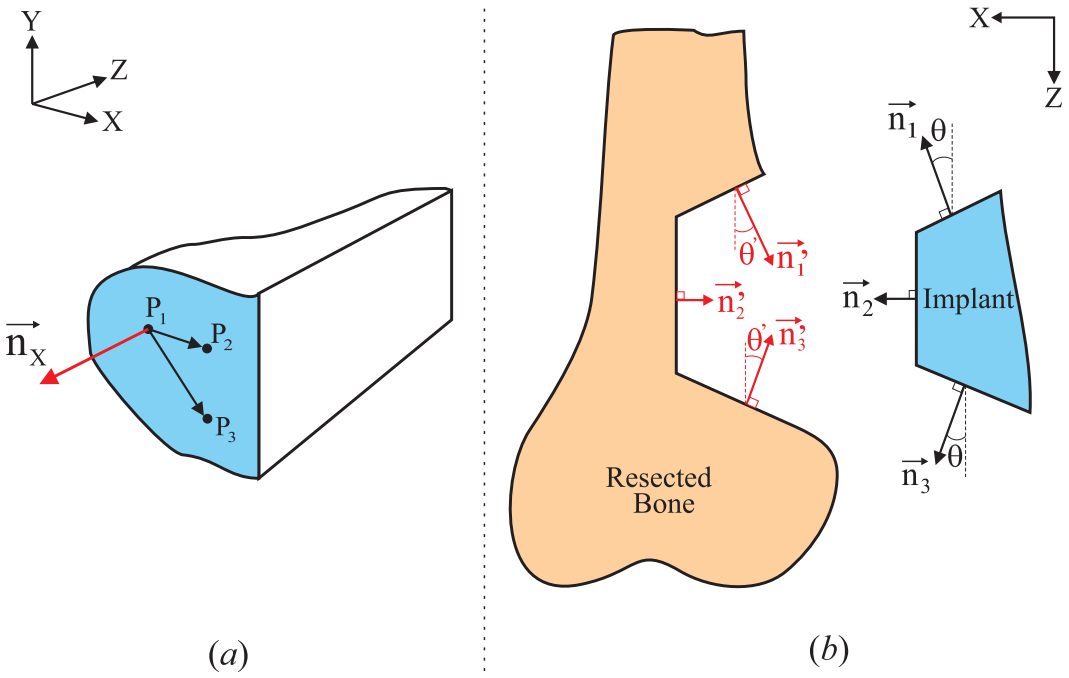

Figure 2.15: Ilustration of normal vectors to estimate deviation from pre-operative plan (*a*) a 3D-view of normal vectors $\overrightarrow{n_x}$ of the implant, and (*b*) normal vectors for both resected bone and implant

Second, the respective vectors for the resected femora were calculated. Due to a variety of factors (e.g., saw vibration, tissue anisotropy, surgical technique) these surfaces were not completely planar. The analysis was restricted to the exposed cortical surfaces because of the natural deviation from planarity of cancellous bone as well as the compressibility of cancellous bone during implant impaction. Therefore, for each surface, **1**, **2**, and **3**, planes were defined from hundreds of points positioned along the cortex, according to the schematic of Figure 2.16, and used to define the normal vectors ($\overrightarrow{n_x}$).

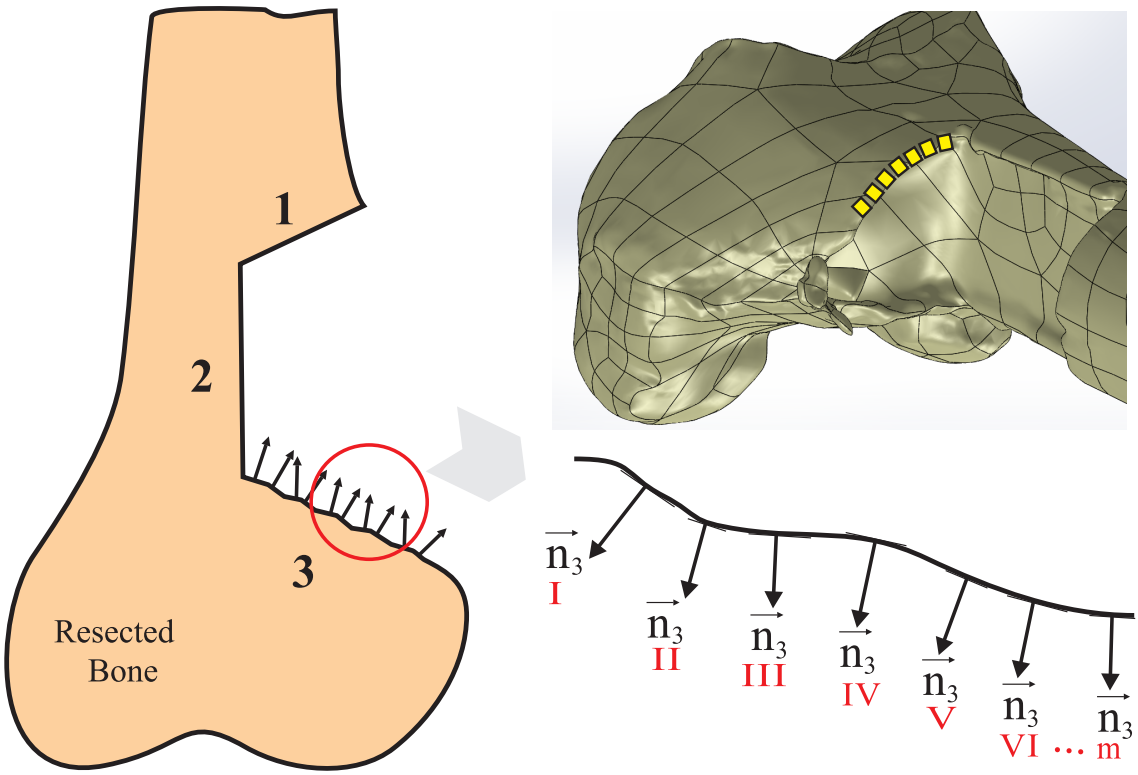

Figure 2.16: Due to imperfect topology of cortical surface of bone after resection, several planes are defined to obtain *m* number of normal vectors in surface **3** of resected bone

Finally, these normal vectors $\overrightarrow{n_x}$, like the ones presented in Figure 2.16, were compared to the vectors for the implants and the differences, in terms of angle θ, were calculated. The definition of θ, for each plane, is shown in Figure 2.15, and defined by the following equation

$$\overrightarrow{n_x} = \begin{pmatrix} a \\ b \\ c \end{pmatrix} \qquad \theta = \arctan\left(\frac{a}{c}\right) \tag{2.6}$$

All of the values of θ', in the resected femora, shown in Figure 2.15, for each plane were then averaged to obtain the mean and standard deviation. The values calculated for θ included both positive and negative numbers, limiting the importance of a comparison of means. Therefore, the absolute values of the differences between θ and θ' were calculated for each resection plane. These values were then averaged by resection plane within each of the two groups and compared with paired t-tests using SPSS (Ver.19, SAS Institute, Cary, NC) at an alpha of 0.95.

2.4.1.3 Results

After the implants had been press-fit into the resected femurs, a qualitative assessment of implant fit was made by visually examining digital photographs taken for the anterior and posterior surfaces, as shown in Figure 2.17. Implant fit in the cutting guide group appeared better than the freehand group for the majority of pairs. Moreover, while several specimens from the freehand group had large gaps (> 5 *mm*) between the implant and the bone, no large gaps were seen in the cutting guide group. It was observed that for both groups, implant fit appeared better when viewed from the anterior side compared to the posterior side.

For the quantitative analyses, absolute values of the differences between θ and θ', according to Figure 2.15 were calculated of each resection plane **1**, **2**, and **3**. The results from the quantitative analysis confirmed the visual analysis with the mean angles closer to

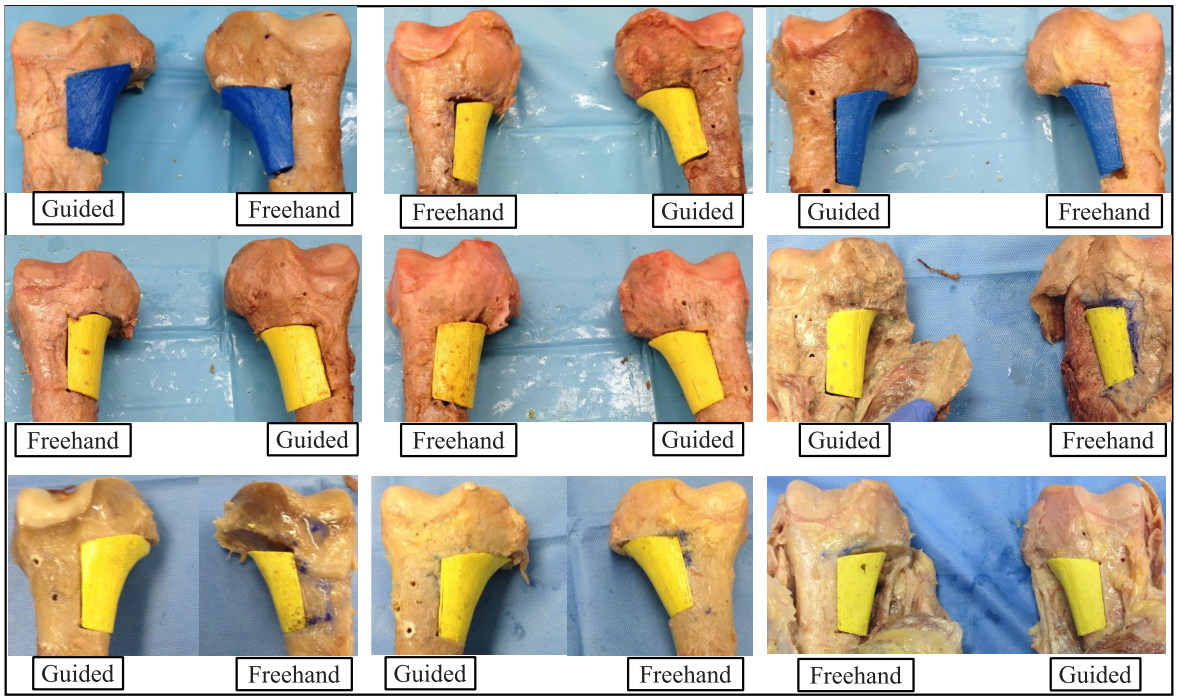

Figure 2.17: Qualitative assessment of implant fitting

the planned angles for all three planes in the cutting guide groups compared to the freehand group. All results are presented in Table 2.2. Comparison of the differences showed that for plane 2 and 3, specimens from the cutting guide group deviated from the preoperative plan significantly less than those in the freehand group.

		Cutting Guide		Freehand		p-value
	Planned Angle	Mean Angle (SD)	Difference (SD)	Mean Angle (SD)	Difference (SD)	
Plane 1	15.00	15.36 (6.56)	5.30 (3.42)	12.23 (8.13)	7.16 (4.14)	0.358
Plane 2	0.00	1.78 (1.6)	1.78 (1.6)	4.41 (3.46)	4.41 (3.46)	0.038
Plane 3	15.00	15.69 (2.79)	2.20 (1.69)	19.23 (8.31)	7.96 (4.23)	0.003

Table 2.2: Comparative results of implant fit in which absolute values of the differences between θ and θ' are presented as well as mean angles for each plane **1**, **2**, and **3**

2.4.2 Discussion

The specimens that showed large gaps between the implants and the host bone, all were in the freehand group. Similarly the specimens that had the best implant fit, all were from the cutting guide group.

Three planes of resection, **1**, **2**, and **3**, were measured in comparison to the preoperative plan. The average absolute angle deviation from the planned area of resection in the free-hand cutting group was 7.16° for plane **1**, 4.41° for plane **2**, and 7.96° for plane **3**. For the group of femora resected using a cutting guide the average angle deviation was 5.30° for plane **1**, 1.78° for plane **2**, and 2.20° for plane **3**. Paired t-tests yielded p-values of 0.358 for plane **1**, 0.038 for plane **2**, and 0.003 for plane **3**, indicating that the cutting guides matched the resection planes closer to the preoperative plan for **2** and **3**. The quantitative analysis supported the qualitative data with significantly less deviation from the preoperative plan seen for two of the three resection planes in the cutting guide group, indicating superior implant fit.

2.5 Summary

This series of experiments was performed to test the hypothesis that cutting guides can improve the accuracy of fit for customized endoprostheses when compared to traditional freehand resection. The results were first assessed visually and it was apparent that the use of cutting guides resulted in smaller gaps between the implants and the host bone.

While this study offers strong support that customized cutting guides can improve the fit of endoprosthesis in skeletal tumor surgery, it does have several limitations. First, the positioning of the cutting guides with the femora still relied on the use of anatomic landmarks and this could contribute to error in alignment. Second, the resections were performed by a postgraduate 4th year orthopedic surgery resident instead of an attending orthopedic oncologist. Therefore, it is possible that a better trained surgeon would have been able to reproduce the preoperative plans using a freehanded technique. Third, the study was performed using skeletonized femora, which provided an expansive field of view. However, this exposure is likely to have benefited both groups and may not have affected the comparisons being made in this study. Finally, the surgeon was allowed to refine the cuts in both groups to optimize implant fit. As in the large exposure, this is likely to have improved the results for both groups equally.

The clinical utility of this study can only be generalized to patients with tumors that closely resemble our experimental model. For example, patients with lower grade malignant lesions which are caught early are confined to the bony compartment.

Chapter 3

Kinematic Modeling and Error Analysis for the Positioning of Cutting-Guide

3.1 Introduction

Computer-generated cutting guides have been demonstrated in cadaver models to be more effective in reproducing preoperative plans for sarcoma resections when compared to free-hand techniques, as presented in Chapter 2. However, the accuracy of resection using these guides remains in need of refinement prior to clinical. It is also obvious that any error introduced in the resection process could cause catastrophic consequences in the outcome of the surgery.

After several experiments where cutting guides were evaluated, we hypothesize is that the major contribution of the error found in Section 2.4.1 comes from the surgeon's positioning of the guide on the bone. Although we design the cutting guide with a built-in feature that allows the surgeon to position it while matching the anatomical feature of the superior ridge of the cartilage in the distal part of the bone, results have demonstrated that this feature alone may not be enough.

Theoretical analysis and experimental validation are needed to verify this hypothesis. Based on the mathematical modeling, we may need to revise the design of cutting guides to minimize the positioning errors and to enhance the consistency and robustness of the process.

Soft tissue on the bone surface also plays a significant role during the positioning of cutting guides due to its random distribution and variability. Quantifying the effect of soft tissues is important in our research study to optimize these guides in order to improve resection accuracy, by employing design features.

To sum up, two major issues require further research study in the resection process using cutting guides:

- The cutting guide must overcome the positioning error introduced while the surgeon place the guide on the bone's surface, and
- The design of the cutting guide must accommodate the randomly distributed soft tissue and its variability.

3.2 Setup of the coordinate frames

The coordinate frames used in the following kinematic analysis is illustrated in Figure 3.1. First, we defined a coordinate frame $\{\mathbf{B}\}$ for the bone with coordinates XYZ. The tumor cell, or osteosarcoma, is represented by the point T located in the origin of $\{\mathbf{B}\}$. Additionally, another frame for the cutting guide is defined as $\{\mathbf{G}\}$ with coordinates xyz. In frame $\{\mathbf{G}\}$, the location of the tumor is defined by point T', which is the origin of $\{\mathbf{G}\}$.

Cutting path for resection is presented in frame $\{\mathbf{B}\}$ as $\overline{ABCD}$ and is also depicted in frame $\{\mathbf{G}\}$ as $\overline{A'B'C'D'}$. The anatomical curve of the superior ridge of the cartilage of the bone is represented as c_B in $\{\mathbf{B}\}$ frame and as c_G in $\{\mathbf{G}\}$ frame.

An ideal case is presented in Figure 3.1(b), where both frames $\{\mathbf{B}\}$ and $\{\mathbf{G}\}$ coincide with each other. Ideally, after aligning c_B and c_G, points T and T' should also coincide.

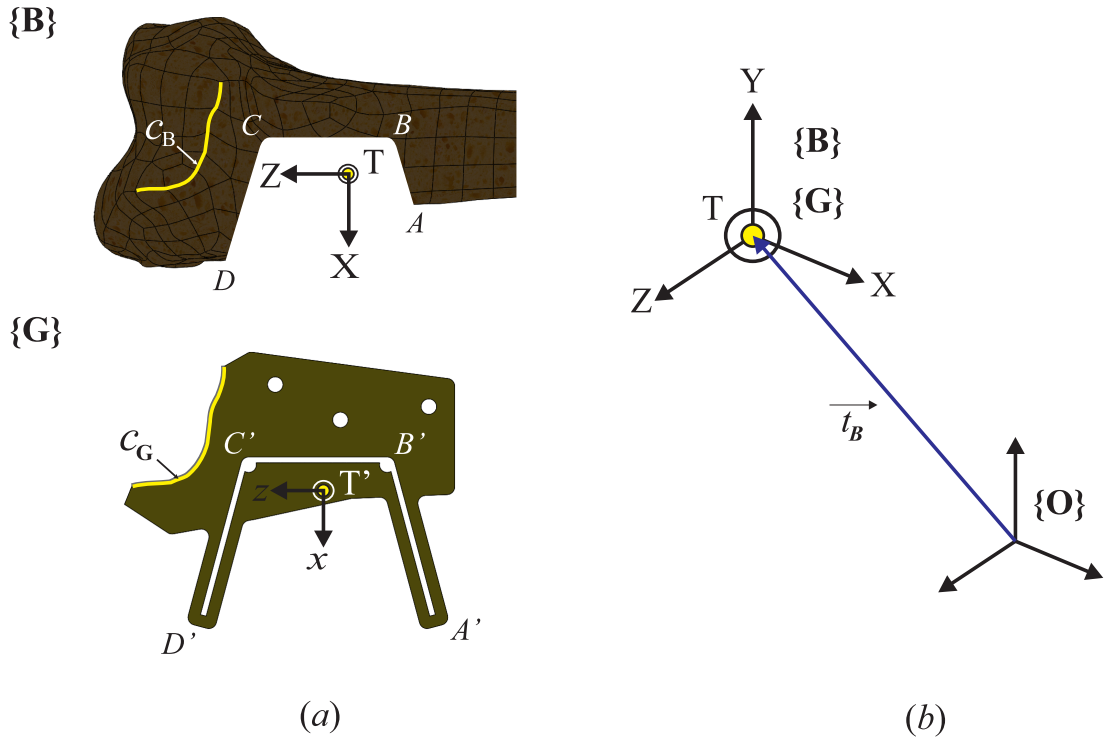

Figure 3.1: Coordinate frames used in the kinematic modeling (a) The coordinate frame $\{\mathbf{B}\}$ is located on the bone, and coordinate frame $\{\mathbf{G}\}$ is located on the cutting guide; the target tumor cell point is referred to as T to the $\{\mathbf{B}\}$ frame and T' to the $\{\mathbf{G}\}$ frame, as shown. Origin of $\{\mathbf{B}\}$ and $\{\mathbf{G}\}$ are located in T and T' correspondingly. (b) In an ideal case with perfect positioning, both coordinate frames $\{\mathbf{B}\}$ and $\{\mathbf{G}\}$will coincide with each other and reference the tumor point without discrepancy; that is, T and T' will coincide. An inertial frame $\{\mathbf{O}\}$ is used to reference the position of the target tumor cell point T with the vector $\overrightarrow{t_B}$

.

3.3 Positioning process and restrictions in the operating room

In the operating room (OR), after exposing the portion of the bone infected by the sarcoma, the surgeon must place the cutting guide on top of bone's surface. A correct positioning depends on how successfully the physician matches the two curves c_B and c_G as illustrated in Figure 3.1(a). This requires full exposure of bone's surface in order to look for the superior ridge of the medial femoral articular surface. Although the inclusion of a curve c_G in the guide serves as an aid during positioning, the positioning task still largely depends on the surgeon's ability to place it accurately.

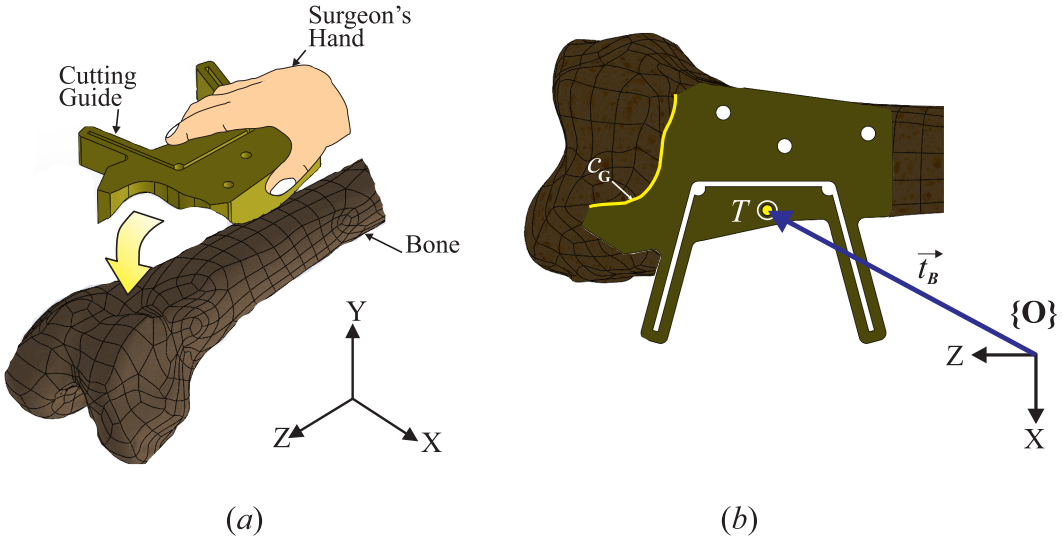

Figure 3.2: Cutting guide positioning process (a) Schematics showing placement of cutting guide on top of bone's surface by surgeon, and (b) after positioning, in an ideal case, tumor cell point T is targeted without discrepancy after perfect alignment of curves c_B and c_G; T position is defined by vector $\overrightarrow{t_B}$ with respect to the inertial frame $\{\mathbf{O}\}$

.

Figure 3.2 shows a schematic of the positioning process of the cutting guide on bone's surface. When the guide is in perfect position, *i.e.* c_B and c_G are aligned, the target point T' depicted in the cutting guide should coincide with the tumor cell T in the bone. However, two factors can cause the discrepancy between points the T and T',

(1) Soft tissue on the surface of the bone cannot be completely removed. While the guide is designed based on the naked bone's surface, any soft tissue will act as an uncertainty during placement that will cause positioning errors.

(2) Once the guide is in place, Steinmann pins are used to hold it; therefore, its relative movement with respect to bone is restricted during the actual resection using a sagittal blade. Such pin-locating process can also introduce positioning errors.

3.4 Kinematic modeling and error analysis

A cutting guide is treated as a rigid body in the following kinematic modeling. Every rigid body movement in the space can be described using three translations and three rotations with respect to a coordinate system, as described in Figure 3.3.

When the guide is reference by the $\{\mathbf{G}\}$ coordinate frame, it translates and rotates with respect to corresponding axes x, y and z with the following notation, as shown in Figure 3.3

- Δx**:** translation along the x axis
- Δy**:** translation along the y axis
- Δz**:** translation along the z axis
- **Roll:** rotation of an angle α with respect to the z axis
- **Yaw:** rotation of an angle β with respect to the y axis
- **Pitch:** rotation of an angle γ with respect to the x axis

After positioning, T and T' are not perfectly aligned due to the uncertainties described in Section 3.3. The misalignment between the two coordinate frames $\{\mathbf{B}\}$ and $\{\mathbf{G}\}$

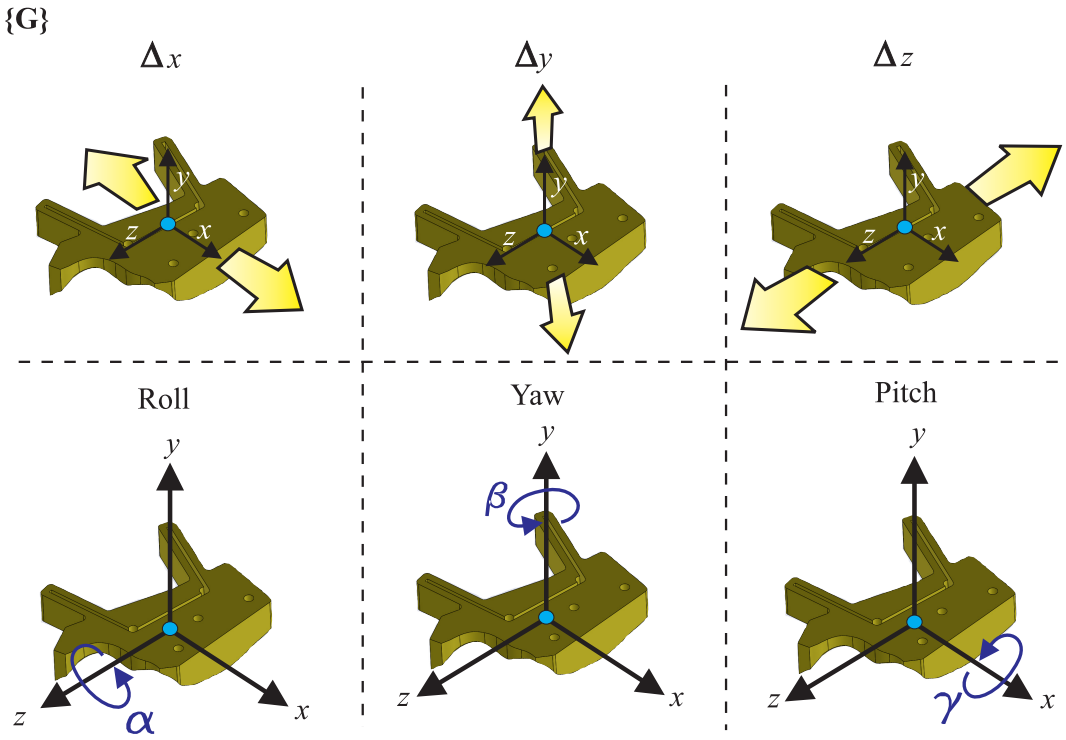

Figure 3.3: Cutting guide as a rigid body, having 6 degrees of freedom in the space; including three translation in the X, Y and Z directions and three rotations of roll, yaw, pitch, as shown.

can be described by the translational displacements of Δx, Δy and Δz, as well as the rotational displacements of α, β and γ. This can be modeled using a 4×4 homogeneous transformation matrix (HTM) ${}^{G}_{B}H$ with Euler angles along the *zyx* directions, which is equivalent to roll-yaw-pitch convention [24]:

$$\{G\} = {}^{G}_{B}H\{B\} \tag{3.1}$$

Equation (3.1) relates frame $\{\mathbf{B}\}$ and $\{\mathbf{G}\}$ using ${}^{G}_{B}H$ which is a homogeneous transformation with six degrees of freedom. The definition of ${}^{G}_{B}H$ is in the following [24]

$${}^{G}_{B}H = \begin{bmatrix} c\alpha\, c\beta & c\alpha\, s\beta\, s\gamma - s\alpha\, c\gamma & c\alpha\, s\beta\, c\gamma + s\alpha\, s\gamma & \Delta x \\ s\alpha\, c\beta & s\alpha\, s\beta\, s\gamma + c\alpha\, c\gamma & s\alpha\, s\beta\, c\gamma - c\alpha\, s\gamma & \Delta y \\ -s\beta & c\beta\, s\gamma & c\beta\, c\gamma & \Delta z \\ 0 & 0 & 0 & 1 \end{bmatrix} \tag{3.2}$$

where c and s represent cosine and sine respectively; that is, $c\alpha = \cos\alpha$, $s\beta = \sin\beta$, ... etc.

We define the origin of coordinate frames $\{\mathbf{B}\}$ and $\{\mathbf{G}\}$ using vectors $\overrightarrow{t_B}$ and $\overrightarrow{t_G}$ correspondingly, with respect to the inertial frame $\{\mathbf{O}\}$, as follows

$$\overrightarrow{t_G} = \begin{bmatrix} x_G \\ y_G \\ z_G \\ 1 \end{bmatrix} \qquad \overrightarrow{t_B} = \begin{bmatrix} X_B \\ Y_B \\ Z_B \\ 1 \end{bmatrix} \tag{3.3}$$

When the frame $\{\mathbf{G}\}$ is misaligned with the frame $\{\mathbf{B}\}$ by the movement of translation and rotation as define earlier in Figure 3.3, the homogeneous transformation matrix in Equation (3.2) can be employed to relate the vectors $\overrightarrow{t_B}$ and $\overrightarrow{t_G}$ defined in Equation (3.3). If we used the definition of the origin of such frames expressed in Equation (3.3) in combination with Equations (3.2) and (3.1), we obtain

$$\begin{bmatrix} x_G \\ y_G \\ z_G \\ 1 \end{bmatrix} = \begin{bmatrix} c\alpha\ c\beta & c\alpha\ s\beta\ s\gamma - s\alpha\ c\gamma & c\alpha\ s\beta\ c\gamma + s\alpha\ s\gamma & \Delta x \\ s\alpha\ c\beta & s\alpha\ s\beta\ s\gamma + c\alpha\ c\gamma & s\alpha\ s\beta\ c\gamma - c\alpha\ s\gamma & \Delta y \\ -s\beta & c\beta\ s\gamma & c\beta\ c\gamma & \Delta z \\ 0 & 0 & 0 & 1 \end{bmatrix} \begin{bmatrix} X_B \\ Y_B \\ Z_B \\ 1 \end{bmatrix}$$

Simplifying the equation, we have

$$\begin{bmatrix} x_G \\ y_G \\ z_G \\ 1 \end{bmatrix} = \begin{bmatrix} X_B c\alpha c\beta + Y_B(c\alpha s\beta s\gamma - s\alpha c\gamma) + Z_B(c\alpha s\beta c\gamma + s\alpha s\gamma) + \Delta x \\ X_B s\alpha c\beta + Y_B(s\alpha s\beta s\gamma - c\alpha c\gamma) + Z_B(s\alpha s\beta c\gamma - c\alpha s\gamma) + \Delta y \\ -X_B s\beta + Y_B c\beta s\gamma + Z_B c\beta c\gamma + \Delta z \\ 1 \end{bmatrix} \tag{3.4}$$

Equation (3.4) is the representation of vector $\overrightarrow{t_G}$. Therefore, x_G, y_G and z_G are the coordinates of point T', with respect to the $\{\mathbf{O}\}$ frame, after positioning the cutting guide on bone's surface.

As shown in Figure 3.4, let us define an error vector $\overrightarrow{e}$ as the error of the positioning of the cutting guide on the surface of the bone. The error vector $\overrightarrow{e}$ describes the discrepancy between T on the bone and T' on the cutting guide. This error could be minimize by introducing other aids during positioning, although the error $\overrightarrow{e}$ always exits in actual resection procedure.

It is convenient to model $\overrightarrow{e}$ as the radius of a sphere which we will call as the 'error zone' from now on. This error zone could be used to sketch the cutting path $\overline{ABCD}$, presented in Figure 3.1, during its design in order to ensure a negative margin resection (see Section 1.5) and overcome any error during cutting procedure. An illustration of this concept is presented in Figure 3.5. Mathematically, $\overrightarrow{e}$ could be expressed as:

$$\overrightarrow{e} = \overrightarrow{t_G} - \overrightarrow{t_B} \tag{3.5}$$

Equation (3.5) shows that $\overrightarrow{t_G}$ and $\overrightarrow{t_B}$ are needed to define $\overrightarrow{e}$. Values for $\overrightarrow{t_B}$, *i.e.* X_B, Y_B and Z_B, which define the location of tumor cell T, as the origin of coordinate frame

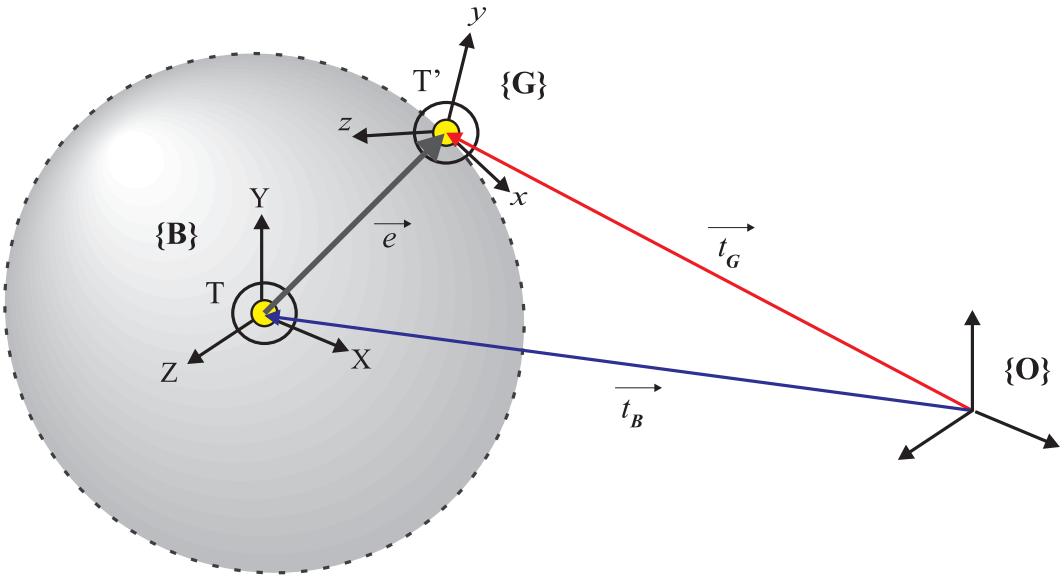

Figure 3.4: Coordinate frame $\{\mathbf{G}\}$ with the origin in T' after translations and rotations introduced during the positioning of the cutting guide, and the coordinate frame $\{\mathbf{B}\}$ with the origin in T showing the actual location of tumor cell; the error vector $\overrightarrow{e}$ is the difference between $\overrightarrow{t_G}$ and $\overrightarrow{t_B}$ with respect to the inertial frame $\{\mathbf{O}\}$

.

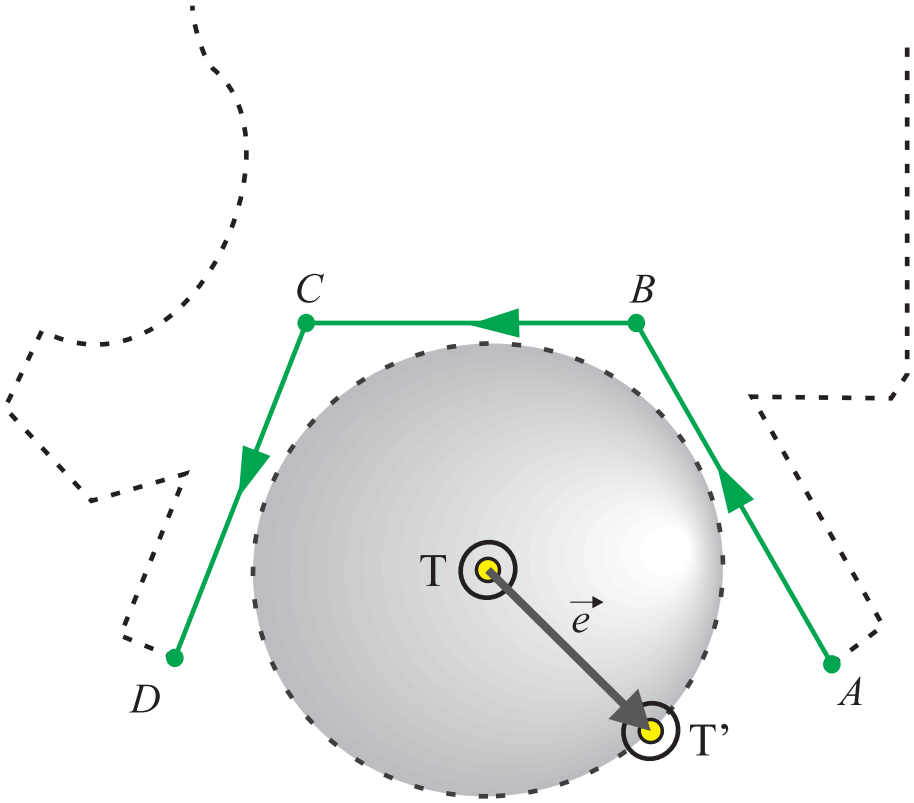

Figure 3.5: Error zone as an aid to plan the cutting path during design phase of cutting guides

$\{\mathbf{B}\}$, can be readily obtained from medical images such as CT scans. Equation (3.4) is the expression to obtain $\overrightarrow{t_G}$ and, although we already stated how to obtain X_B, Y_B and Z_B, we still need proper values for α, β, γ, Δx, Δy and Δz; that is, the values for the rotation and translation of the cutting guide with respect to the bone. A proper way to obtain these values is through experiments and statistical analysis. Peaks and average values can be substituted into Equations (3.4) and (3.5) to inspect the behaviour of $\overrightarrow{e}$ under different conditions. The main idea is to control and minimize $\overrightarrow{e}$ and give surgeons a 'magic number' that allows successful resection of the tumor cell without touching it during cutting procedure.

A experimental study to obtain the rotation and translation values is presented in the next section.

3.5 Experimental Study: Improving accuracy by accounting for soft tissue

In order to obtain proper values for α, β, γ, Δx, Δy and Δz, as explained in Section 3.4, an experimental study is conducted. The main objective is to obtain maximal and average values for translations and rotations of the cutting guide with respect to the bone after positioning. As stated before, the positioning error quantified as $\overrightarrow{e}$ in Equation (3.5), is introduced when placing the cutting guide onto the surface of the bone. It is our objective to improve the design of cutting guides in order to limit the negative impact of soft tissue. By introducing necessary built-in features, such as small spikes, to achieve this, four different designs will be tested and two different bone-surface conditions will be simulated and studied.

3.5.1 Experimental setup and procedure

A 3D digital image of a femur (Sawbones, Vashon Island, WA) was obtained using a clinical CT scanner. Four types of cutting guides were designed and fabricated by a 3D printer based on the digital representation. Each guide has different features to be tested

for their ability to overcome randomly distributed soft-tissue, allowing the guide to place properly with minimum error of translation and rotation with respect to the bone surface.

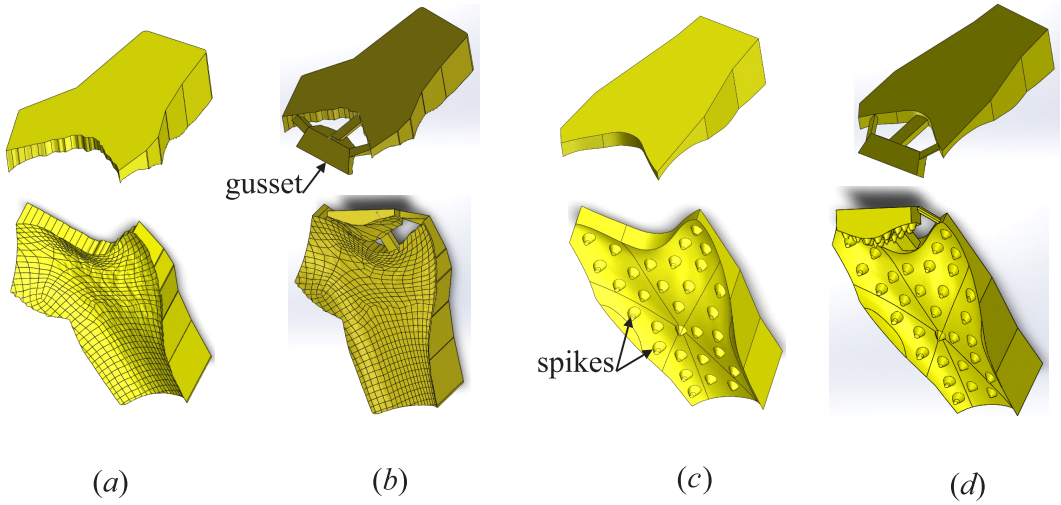

Figure 3.6: Different types of cutting guides used in positioning experiment (*a*) standard, with no features, (*b*) standard with gusset, (*c*) surface with distributed spikes, and (*d*) surface with distributed spikes and gusset

Figure 3.6 shows four different configurations of the cutting guide designs. They are described as follows.

(1) **Standard (Figure 3.6*a*):** a typical cutting guide with no extra features on the contact surface, similar to the guides used in the experiments of Section 2.4.1

(2) **Standard with gusset (Figure 3.6*b*):** the standard guide with an add-on feature at the top to help the user in positioning, with an extra feature called 'gusset'

(3) **Surface with distributed spikes (Figure 3.6*c*):** the standard guide with multiple miniature spikes randomly distributed throughout the contact surface of the guide; these spikes are designed to help the guide to penetrate any soft tissue on the bone surrounding the resection area to minimize the positioning errors due to the presence of soft tissues

(4) **Surface with distributed spikes and gusset (Figure 3.6*d*):** the standard guide including spikes on the contact surface and a gusset

Ten different subjects, five men and five women, with no previous training on guide positioning were asked to place each type of the guides over the femur bone surface under two conditions

(1) a clean and smooth surface

(2) a simulated tissue-covered surface

Small pieces of modeling clay were randomly placed on the surface of the femur bone to simulate soft tissue, as illustrated in Figure 3.7(*b*).

(*a*) (*b*) (*c*)

Figure 3.7: Different bone-surface conditions for positioning experiment (*a*) smooth surface, and (*b*) tissue-covered surface using modeling clay. Cutting guide in contact with a femur bone is shown in (*c*).

After positioning, the femur with the positioned guide were CT-scanned to quantify the relative position of the guide with respect to the femoral surface. A STL file with a three dimensional digital representation of the cutting guide placed over the bone's surface was obtained for each case. Reverse engineering was carried out with an identical procedure as that described in Section 2.2 to obtain a CAD-based file from which rotations and translations were measured.

3.5.2 Calculate rotations

Each file of the experiments was analyzed using CAD tools to accurately calculate the relative rotation of the top surface of cutting guide with respect to the surface of the bone. A coordinate frame $\{\mathbf{B}\}$, for the bone, is defined with coordinates XYZ, as shown in Figure 3.8. A plane formed by the three points P_1, P_2 and P_3 of the CAD solid model on the top surface of the cutting guide defines a frame $\{\mathbf{G}\}$. Rotations α, β and γ are then obtained by the rotation of $\{\mathbf{G}\}$ with respect to $\{\mathbf{B}\}$. Angles α and β were obtained by projecting a vector $\overrightarrow{m}$, normal to the defined plane, into each Cartesian plane XY and YZ. To calculate γ, the rotation of the vertical cutting slot was used in order to obtain the orientation of the cutting guide in the XZ plane as illustrated in Figure 3.8(b).

3.5.3 Calculate the X and Z translations

In order to calculate the translation of the cutting guide with respect to the bone along the Cartesian axes X and Z. We take advantage of another landmark printed on the guides — the three fiducial holes for Steinmann pins. These holes were originally printed on the cutting guide to allow for drilling the locating holes on the bone to secure the guide in place with Steinmann pins once it was positioned on the bone by the surgeon. Since they are drilled into the bone, we compare the position of the holes left in the specimen, obtained by reverse-engineering CT-scan images, with their corresponding ideal position of CAD solid model design.

Three fiducial holes (1 for proximal, 2 for middle and 3 for distal) made on the cutting guide are shown in Figure 3.9. The position of the center of each hole was extracted from CT-scan image, from which a triangle was formed. The coordinates of the centroid of this triangle before guide positioning (ideal location with the CAD model) was compared with the actual location of the triangle after placing the guide on the surface of the bone.

Note that the vector $\overrightarrow{d}$ provides not only the linear displacements along the X and Z directions, but also the angular displacement, β, with respect to the Y dirction. The yaw

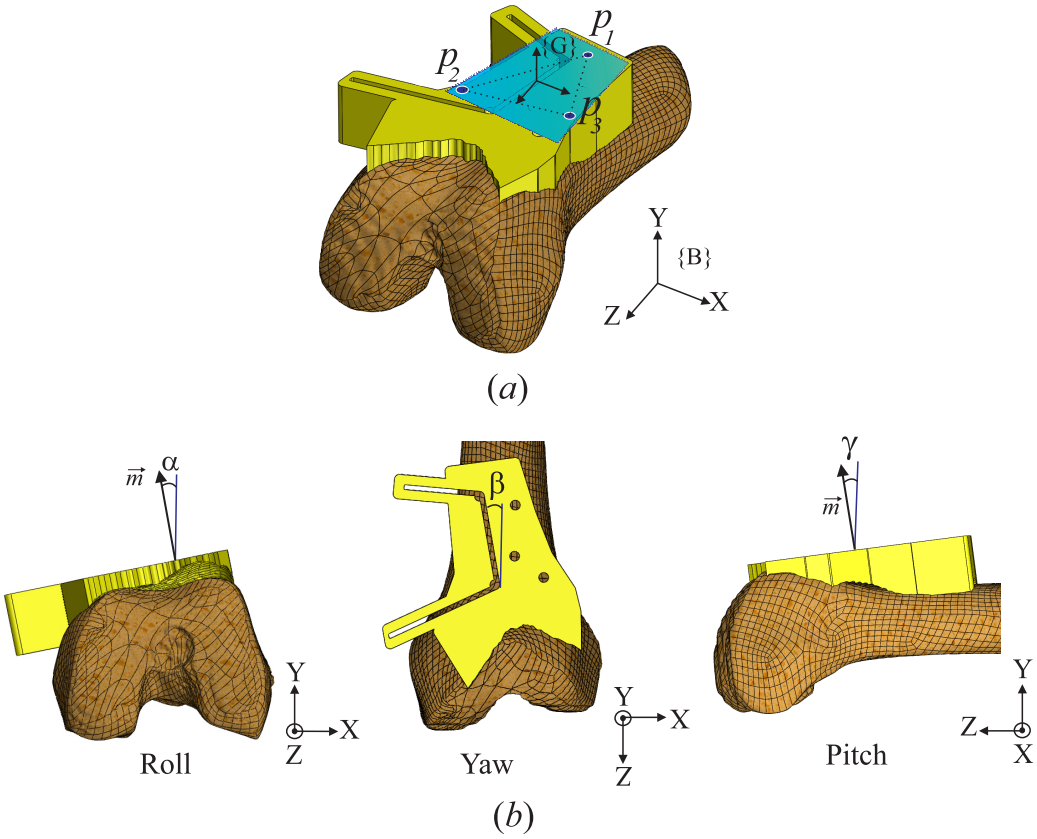

Figure 3.8: Calculating rotations of cutting guide after positioning (a) defining a plane using three fiducial points: P_1, P_2 and P_3 from the top surface of cutting guide, and (b) definition of angles for roll (α), yaw (β) and pitch (γ)

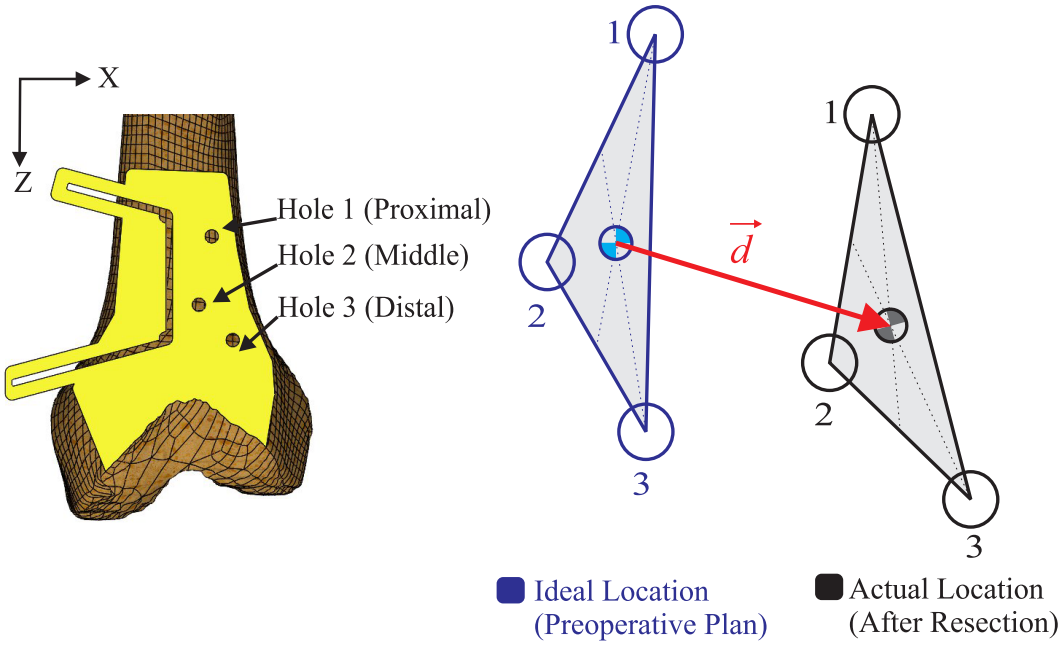

Figure 3.9: Calculating the X and Z translations of cutting guide before and after the placement of the guide on the surface of the bone, using CT-scans and Steinmann pins holes

angle should be the same as that obtained in Figure 3.8. The results are presented in Section 3.6.3.

3.5.4 The Y translation

Prior to the resection, the surgeon presses the cutting guide against the bone surface along the negative Y direction, as shown in Figure 3.10. Due to the randomly distributed tissue on the surface of the bone, typical of an operation procedure, the cutting guide can not make a perfect contact with the surface of the bone, as designed and intended by the CAD solid model. As a result, an error in the Y direction due to soft tissue will occur. The displacement of the cutting guide along the Y direction due to the soft tissue can be estimated intraoperatively during surgery.

Cases where soft tissue is also compromised by a tumor cell requires special consideration to coordinate between the design of cutting guide and the preoperative plan. For such cases, the compromised portion of soft tissue cannot be removed during the operation. A pre-determined offset in the Y-direction must be used based on the CT scan images. This will lead to an inevitable error in the Y direction. Further study is needed to render a fair estimate of error in the Y-direction for such special case, from the CAD model, guide design, to the preoperative plan and *in-situ* operation.

3.6 Results of experimental study

The results of experimental study are presented in the following subsections. The results of rotations α, β, and γ are presented in Section 3.6.1, followed by results of translational displacement in the X and Z directions in Section 3.6.2. In Section 3.6.3 we compare the yaw angle β obtained in Section 3.6.1 and the angular displacement obtained from the rotation of the triangle on the surface of the guide (Section 3.5.3).

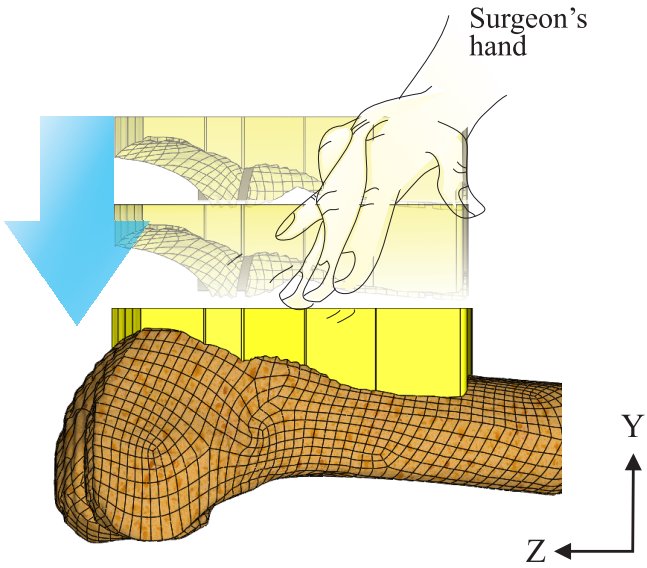

Figure 3.10: Translation of cutting guide along the *Y* axis; surgeon presses the cutting guide against the surface of the bone prior to the resection

3.6.1 Results of rotation

The mean values and standard deviations (SD) of each of the rotation of roll, yaw and pitch, were obtained from experiments. First, a comparison between each type of cutting guide designs in Figure 3.6 is presented in Table 3.1, using the smooth bone surface in Figure 3.7(*a*). In this scenario, the design with spike points reported smaller rotational errors after positioning in the direction of roll. For the yaw component, the gusset design showed smaller rotational errors after positioning. In the direction of pitch, the design with spike points reported, again, smaller rotational errors .

When the average of the mean values are taken for the roll, yaw and pitch directions to quantify the rotational errors, the pitch direction reports the maximum error with 2.37°, as shown in Table 3.1.

	Roll α		Yaw β		Pitch γ	
	Mean	SD	Mean	SD	Mean	SD
Standard	0.75	1.45	0.33	0.95	2.21	1.12
Gusset	1.02	1.32	0.63	1.73	2.45	0.74
Point	0.03	2.14	3.25	1.14	1.95	0.47
Point+Gusset	2.47	0.72	3.12	1.47	2.88	0.82
Average	1.067		1.83		2.37	

Table 3.1: Mean and standard deviation (SD) of the errors of rotation after positioning on smooth surface of the bone (*cf.* Figure 3.7*a*). All values are in degrees.

Table 3.2 shows the results for the case where bone was covered with soft tissue, as in Figure 3.7(*b*). The design with spike points again shows the smallest rotational errors after positioning for both roll and pitch directions. For the yaw component, the standard design reported the minimum rotation.

Finally, in order to analyze the influence of the soft tissue in the positioning process, Table 3.3 presents the total average of the mean values of the rotational errors in the roll, yaw and pitch directions for every type of guide in Figure 3.6. The difference of values

	Roll α		Yaw β		Pitch γ	
	Mean	SD	Mean	SD	Mean	SD
Standard	1.25	2.47	0.42	1.15	2.75	1.12
Gusset	1.41	0.95	0.78	2.12	3.02	0.53
Point	0.04	1.86	3.41	1.97	2.18	0.55
Point+Gusset	2.77	1.24	4.25	0.74	3.26	1.19
Average	1.37		2.21		2.80	

Table 3.2: Mean and standard deviation (SD) of the errors of rotation after positioning on tissue-covered surface of the bone (*cf.* Figure 3.7*b*). All values are in degrees.

between the errors of rotation for the case with smooth surface (Figure 3.7*a* and Table 3.1) and those for the case with soft tissue on surface (Figure 3.7*b* and Table 3.2) were calculated. The design with spike points has the smallest difference, indicating that this design performs better under the presence of soft tissue.

Two interesting observations from these results are in order

(1) The magnitudes of errors of rotation do not exceed 5 degrees in all cases.

(2) Considering average of the mean values, the rotational errors in the pitch direction are larger, follow by yaw and pitch, in both smooth surface and tissue-covered surface.

3.6.2 Results of translation

Similar to Section 3.6.1, the mean values and standard deviation (SD) of the errors in the X, Y and Z directions were obtained. First, a comparison among each type of cutting guide is presented for the case of smooth surface in Table 3.4. In this scenario, the gusset design reports the smallest translational errors along the X and Z axes after positioning, as shown in Table 3.4.

The results for the tissue-covered case are presented in Table 3.5. As expected, the standard guide has the largest errors for translation in both axes, as compared with the the

Type	Smooth-surface Table 3.1	Tissue-covered Table 3.2	Difference
Standard	1.47	1.09	0.38
Gusset	1.74	1.37	0.37
Point	1.88	1.74	0.14
Point+Gusset	3.43	2.82	0.61

Table 3.3: Influence of soft tissue in positioning errors; showing the average of the mean values of the rotational errors for different type of guides

	X		*Z*	
	Mean	SD	Mean	SD
Standard	-1.41	1.54	-1.55	0.96
Gusset	0.76	2.16	-0.45	2.78
Point	1.34	1.25	-1.15	1.77
Point+Gusset	2.36	-2.97	-0.73	2.62
Average	0.76		-0.97	

Table 3.4: Mean and standard deviation (SD) of the errors in translation after positioning on smooth surface of the bone (*cf.* Figure 3.7*a*). All values are in *mm*.

other types. This is mainly because it did not have any feature that allows it to overcome the topological discrepancy that soft tissue introduces to bone's surface.

For both smooth and tissue-covered cases, the guides that have gussets report smaller errors in translation along the X and Z axis. This was also expected as the gusset provides restriction of the movement of the guide.

	X		Z	
	Mean	SD	Mean	SD
Standard	-2.78	2.45	-1.62	0.96
Gusset	0.89	1.89	-0.56	2.78
Point	1.04	0.87	-1.18	1.77
Point+Gusset	2.06	0.99	-0.75	2.62
Average	0.30		-1.03	

Table 3.5: Mean value and standard deviation (SD) of the errors in translation after positioning on the tissue-covered surface of the bone (*cf.* Figure 3.7*b*). All values are in *mm*.

3.6.3 Results of the yaw angle

The rotational error in the yaw direction was calculated using two approaches. According to Section 3.5.2 the orientation of the vertical cutting slot in the guide was considered, as presented in Figure 3.8(*b*). Also, as described in Section 3.5.3, the rotation in the yaw direction was calculated using the three fiducial holes for Steinmann pins and the vector $\overrightarrow{d}$ according to Figure 3.9. Results for both approaches, in the smooth-surface case, are shown in Table 3.6 as well as the difference between them for each type of cutting guide. The small difference values evidence consistency between both cases.

3.7 Revisit the kinematic modeling

The average of the mean values of the experimental results presented in Tables 3.1 and 3.2 are good choices for α, β, γ, Δx, Δy and Δz in Equations (3.4) and (3.5). These

Type	Figure 3.8(b)	Figure 3.9	Difference
Standard	0.33	0.41	0.08
Gusset	0.63	0.67	0.04
Point	3.25	3.33	0.08
Point+Gusset	3.12	3.20	0.08

Table 3.6: Comparison of results of rotational error in the yaw direction using the approach depicted in Figure 3.8(b) vs. the procedure presented in Figure 3.9. All values are in degrees.

values from experiments can be substituted into Equation (3.4) to obtain $\overrightarrow{t_G}$, which can be used to calculate the values of the error vector $\overrightarrow{e}$ by means of Equation (3.5).

The goal is to quantify the error vector $\overrightarrow{e}$ with respect to the errors in translation and rotation introduced during positioning process. From Section 3.6.1, we experimentally estimate that cutting guides tend to rotate more with respect to x-axis, *i.e.* pitch rotation or γ. However, what is the influence of this rotation over the position of T' (*cf.* Figure 3.4) it is yet not clear. An analysis of the position of T' for different scenarios, *i.e.* variation of α, β and γ, is conducted in the following section.

3.7.1 Behavior of the error vector according to kinematic model

Equations (3.4) and (3.5) were used to analyzed various scenarios considering only rotation of the cutting guide with respect to the bone. Figure 3.11 shows the magnitude of $\overrightarrow{e}$ when each of the α, β or γ are varying from -15° to 15°[1] while the other two angles are fixed at zero. This is an ideal case for the parameter study where the guide is only rotating with respect to one axis. The plot in Figure 3.11 appears to show only one curve; however, the three curves, one for each case, are coincident with one another based on the arrangement of simulation in this parameter study. The plot shows a sinusoidal behavior of $|\overrightarrow{e}|$ with minimum values equal to zero, indicating that the error $\overrightarrow{e}$ could vanish with

[1] Although it was shown by the experimental data in Section 3.6.1 that none of the rotation errors reach a value greater than 5°, we have chosen the rante of simulation from -15° to 15° for investigating a broader range of the behavior and patterns of $\overrightarrow{e}$

certain combination of the parameters.

However, if we inspect how T' is moving when α, β or γ is varying, the result will show that only if we vary α, *i.e.* if we 'roll' the guide, we can target our tumor cell T. This is shown in Figure 3.12.

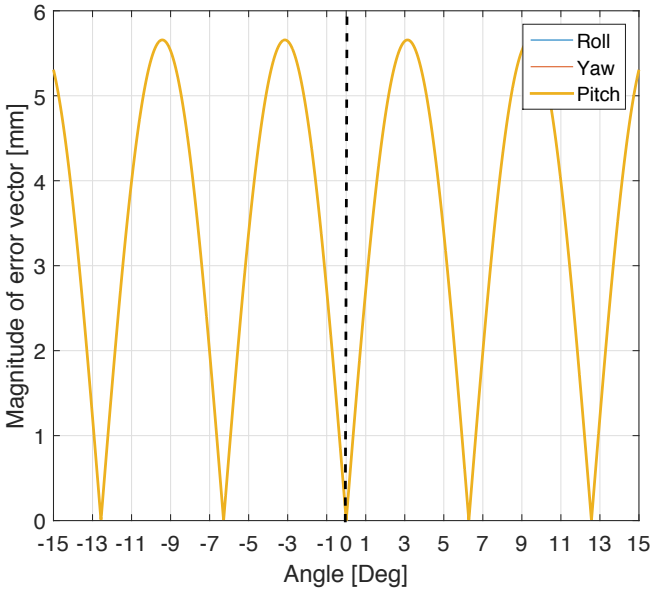

Figure 3.11: Magnitude of $\overrightarrow{e}$ with respect to cutting guide rotations. Three overlay curves in which one angle varies and the other two are fixed at zero.

Figures 3.11 and 3.12 represent a simulation of an ideal case, we can move forward to a more realistic scenario using the average values obtained in Section 3.6.1. Figure 3.13 is showing the variation of $|\overrightarrow{e}|$ when α, β or γ is varying. The other two angles that are not varying are fixed at the average values from Table 3.2. For this case, it is interesting to observe that, if the guide is rotated either with respect to z (roll) or x (pitch) axes, the magnitude of $|\overrightarrow{e}|$ is greater. Only for yaw rotation, $|\overrightarrow{e}|$ outcomes smaller values.

Finally, by constructing the trajectory of T' we obtain Figure 3.14 in which T, the location of the tumor cell, it is also shown. Under this more realistic scenario, T' would never overlay with T and, therefore, there will always be an error that needs to be accounted for, according to Figure 3.5. The mathematical model from Equations (3.4) and (3.5) would

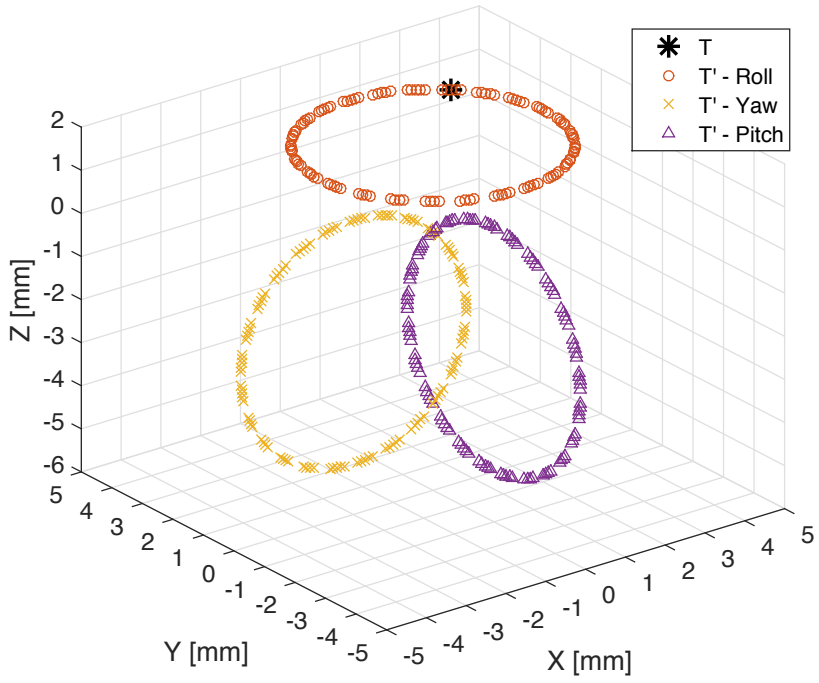

Figure 3.12: Trayectory of T' for different rotations. For each ellipsoid, one angle varies and the other two are fixed in zero.

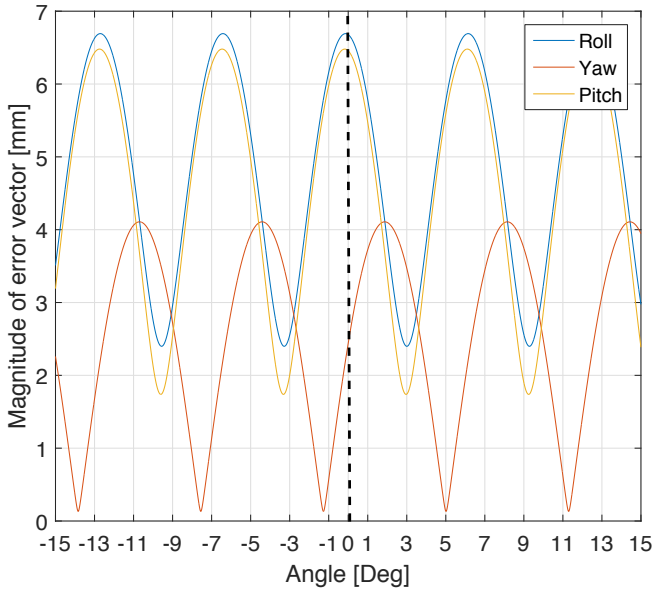

Figure 3.13: Magnitude of $\overrightarrow{e}$ with respect to cutting guide rotations. For each curve, one angle varies and the other two are fixed in corresponding average of mean values presented in Table 3.2

help to estimate this error during cutting guide design considering the anatomy of the patient and the average values obtained in Section 3.6.1. A more conservative design would consider maximum values instead of average values.

3.7.2 Estimation of error vector based on experiments

The error vector $\overrightarrow{e}$ is defined by Equation (3.5), which is a function of the rotation and translation components of the cutting guide after positioning. A fair estimation of the final value of $\overrightarrow{e}$ could be obtained by plugging the average results obtained in Tables 3.2 and 3.5 into Equations (3.4) and (3.5). Also, the translation along the Y axis was estimated in 2 *mm*, according to the considerations explained in Section 3.5.4.

$$\overrightarrow{e} = \overrightarrow{t_G} - \overrightarrow{t_B} = \begin{bmatrix} 0.98X_B - 0.022Y_B + 0.049Z_B + 0.30 \\ 0.041X_B - 0.98Y_B - 0.037Z_B + 2 \\ -0.049X_B + 0.039Y_B + 0.98Z_B - 1.03 \end{bmatrix} - \begin{bmatrix} X_B \\ Y_B \\ Z_B \end{bmatrix} \tag{3.6}$$

Equation (3.6) returns the actual coordinates of the error vector $\overrightarrow{e}$ based on the coordinates of the tumor defined by $\overrightarrow{t_B}$. The position of the tumor cell could be readily obtained using the CT-scan images of the patient after the corresponding reverse engineering process.

Therefore, Equation (3.6) could be used while prepareing for the preoperative plan, specifically to trace the cutting path to minimize that the risk of touching the tumor during resection. Figure 3.15 is an schematic showing how an original cutting path $\overline{ABCD}$ is corrected by accounting for the error vector into a new cutting path $\overline{A'B'C'D'}$ which will eliminate any possibility of touching the tumor cell during the resection. Although this will definitely increase the amount of healthy soft tissue that will be removed, eliminating the risk of an error during resection is far more crucial as involves patient's health. In fact, current resection techniques in which cutting guides are not in use require to consider a greater margin of error [4].

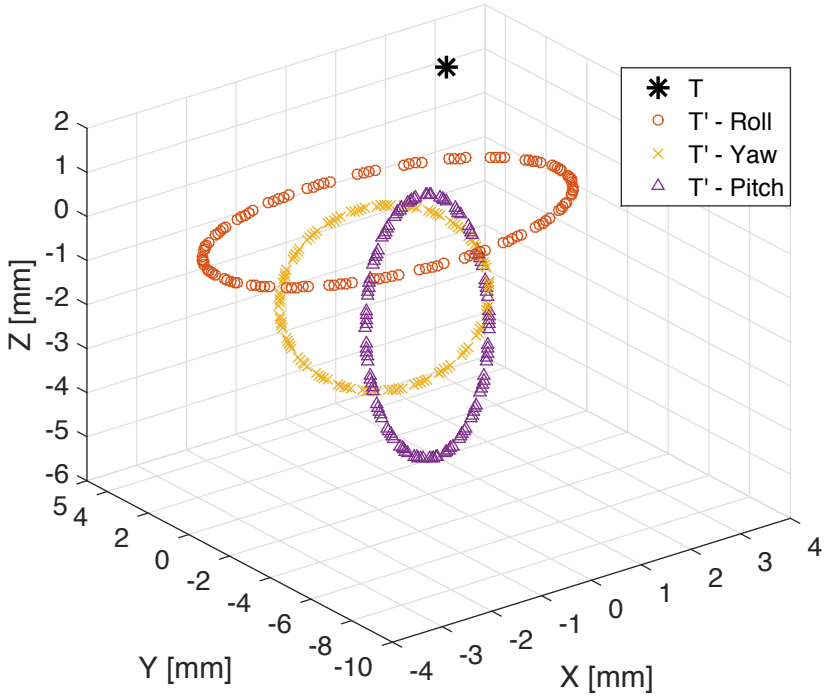

Figure 3.14: Trayectory of T' for different rotations. For each ellipsoid, one angle varies and the other two are fixed in average values.

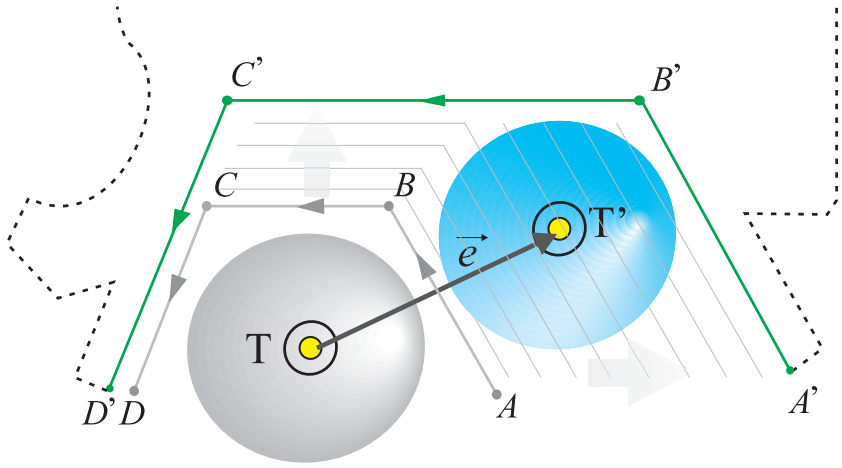

Figure 3.15: Original cutting path trayectory $\overline{ABCD}$ changes after accounting for error vector into new cutting path $\overline{A'B'C'D'}$

3.7.3 Discussion

The errors of rotations and translations with respect to the three axes due to positioning of cutting guides on the surface of the bone were measured for each type of guide and the for each cases of smooth surface (Figure 3.7*a*) and surface covered with soft tissue (Figure 3.7*b*). On average, the absolute difference of magnitude of rotation error between smooth and tissue-covered surfaces for the four different guide designs were

- Standard $= 0.38^{\circ}$
- Gusset $= 0.37^{\circ}$
- Point $= 0.14^{\circ}$, and
- Point+Gusset $= 0.61^{\circ}$

The results indicate that in all four types of guides, the presence of soft tissue influenced guide positioning. The feature added to Guide 3, equally spaced peaks for point contact, successfully diminished the effect of soft tissue. If we analyzed purely translation of the guides, soft tissue roll is not statistically significant. The analysis of translation along Y axis is special as it is not influenced by surgeon's hand skills during positioning, but the amount of soft tissue left around bone's surface which could be measured from patient's medical images.

Positioning of computer-generated cutting guides for tumor resection is significantly influenced by the presence of soft tissue. However, guides can be designed with additional features that help to overcome this issue leading to a more accurate placement and, therefore, a more precise resection of bone sarcomas.

3.8 Summary

The presented mathematical model aids in the estimation of the error introduced during positioning of cutting guide over bone's surface. With the maximum and average

values obtained in the experimental study, the error could be accounted for during cutting guide design. Equation 3.6 is proposed to calculate the error vector $\overrightarrow{e}$ based solely on the position of the tumor. Estimation of $\overrightarrow{e}$ is crucial while sketching the cutting path during preoperative plan since it will allows the surgeon to rely on resection using cutting guides as the risk of touching the tumor during surgery has been accounted for.

According to our mathematical model, it is impossible to completely vanished $\overrightarrow{e}$. It is possible, however, to account for it before the surgery procedure. In the next chapter we are proposing a novel technique to maintain $\overrightarrow{e}$ within our calculated limits intraoperatively.

Since we are using average values to proposed Equation 3.6, there is still a slight chance that surgeon fails to position the cutting guide resulting in a greater error than the calculated one. A new technique that allows the surgeon to quantify its positioning error during surgery is proposed and validated in Chapter 4.

Chapter 4

Intraoperative Technique to Accurately Position Cutting Guides

4.1 Introduction and justification

In Chapter 2 we studied the accuracy of osteosarcoma resection using cutting guides as compared to typical and current manual resection techniques, showing that although guide-assisted resection is more accurate and precise, it still requires that the errors be quantified and accounted for. In Chapter 3 we studied the contribution of errors from the process of positioning cutting guides on top of the bone. We also introduced a kinematic model that allows the preoperative-planner to quantify the errors based on the actual positioning of the guide as compare to an ideal configuration. Due to the inevitable errors introduced by human factor, we can not solely depend upon the preoperative plan and kinematic model accuracy of positioning before the actual surgery. If there is a slight probability that surgeons position the guide with an error beyond the preoperative limits and parameters, the procedure is likely to present a real risk to the patient.

Therefore, other means to increase the accuracy of cutting guide's positioning during the resection need to be explored and proposed. In addition, they should be accurate, simple, inexpensive and compatible with current standards in OR. It might be obvious to think about sophisticate robotic devices, such as da Vinci Surgical System (SIC), as they offer greater accuracy than human hand; however, they are expensive, bulky and require a

a special configuration of OR with a steep learning curve to operate devices[25]. Other options might include the use of real-time 3D scanners, optical sensors or lasers. For all those, a foreign device needs to be introduced in the OR which involves additional arrangement and training, FDA approvals, etc., that may render it impractical.

Under this context, we will introduce a technique that takes advantage of a device which surgeons carry with them — their smartphones. Furthermore, we also present image processing techniques to extract the orientation of the cutting guide after the positioning using pictures taken by the camera of smartphones.

4.2 Digital image processing technique to quantify accuracy of cutting guide positioning

As stated earlier, our main objective is to use image processing techniques to extract information about the positioning of the cutting guide from a picture of the bone with the guide placed on top. The long-term goal will be to create a smartphone application that will process the picture taken by a surgeon in the OR and returns the relevant results to the doctor to correct the position according to the specific limits specified in Equation (3.6). Current smartphones cameras are powerful enough to take high-resolution still photos. In the subsequent sections, we will address the following questions:

- How do we extract the positioning information of the guide from a still photos?
- What kind of image processing techniques do we utilize to obtain such information?

4.2.1 Defining a digital image

By definition, any digital image can be analyzed as a two or three dimensional function, depending on the nature of such image. If the image is two dimensional (2D), then it can be treated as a 2D-array or matrix where every pair of coordinate (x_n, y_n) of that matrix

is called a *pixel* which is allocated with a value of brightness or intensity. For simplicity, we will consider only gray-scale images, meaning that every pixel of the picture is going to have an intensity between 0 (100% black) and 255 (100% white), resulting in a total of 256 levels of gray scales per every pixel, as presented in the example in Figure 4.1. Converting any full-color image into gray-scale is easy as it is a common option in most image-processing available software such as Matlab (MathWorks, USA).

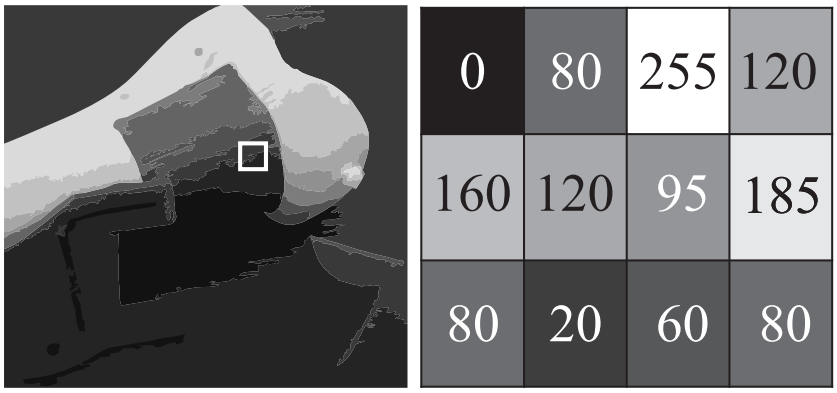

Figure 4.1: The concept of a digital gray-scale image (a) A digital image showing a small square of 4x3 pixels, and (b) an enlargement of such square as a two dimensional array where every coordinate receives a brightness value from 0 (100% black) to 255 (100% white)

4.2.2 Digital image processing and boundary tracing

The next step is to extract relevant information from the gray-scale image, meaning the rotation (α, β and γ) and translation (x and z)[1] of the cutting guide with respect to the bone within the frame defined in Section 3.2. We used physical markers in the guide, as presented in Figure 4.2, to track its position and quantify the corresponding rotations and translations. Our image processing code must include means to extract information from those circular markers, such as the cartesian coordinates of corresponding centers, post-process those coordinates and calculate values of rotation and translation.

[1] See Section 3.5.4 for translation along y axis.

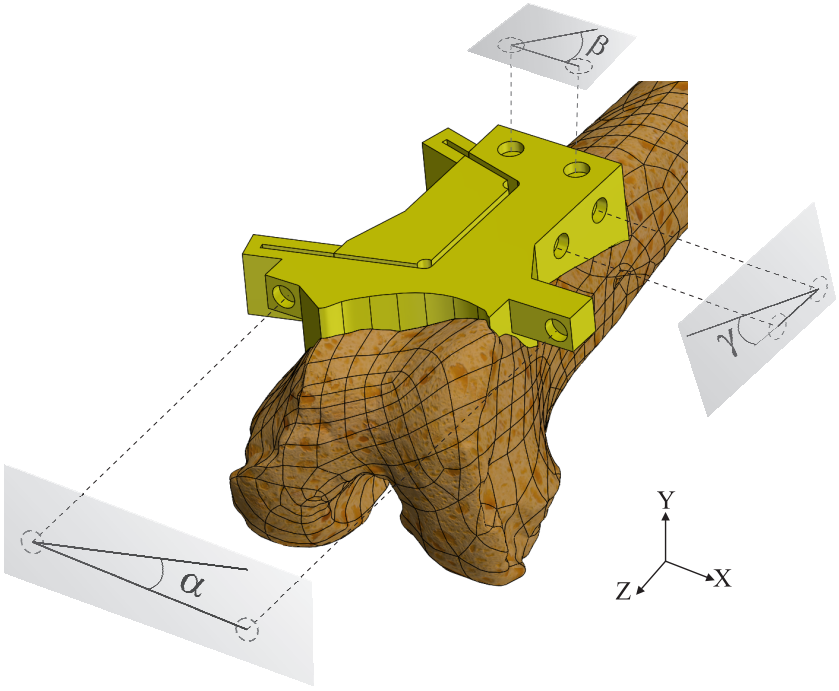

Figure 4.2: The use of markers in the cutting guide to record its position. Circular markers are placed in the guide to extract center coordinates and calculate the rotation and translation of the cutting guide after positioning by surgeon.

In order to detect meaningful objects (*i.e.* circular markers) in a picture, a conversion from full-color to gray-scale is required, as presented in Figure 4.3, from (*a*) to (*b*). This will help to distinguish any marker placed on the cutting guide from everything else in the photo. Depending on the selection for the colors, after gray-scale transformation, the circular markers will be highlighted in the image as they contrast from their surrounding area (*i.e.* the cutting guide). Therefore, it is important to select opposite colors that will contrast well after conversion.

After proper detection, extraction of the coordinates of the circular markers will follow using *boundary tracing* technique, as shown in Figure 4.3(*c*) and (*d*). Essentially, this technique takes advantage of the high contrast between marker and its surroundings achieved in the previous step. As every pixel in the image is associated with a gray-brightness, this procedure scouts for big changes in brightness level from one pixel (A) to another (B), as presented in Figure 4.4. Once a big change is found, it is consider as a boundary point. From there, the tracing algorithm follows the boundary assuming a closed shape and finds the coordinates for the rest of the points that constitute such perimeter by searching for similar changes in subsequent pixels. This algorithm ends when the initial point (B) is reached again. The process starts again to find a new change and, therefore, the contour for the other circular marker is identified.

The centers of the circular markers can be calculated based on the results of the image processing. Finally, the line connecting the two centers will be compared to the reference in the bone to determine the angles of rotation and translation. The process is repeated to calculate all three angles α (XY plane), β (XZ plane), and γ (YZ plane) as shown in Figure 4.5 and according to the same setup of the coordinate frames made in Section 3.2. In our case, we used bone landmarks as a reference. For example, for the XZ and YZ planes, the longitudinal axis of the bone could be extracted using the same boundary tracing technique. This longitudinal axis reveals the orientation of the bone in such plane. In the YX plane (frontal view), we traced a horizontal line in the patellar surface of the bone. However, this

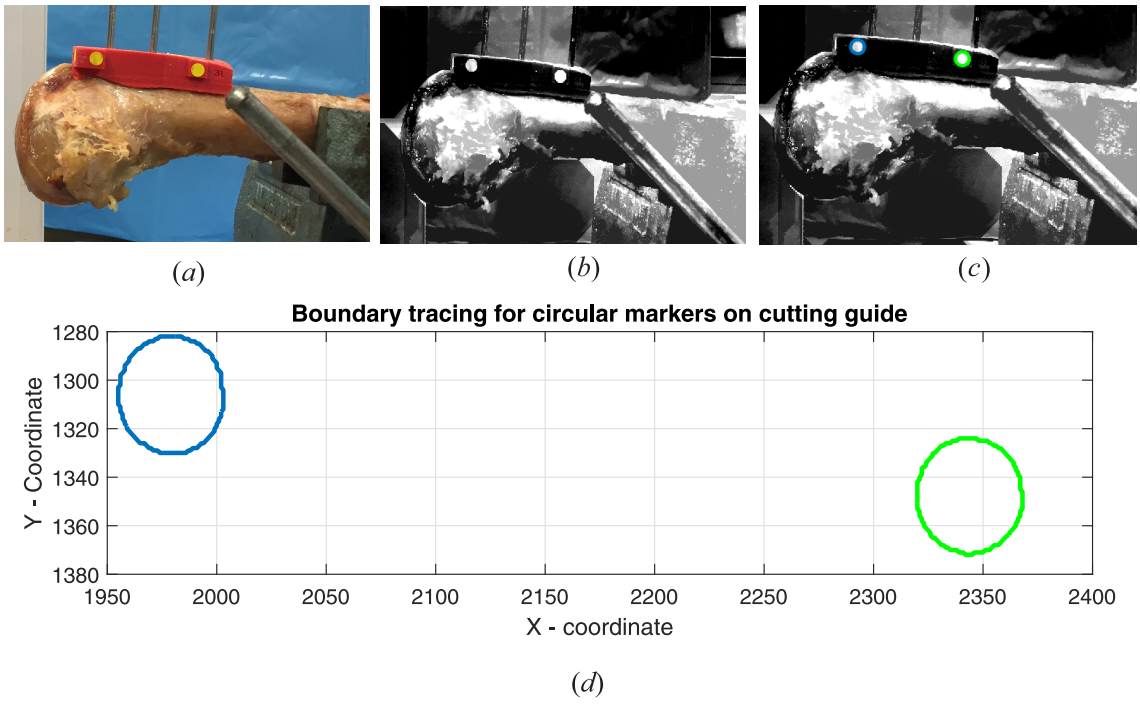

(*a*) (*b*) (*c*)

(*d*)

Figure 4.3: Digital image processing steps for marker extraction (*a*) full-color original image, (*b*) gray-scale image, (*c*) boundary tracing to extract circular markers on guide and, (*d*) plotting of extracted points from circular markers

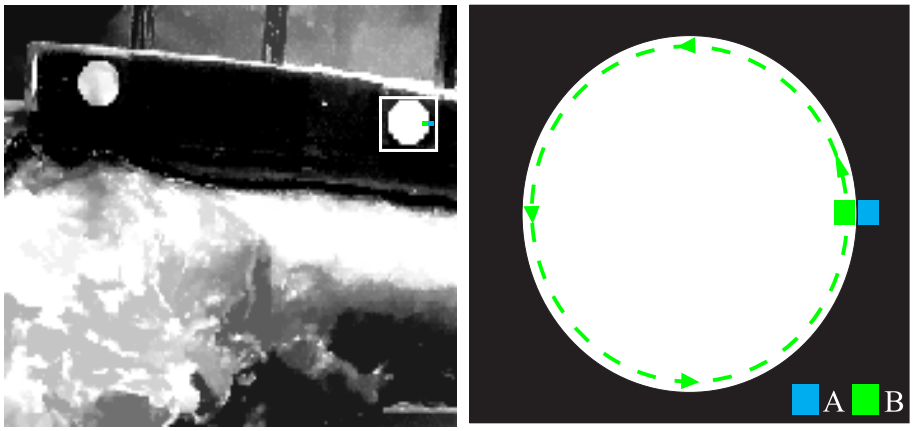

(*a*) (*b*)

Figure 4.4: Boundary tracing technique (*a*) gray-scale image showing a square surrounding one circular marker on the guide, and (*b*) the sketch representing the detection process: after finding a change in brightness from point A to B, the code scouts for boundary points and extracts their coordinates before returning again to B

is not feasible in the OR as the bone is buried in its anatomical position inside the patient. In this cases, an external device serving as a reference could be attached to the patient.

To calculate the translational errors in X and Z directions, we used the same process described in Section 3.5.3, *i.e.* extracting the coordinates of centers of the Steinman pins holes left in guide using image processing and boundary tracing.

This process let us to calculate the spatial orientation of the cutting guide after proper positioning. It is a non-invasive procedure as we simply take still photos of the patient and the bone. The results of both the image processing and the boundary tracing algorithms must be analyzed considering the results from Equation (3.6) and only after precise location of tumor tissue during preoperative plan is obtained. If the image processing algorithm estimates that cutting guide is misplaced by an amount beyond limits established by Equation (3.6), the guide must be repositioned and orientation must be extracted again.

Our next task will be to estimate the accuracy of this procedure by a series of experiments presented in next section. The main criteria will be to compare the results obtained using boundary tracing with the results obtained by reverse-engineered CT scan images as described in Section 3.5.

4.3 Experimental Study

In this section, we present the image process of digital images to quantify the accuracy of the positioning of cutting guides in the OR.

The image processing and boundary tracing procedures presented in Section 4.2 need to be validated. We designed a series of experiments with an objective to calculate the spatial orientation of the cutting guide after surgeon's positioning using the boundary tracing method, and compare the results with the ones computed by processing CT scan images acquired from similar experiments, as presented in Section 3.5.

By the nature of the data acquisition system, it is tempting to think that CT scans offer more reliable results because a 3D image gives a broader spectrum of the specimen and a

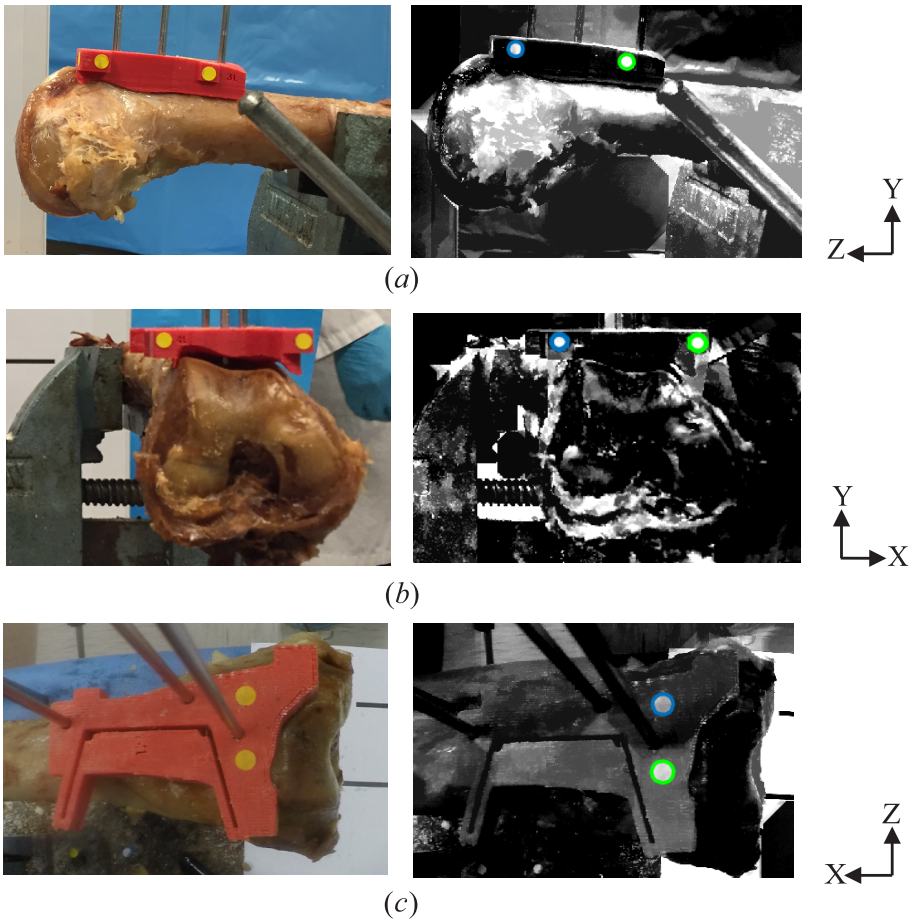

Figure 4.5: Marker detection in cutting guides using image processing. Original images are shown in the left column, and the gray-scale images in the right column. The colour contours shows proper marker detection in (a) lateral view in plane YZ, (b) front view in plane YX, and (c) top view in plane XZ.

3D-CAD environment offers more details. However, the reverse-engineering process is exhaustive, time-consuming and tedious. On average, it takes 4 hours to process every CT-scan image from DICOM file reconstruction to STL processing and final CAD-environment exporting. Therefore, this process cannot be applied in real-time surgical process to correct the position of the guide intraoperatively.

However, the boundary tracing procedure described in Section 4.2 takes only seconds using a typical computer for processing. By using the proposed procedure, the doctor will only need to take a few photos and wait for the computer (or smartphone) application to do the analysis and reposition the guides by adjusting for the errors in positioning.

4.3.1 Experimental setup

The 3D images were obtained from 12 pairs of cadaveric femurs using a CT Scanner. Cutting guides were designed for each of the 24 bones based on digital representation. Each guide was designed considering a resection cutting path using the same criteria described in Section 2.4.1, and based on a virtual tumor (10x10x25 *mm* ellipsoid) positioned on the distal medial metaphase of the bone.

Three types of cutting guides were inspected, the same that were used in the experiments described in Section 3.5 in order to be consistent and be able to compare results between the two experiments. The guides were equally distributed among the 24 specimens: the standard guide is used in 8 bones, guides with gusset in 8 bones, and guides with distributed spikes in the remaining 8 bones. Experiments are divided into two sessions to minimize the human factor of experience.

4.3.2 Experimental procedure

A senior orthopedic surgical resident was asked to prepare the specimens by removing only necessary soft tissue to reveal the area enclosed by the distal line of capsular reflection without touching the patellar surface (Figure 4.6), in order to simulate OR con-

ditions. The guides were 3D-printed which included the design of the superior ridge of the medial femoral articular surface of the bone in their distal edges. In addition, the undersurface of the guides match the anterior surface of the femur. The surgeon was introduced to these features and was asked to used them to position each guide in place after stabilizing the bone using a tabletop vise.

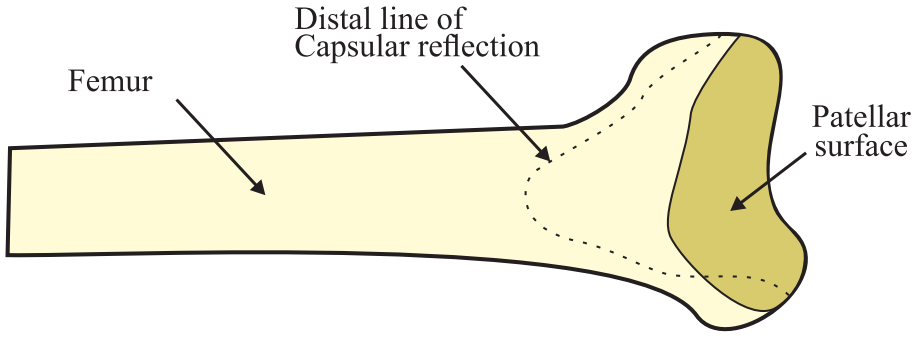

Figure 4.6: An illustration showing the distal line of capsular reflection in the femur where cutting guide is placed for resection

Once the surgeon felt comfortable with the position of the guide, it was held in place by three bicortical 5 *mm* Steinmann pins. Before performing the resection, three pictures were taken to asses how well the surgeon located the device. The setup of the experiment is presented in Figure 4.7. Typical high-end smartphones (Apple iPhone 6) were used to take the pictures in the XY plane (roll) and the YZ plane (pitch). For the XZ plane a GoPro Hero 4 camera was used in order to test other types of capturing device. The smartphones and camera were held using corresponding tripods and the positions of those tripods were marked in order to consistently locate the cameras in the same spot for each bone.

As presented in Figure 4.8, circular color coding labels of 6 mm diameter were placed on each face of the cutting guide, matching with the 3D-printed references included in guide's design. The references were designed in order to depict an ideal position of the guide without rotation and translation. Colors of labels were chosen based on guide's tone to produce the best contrast, which is desired in the image processing and boundary tracing algorithm. Different color combinations of guide and coding labels were tested.

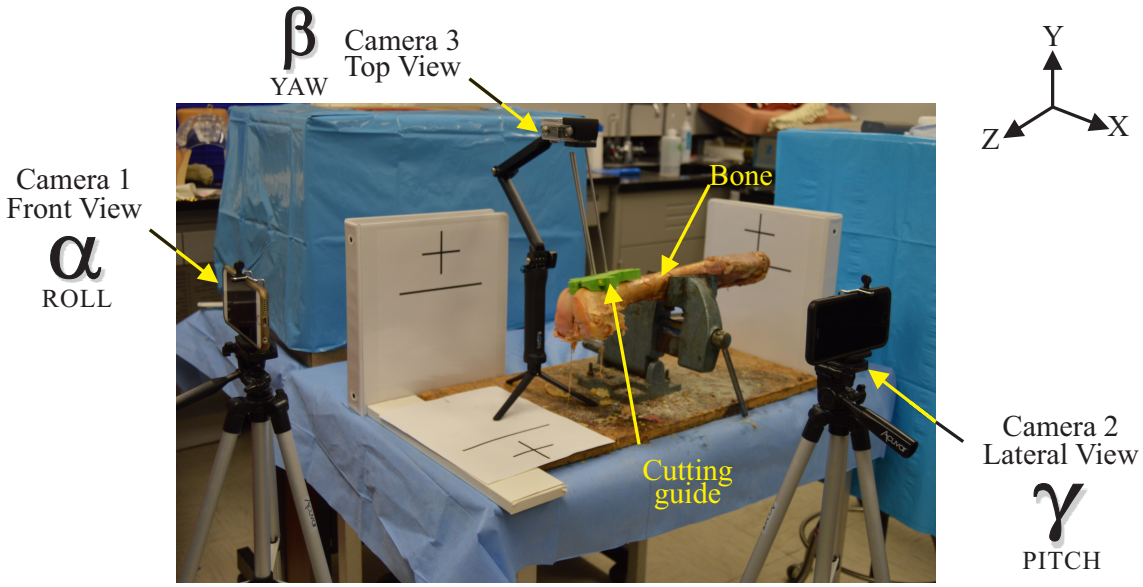

Figure 4.7: Experimental setup. Three cameras were positioned to capture each plane of the guide after positioning: front, lateral and top. Pictures were processed using boundary tracing technique to calculate spatial orientation of the guide.

As stated in Section 4.2.2, a reference was drawn on the specimen by placing the bone in its natural position on top of a flat table and a line parallel to the table was traced in the patelar surface of the femur, as shown in Figure 4.3(a).

Also, to confirm our results, another external reference was located for every camera angle. This will allow us to calculate the corresponding rotation and translation by measuring them for both, bone and guide, with respect to the external reference. The difference between these two will be the relative position of the guide with respect to bone.

Finally, after pictures were taken and processed, the surgeon may need to adjust the cutting guides based on the outcomes of image processing, before performing the outlined resections for each bone.

4.4 Experimental results

The procedures described in Sections 4.2 and 4.3 were repeated for each of the 24 bones. Image processing and boundary tracing algorithm are employed to calculate the spatial orientation of the cutting guide with respect to the bone after being positioned by the surgeon. Matlab software was used to process all pictures, and average values were taken for each angle (α, β, and γ).

Table 4.1 shows the average results of the rotation in all planes for the three types of guides used in the experiment. It is found that the pitch rotational errors are greater than the errors of roll and yaw. On average, the standard guide reported less rotation than other.

The results of translational errors are presented in Table 4.2. On average, the gusset guides have smaller translational errors, which is expected as the added feature restricts the movement of the guides. The translation along the Y direction is considered zero for the case of smooth surface and is estimated at 2 *mm* for the tissue-covered case, according to the consideration explained in Section 3.5.4.

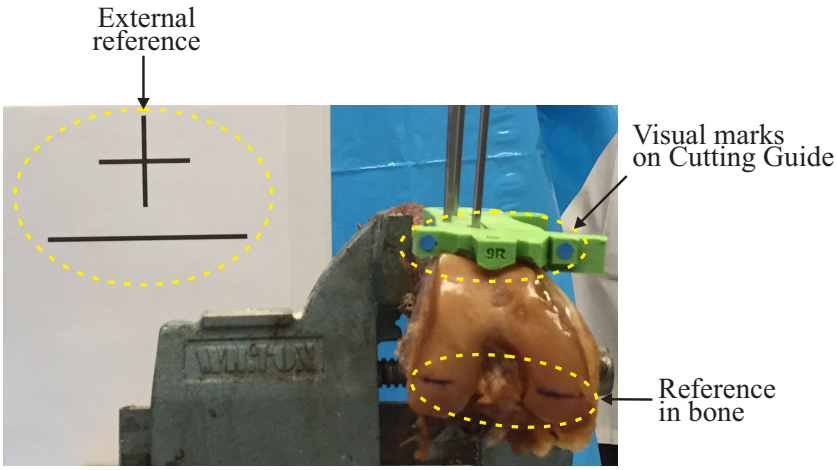

(*a*)

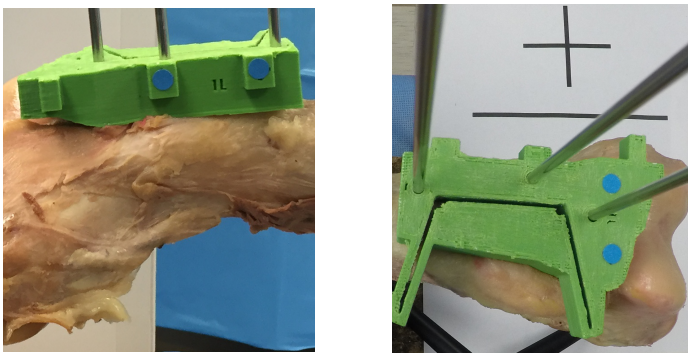

(*b*)

Figure 4.8: Coding labels and references used in image processing experiment (*a*) the front view of femur in placed showing the external reference, guide and bone references, and (*b*) coding labels located on top of 3D-printed references on guide for lateral (left) and top (right) view.

	Roll α		Yaw β		Pitch γ	
	Mean	SD	Mean	SD	Mean	SD
Standard	1.06	3.35	0.35	1.54	2.66	2.29
Gusset	1.35	1.57	0.66	2.13	2.96	2.77
Point	0.0038	3.28	3.38	1.95	2.10	2.27
Average	0.80		1.46		2.57	

Table 4.1: The mean and standard deviation (SD) of α, β and γ of the cutting guide after positioning, calculated using the image processing and boundary tracing algorithm; all values are in degrees

	X		*Z*	
	Mean	SD	Mean	SD
Standard	-1.26	2.45	-2.14	0.96
Gusset	0.72	1.89	-0.59	2.78
Point	1.27	0.87	-0.44	1.77
Average	0.25		-1.06	

Table 4.2: The mean and standard deviation (SD) of the translational errors of cutting guides after positioning, calculated with the image processing and boundary tracing algorithm; All values are in *mm*

4.5 Comparison of results and discussions

In this section, we will compare the results in Section 4.4 with these in Chapter 3, as well as discussions.

For a fair comparison, the data of the 'point and gusset' guide was removed from Tables 3.2 and 3.5. Subsequently, average values were recalculated. We did not included this type of guide in the image processing experiments as we demonstrated in the experiment described in Section 3.5, that it did not contribute much to decrease the positioning errors as compared to other types of guides.

Table 4.3 presents the average rotational errors of all types of guides for both CT-Scan and image processing. Differences of the rotational errors are around and less than 0.1 degrees in all cases. Data was subject to a linear regression and R^2 values are shown.

Table 4.4 presents the results for comparison of the translational errors. The translational errors along the Y direction is not considered as it is estimated. For the translational errors in the X direction, the difference between both cases is barely 0.03 *mm*; while the errors in the Z axis is 0.06 *mm*. Data was also subject to a linear regression and R^2 values are shown.

	CT-Scan	Image Processing	Difference	R^2
Roll	0.9	0.80	0.10	0.85
Yaw	1.54	1.46	0.08	0.83
Pitch	2.65	2.57	0.08	0.83

Table 4.3: Comparing values of rotational errors obtained by processing CT-Scan medical images versus still pictures; values are in degrees

	CT-Scans	Image Processing	Difference	R^2
X	0.28	0.25	0.03	0.86
Z	1.12	1.06	0.06	0.79

Table 4.4: Comparing values for translational errors obtained by processing CT-Scan medical images versus still pictures; values are in *mm*

4.5.1 Discussion

According to the presented results it is fair to accept that image processing and boundary tracing techniques offer a reliable way to calculate the spatial orientation of the guide in the OR during surgery.

In the case of rotations, the differences between CT scans and Image processing are 0.10° for the roll direction and 0.08° for the yaw and pitch direction. Paired t-tests yielded these differences were not statistically significant. In the analysis for translations the differences were 0.03 *mm* for translation along X axis and 0.06 *mm* for translation along the Y axis, again, after proper statistical analysis it was found that these differences are not significant.

These results indicate that the use of boundary tracing and image processing techniques is as reliable as the reverse engineering process using CT scans presented in Chapter 2 and used in Chapters 2 and 3.

4.6 Summary

In this chapter, we have presented a technique to correct positioning of the cutting guide in real time, prior to the resection. This is a process that takes into consideration only on the ability of the surgeon to match the distal edge of the guide with the superior ridge of the medial femoral articular surface of the bone, but also on the amount of soft tissue left in the bone before the cutting procedure.

In Chapter 3 and the experiments described in Section 3.5, we have relied on the high resolution of the medical images obtained using a CT scanner and the reverse engineering of such images using specialized CAD processing software. Although these results are very reliable, they require longer processing time and costs, and do not provide a real-time solution in the OR. While the technique presented in Chapter 3 with CT images provides a very precise design of cuttin guides and preopertive planning, it involves multiple steps in the process which are time consuming to computer, and costs more with computer tomograpy.

One such solutions of real-time positioning of the guide with respect to the patient is provided by the O-arm (Medtronic, USA), but with prohibitive cost.

Our objective is to provide surgeons with a tool that enhances their experience in the OR. The use of image processing techniques to extract information from still photos is fast and easy. The technique of boundary tracing is able to extract the position of the circular markers placed in the cutting guide. The results of experiments presented in Section 4.4 indicate that this technique has nearly the same accuracy as the process using CT scan images. Not only that, it is fast and affordable.

This analysis paves a pathway to use still pictures for calculating the spatial configuration of the cutting guide after positioning and correcting it, according to the limits established in Equation (3.6).

Chapter 5

Bone Reconstruction Using Biomimetic Implants

5.1 Introduction and justification

Current 3D printing bone technologies can create either hard inert bone structures (based on primary scaffolds) that are structurally compatible but functionally inert, or fragile soft structures that have osteoconductive properties but are extremely weak in structure. However, the best bone scaffolds should be able to withstand heavy loads and, at the same time, allow for osteoconductivity [33]. Several studies tested the biomimicry and structural strength of different printing materials, however, all attempts were unsuccessful in finding the perfect material [34].

It is our objective to create artificial bone that is both biomimetic and biocompatible using structural designs obtained from μCT of bones to create bone scaffolds and strengthen the scaffolds by seeding them with bone producing cells.

Low mechanical strength is a major challenge in porous scaffolds, and is primarily controlled by pore volume. This is also true for one-dimensional (1D) and 3D printed scaffolds and limits their use to only non-load bearing and low-load bearing applications. A majority of materials currently used in creating artificial bones, though biocompatible, are inert. Few materials like mineralized collagen and hydroxyapatite allow osteogenic activity and are capable of guiding bone regeneration. However, these materials are very difficult to use in fabricating bony scaffolds and the mechanical strength of this artificial

bone is too low to provide effective support at human load-bearing sites. Hence it can only be used for the repair at non-load-bearing sites, such as bone defect filling and bone graft augmentation. We present a technique to create a high tensile artificial bone by using ABS. An overview of the steps to accomplished these objectives is presented in Figure 5.1.

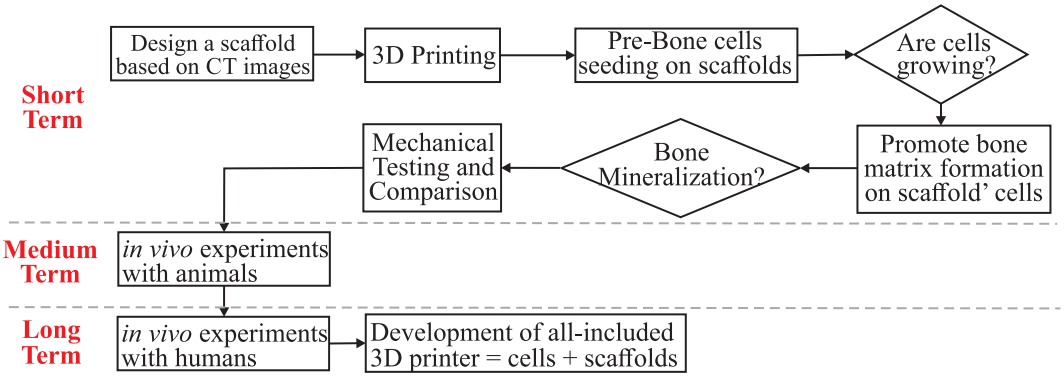

Figure 5.1: Flowchart for Biomimetic Implants Project

5.2 Designing process of 3D-printed ABS scaffolds using bone's trabecular pattern

A very similar process to the one described in Section 2.2 is presented to design 3D-printed ABS scaffolds. The process start with a μCT of a L5 rat vertebrae. After importing the CT Scan file and converting it to STL extension, editing using Geomagic is required to reduce noise. Later, Solidworks is used for feature-extraction to replicate the trabeculae pattern over scaffold's surface. A simplified schematics of these steps is presented in Figure 5.2. Also, the editing process using CAD software is presented in sequential steps from DICOM image to final CAD file in Solidworks in Figure 5.3. After the design is ready, the scaffolds will be 3D-printed using fused deposition modeling (FDM) process in a CubePro (3D Systems, USA) 3D printer.

We use the trabeculae feature of the bone, as a unique feature compared to other approaches [35], for two main reasons: to create a more conductive environment for bone

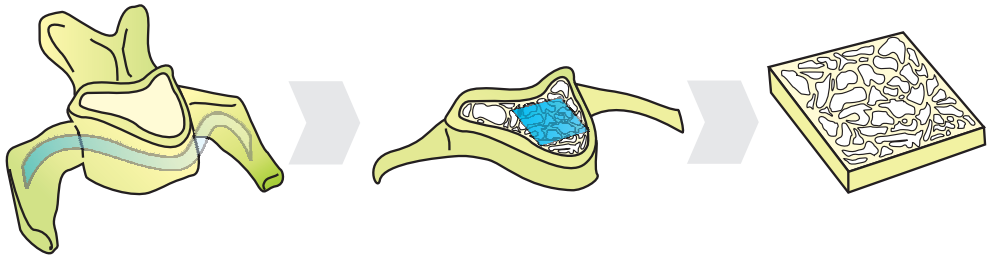

(*a*) (*b*) (*c*)

Figure 5.2: Designing proces of Trabecular Scaffolds: (*a*) CT images of rat L5 vertebra, (*b*) sliced segment of vertebra to expose trabecular pattern, and (*c*) scaffold with trabecular pattern ready for seeding

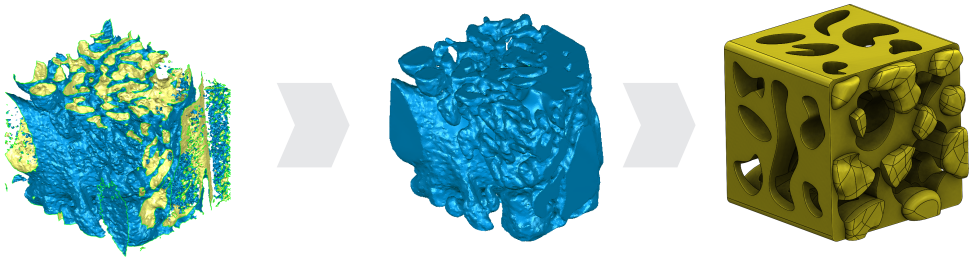

(*a*) (*b*) (*c*)

Figure 5.3: CAD editing of trabecular scaffolds: (*a*) Raw CT scan image of rat vertebrae, (*b*) editions in Geomagic for noise reduction, and (*c*) trabecular scaffold finished using Solidworks

matrix formation and to mimic the structural support that trabeculae pattern gives to bone. For instance, cancellous bone is the primary host of cellular regeneration, its built-in porosity leads to a broader surface area which induce cells to inhabit in that surface more easily, hence, a better habitat for bone formation. It is our interest to validate these ideas with the experimental study. In order to successfully extract the trabecular pattern of the bone so that it matches our 3D printer resolution, several revisions were needed. A compilation of the most relevant versions is shown in Figure 5.4.

5.3 Cellular growth on 3D-printed ABS scaffolds: preliminary studies

Once the scaffolds are designed, evaluation of their cell integration response is required. To do so, a detailed protocol is followed after proper sterilization of the scaffolds. Such protocol will be described in following sections. Later, in order to alter, and enhance, the mechanical properties of the scaffolds, we induced mineralization off the scaffolds, also with a specific procedure.

We used MC3T3 cells (ATCC-CRL2593), a commonly used cell line in experiments related to bone simulation. These type of cells are derived from *Mus Musculus*, typically call as 'house mouse', bone. They are osteoblast (See Section 1.5) precursors or 'pre-osteoblasts'. They are commonly used to study *in vitro* osteoblast differentiation since their behavior is similar to primary bone osteoblasts.

Also, our lab has been investigating a bioactive peptide called Calcitonin Receptor Fragment Peptide (CRFP). CRFP was found to be bioactive as well as osteogenic by its ability to enhance bone matrix production by osteoblasts and by its ability to transform human stem cells into bone producing cells. CRFP was also found to be skeletally bioactive *in vivo* by strengthening bones in osteoporotic animals [36]. It is our interest to evaluate CRFP effect cell seeded in our scaffolds.

Figure 5.4: Evolution of scaffold design: most relevant versions including final 3D-printed part

5.3.1 Protocol for cell-seeding scaffolds

The following protocol is followed in detail to evaluate cell growth response in ABS trabecular scaffolds. Figure 5.5 also shows pictures of the procedure.

(1) The printed scaffolds are washed for 24 hours with deionized water, sterilized and stored in ethanol. Before experimentation scaffolds were air-dried in a cell culture hood

(2) Each scaffold is attached to a corresponding well in a cell culture plate using sterilized vacuum grease with a cotton swab. [1]

(3) 1.5 ml of CRFP (concentration of 15mM in 100μl) is deposited over fixed scaffolds and let it set for 1 hour.

(4) Media for cell culture is prepared with the following ingredients:

- Minimum essential medium (α-MEM): amino acids, salts, glucose, vitamins.
- 10% Fetal bovine serum (FBS): supplement for *in vitro* cell culture. It helps cells to survive, grow and divide.
- 1% Pen strep (penicillin mixture): used to keep cultures contamination free.

(5) MC3T3 cells were maintained in the supplemented α-MEM.

(6) Cells were plated at 40,000 cells/35-*mm* dish and maintained in α-MEM with 10% FBS

(7) An incubation period at 37 C is followed for 7 days. MEM is changed every 3 days.

[1] Scaffolds needed to be attached on wells, otherwise they will float due to ABS density. A floating scaffold won't serve as culture environment since cells tend to solid immobile base.

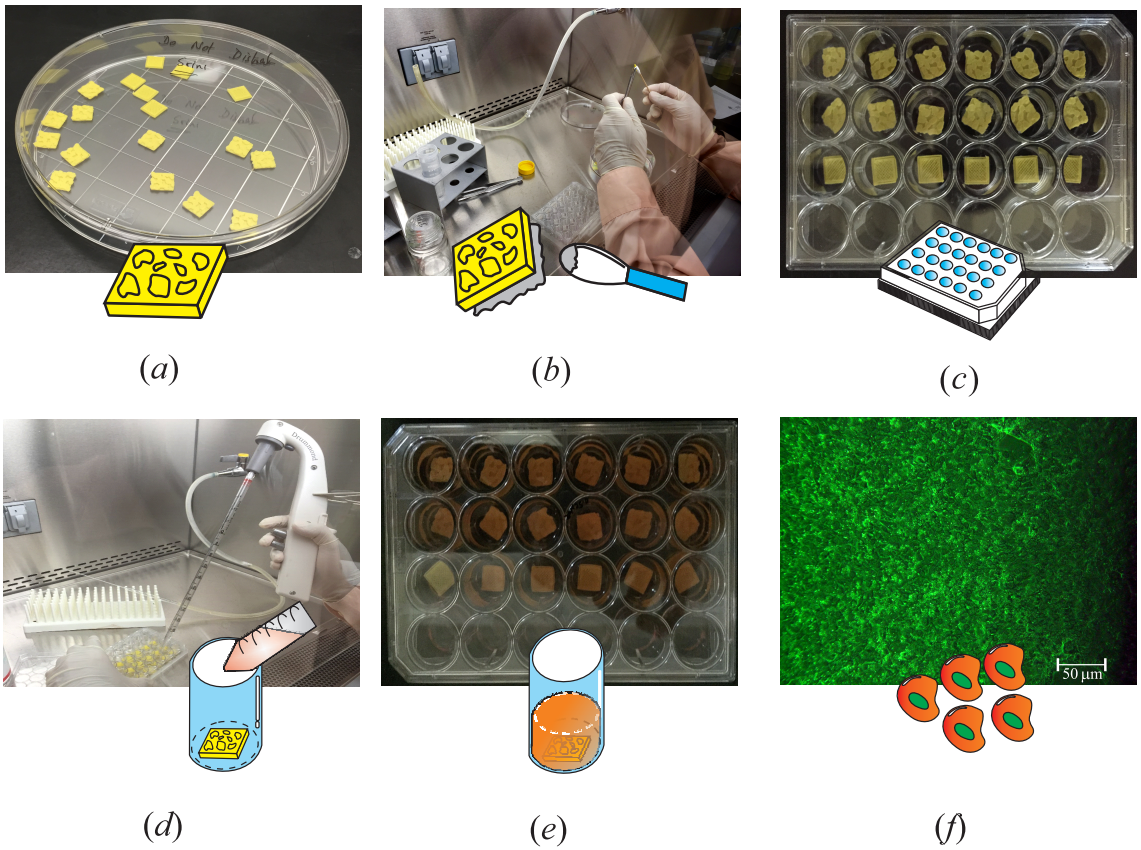

Figure 5.5: Cell seeding protocol: (*a*) sterilized scaffolds ready for seeding, (*b*) scaffolds are attached to plate using grease, (*c*) scaffolds in culture plate, (*d*) Dispensing media for cell culture over scaffolds using pipet, (*e*) scaffolds submerge in media, and (*f*) microscope view of cells growing on scaffolds.

5.4 Depositioning of 3D-printed scaffolds with cellular bone matrix

Osteogenesis (see Section 1.5) was assessed in treated scaffolds after incubation time. The main goal is to promote cellular bone matrix propagation over inner and outer surfaces of scaffolds. This will constitute the biomimetic characteristic of these 'frames' as they are hosting real cellular matrix, in addition to trabecular pattern already printed. We hypothesize that by allowing the cultured cells to mineralize the ABS scaffolds, the mechanical strength, particularly under compression stress, will be enhanced. Also, the biological performance of these scaffolds will be different compared to implants used nowadays as they will recreate a familiar environment where host cells will more likely grow and, therefore, allow for resorption and vascularization of patient's bone. All these hypothesis will be proved with further-described experiments.

A very common protocol for promoting bone formation by osteoblasts includes the use of osteogenic reagents. The reagents used in our series of experiments are:

- **β-Glycerol phosphate (G6P):** organic phosphates aids osteogenesis by starting mineralization in cell cultures [37]. Concentration is 5 μM
- **Ascorbic Acid:** initiates the formation of extracellular matrix and synthesis of several osteoblast-related proteins [38]. Concentration is 50 $\mu g/ml$
- **Calcitonin Receptor Fragment Peptide (CRFP):** a novel peptide sequence that has skeletally anabolic proporties [36].[2] . Concentration is 15 μM

All these reagents are utilized according to the protocol describe in next section.

[2] We are using CRFP as both: a precoat and an osteogenic reagent

5.4.1 Protocol for inducing cellular bone-matrix formation on 3D-printed scaffolds

The following protocol is a continuation of the one described in Section 5.3.1, specifically, after 7 days of cell culture:

(1) Media for cell culture is removed from each well

(2) On confluence, designated day 0, cells were then exposed to osteogenic medium containing α-MEM supplemented with 5% FBS. Reagents were added to each well according to schematics in Figure 5.6

(3) Confluent cells treated with osteogenic inducers were cultured for 21 days. Media is changed accordingly every 5 days.

5.5 Evidence of succesfull seeding and osteogenesis: staining and imaging

Staining and imaging techniques were used in order to report evidence of succesful seeding over scaffolds, and monitoring cell proliferation, growth and bone matrix production on scaffold's surface. After treatment with osteogenic agents, cells need to go through **fixation** process. The main objective of fixation is to stop cells decomposition and literally 'freeze' them. This way, a snapshot of the total culture environment could be taken, including cellular proteins and structures. In our case, scaffolds were fixed in 4% formaldehyde.

Two types of stains where used to collect evidence of both: cellular growth and osteogenesis. A double staining of Alexa568-Phalloidin, a high-affinity F-actin (see Section 1.5) probe, and DAPI (also in Section 1.5) for nuclear staining was used to monitor cell growth and proliferation. Alizarin Red stain was used to stain calcium deposits, showing bone matrix deposits.

Scaffolds were imaged with confocal microscopy (Zeiss LSM-510) and with a scanning electron microscope (ISI-SX30 SEM). Figure 5.7(a) shows a 3D reconstructed confo-

Figure 5.6: Treatment of MC3T3 cells with osteogenic inducers

cal z-sections images of cells grown on scaffolds and Figure 5.7(*b*) shows an SEM image of cells on the scaffold.

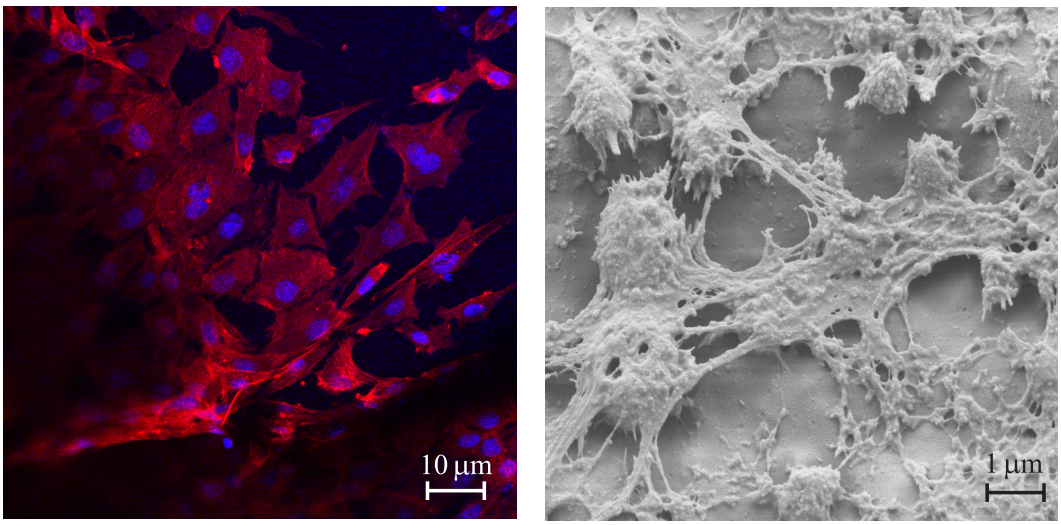

(*a*) (*b*)

Figure 5.7: Microscopy results over treated scaffolds: (*a*) Laser-scanning confocal images of osteoblasts growing on 3D-printed scaffolds. Cells stained with Alexa Phalloidin and DAPI, and (*b*) Scanning electron microscope image of cells growing on 3D-printed scaffolds

Figure 5.8 shows scaffolds under magnifying microscope. Incubating the seeded scaffolds under osteogenic conditions showed osteoblasts promoting matrix formation and mineralization as evidence by abundant alizarin red staining.

5.6 Evaluation of CRFP effect on bone formation regulators

Calcitonin receptor is a G protein-coupled receptor which binds the peptide hormone calcitonin, and is involved in maintenance of calcium homeostasis, particularly with respect to bone formation and metabolism. CRFP used in this project was identified by specially written algorithm, and this peptide sequence was found to be in the C-terminal intracellular domain of the calcitonin receptor. Interestingly, the same peptide sequence was found to be the G-protein interaction site, as identified by extensive mutagenesis work by other researchers [39]. However, no studies were reported showing that small peptides like CRFP

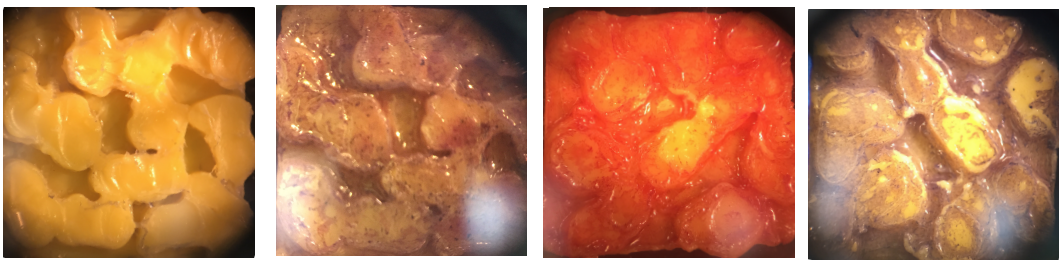

(*a*) (*b*) (*c*) (*d*)

Figure 5.8: Mineralization results using Alizarin red stain: (*a*) Control (no reagents), (*b*) G6P + Ascorbic Acid, (*c*) CRFP, and (*d*) G6P + Ascorbic Acid + CRFP

derived from the proteolytic cleavage of a mature protein like calcitonin receptor, have the ability to activate biological processes, particularly a complex process like bone matrix formation.

Bone remodeling is the dynamic metabolic process of the body, which regulates calcium homeostasis through osteoclast-mediated bone resorption and osteoblast-mediated bone formation [40]. Bone resorption by osteoclasts releases stored calcium into systemic circulation while bone formation by osteoblasts fixes circulating calcium in its mineral form [41].Any disruptions in this process can result in various bone pathologies such as osteoporosis, osteopenia, osteomalacia, etc.

Osteoporosis is a type of bone pathology in which bone mineral density is reduced, microarchitecture of the bone is affected, and various amounts of non-collagenous proteins in the bone are altered [42]. It is most often associated with a progressive deterioration and slight thinning of the bone, commonly referred to as osteopenia. These conditions can eventually lead to fractures of the hip, wrist, and vertebra [43]. One potential approach to reduce the magnitude of osteoporosis is to increase osteoblast activity while simultaneously blocking osteoclast activity [39].

Several signaling molecules like bone morphogenic peptide-7, osteocalcin and osteopontin were found to regulate bone matrix production. BMP-7, also known as Osteogenic protein-1 (OP-1), is one of 15 currently known BMPs, which are structurally and functionally related and which are part of the transforming growth factor β (TGF-β) superfamily

of growth factors. BMP-7 was originally identified as a regulator of cartilage and bone formation. Osteocalcin is synthesized by osteoblasts and is one of the most abundant non-collagenous proteins found in bone. It first appears in embryonic bone when mineralization begins and integrates into bone by binding hydroxyapatite in a calcium dependent manner. Osteopontin (OPN) is intimately involved in the regulation of both physiological and pathological mineralization. In normal bone tissue, OPN is expressed by both osteoclasts and osteoblasts which are the cells responsible for bone remodelling. Immunoblotting technique was used to test whether CRFP has any effect on the expression of signaling molecules like BMP-7, osteocalcin and osteopontin.

5.6.1 Preparing cell extracts for immunoblot studies

Cells were grown in T-25 flasks and were treated with CRFP. Two concentrations were selected for treatment based on the microscopy results 13.8 μM and 15 μM. After the cells reached 80% confluency, osteogenic agents were added and cultured for 7 days. The cells were treated with 1 ml of Sigma lytic buffer with protease inhibitor cocktail (to prevent protein degradation) and the whole cell extract was collected into 1.5 *ml* eppendorf tubes. The amount of protein in each sample was measured by BioRad protein assay by taking 5 μl of sample and adding 200 μl of BIORAD Reagent in a volume of 1 *ml*. The color developed was monitored at 505 *nm*. The protein values were extrapolated to a standard curve made with bovine serum albumin (BSA). The final plot is presented in Figure 5.9.

5.6.2 Immunoblotting

The proteins were resolved with 12% Sodium Dodecyl Sulfate Poly Acrylamide Gel Electrophoresis (SDS-PAGE). A standardized protocol was used to pour and run the gels [44]. After loading the gel with equal amounts of protein samples obtained from extracts of cells treated with CRFP, electrophoresis was performed for 1.5 *hr* at 90 volts using a BIORAD Mini-Protean II PAGE system. Resolved proteins were electroblotted

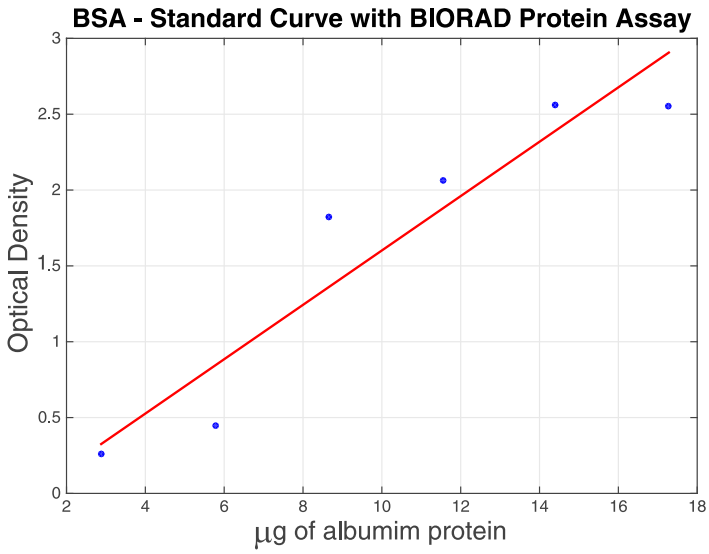

Figure 5.9: Bovine serum albumim standard curve with BIORAD protein assay

to Immobilon PVDF membrane (Millipore) using Transblot Semi Dry Transfer apparatus (BioRad) at 17 V for 1 hr with transfer buffer consisting of 25 mM Tris-base, 192 mM glycine and 20% methanol. After transfer, the membrane was blocked with non-fat milk (5%) suspended in 10 mM Tris-HCl, pH 7.5, 150 mM NaCl, (TBS) for 1 hour, and then incubated with appropriate primary antibodies (BMP-7, osteocalcin or osteopontin) in TBS containing 1% albumin at room temperature for 1 hour. Membranes were washed with TBS containing 0.2% Tween-20 and then incubated with horseradish peroxidase conjugated 2nd antibody in a solution of 1% albumin in TBS for 45 min. Results are presented in Figure 5.10 suggesting that CRFP increases in combination with the expression of BMP-7, osteopontin and osteocalcin.

5.7 Summary

Recent advances in 3D printing have enabled biocompatible materials to be applied to regenerative medicine in order to address the growing need for tissues and organs, including bone. The aging population with its concomitant increased risk of osteoporosis, osteoarthritis, bone injuries and obesity are significant contributors to orthopedic implant failure. Due to its ability to be tailored for patient specific needs, the demand for 3D printed bone will only increase in the coming years. By utilizing low-cost material, such as ABS in our study, and showing its biocompatibility and cellular response, the road to custom created bone graft substitutes is easier and more affordable.

In this chapter we have introduced a novel technique to create biomimetic and biocompatible scaffolds. They are biomimetic in the sense that we have designed them introducing the trabecular pattern of the potential implant-host. We hypothesize that trabeculae pattern increases the porosity of the scaffolds, without diminishing its mechanical resistance, easing cellular differentiation. Post mechanical evaluation of the cell seeded scaffolds is presented in Chapter 6

Results presented in Sections 5.5 and 5.5 clearly show the ability of our scaffolds to

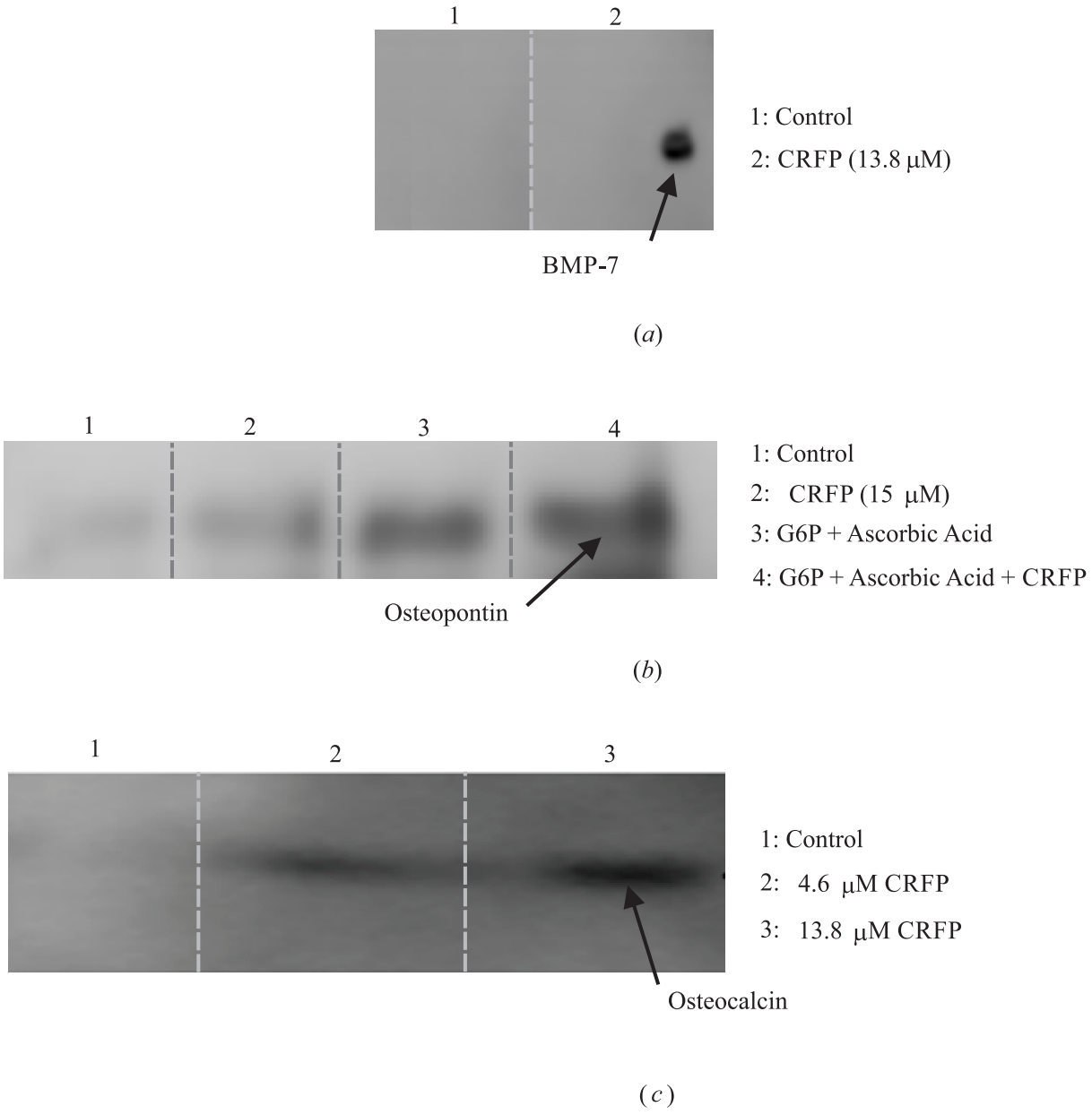

Figure 5.10: Protein expression experimental results: (*a*) BMP-7 expression, (*b*) osteopontin expression, and (*c*) osteocalcin expression in osteoblasts

host cellular reproduction and, moreover, osteogenesis. This is the fundamental aspect of biocompatibility of future implants created by this technique. CRFP has also shown to be effective in improving osteogenesis process, more so in combination with corresponding osteogenic agents.

Chapter 6

Mechanical Properties of Biomimetic Scaffolds

6.1 Introduction

A few materials like mineralized collagen [45] and hydroxyapatite [46] allow osteogenic activity and are capable of guiding bone regeneration. However, these materials are very difficult to use in fabricating bony scaffolds and the mechanical strength of this artificial bone is too low to provide effective support at load-bearing sites. After obtaining evidence of mineralization over 3D printed ABS scaffolds it is also our interest to test the mechanical properties of these hybrids (plastic + organic).

The introduction of the trabecular pattern on the scaffold's design will also be evaluated as a characteristic that would enhance the mechanical strength of the scaffolds. To do so, a comparison between a scaffold design with no trabecular pattern, also called *flat* scaffold, will be compared with the standard trabecular scaffold described in Section 5.2.

Lastly, to assess the contribution of the extra cellular matrix of which the scaffolds are now layered with, a comparison between non-treated scaffolds and treated scaffolds, *i.e.* after matrix formation, is conducted.

A simplified mechanical model, explained in the schematics of Figure 6.1, will be used to obtain the stiffness, or modulus, of the specimens. A non-treated scaffold has only the stiffness of its material, in this case ABS, and it is denoted as k_1. When the scaffolds are treated and mineralization is induced, the scaffolds now carry not only the ABS stiffness

but also the stiffness of the formed cellular matrix k_2. Any mechanical test won't disregard between these two stiffness as it will only allows us to measure the equivalent stiffness of the hybrid, *i.e.*, k_e. A straight forward mechanical model will allow us to calculate k_e as follows:

$$k_e = k_1 + k_2 \tag{6.1}$$

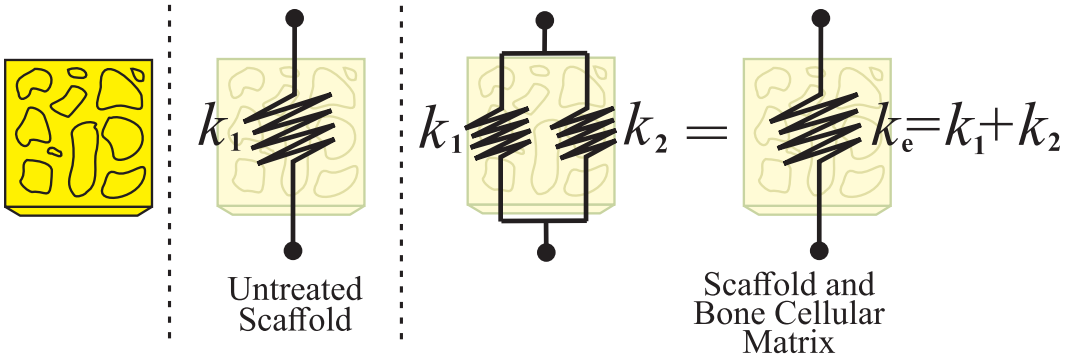

Figure 6.1: Simplified mechanical model of springs to calculate stiffness of scaffolds

6.2 Testing anisotropy of scaffolds

In this study we are also interested in testing the **anisotropy** of the scaffolds. FDM process, like the majority of 3D-printing procedures, builds the scaffolds layer by layer. This lead us to thinking about the anisotropy characteristic of our specimens. Three different directions of compression will be tested and compared according to Figure 6.2.

Also, not only the manufacturing process of the scaffolds contribute to their anisotropy, but also trabecular pattern itself adds this characteristic to the specimen as bone structure is indeed anisotropic. Bone structures perform better under compression rather than tension. However, the direction of the compression is also important. In previous statistical studies [47], the following inequality was noted, according to axis described in Figure 6.3:

$$\sigma_1 \leq \sigma_2 < \sigma_3 \tag{6.2}$$

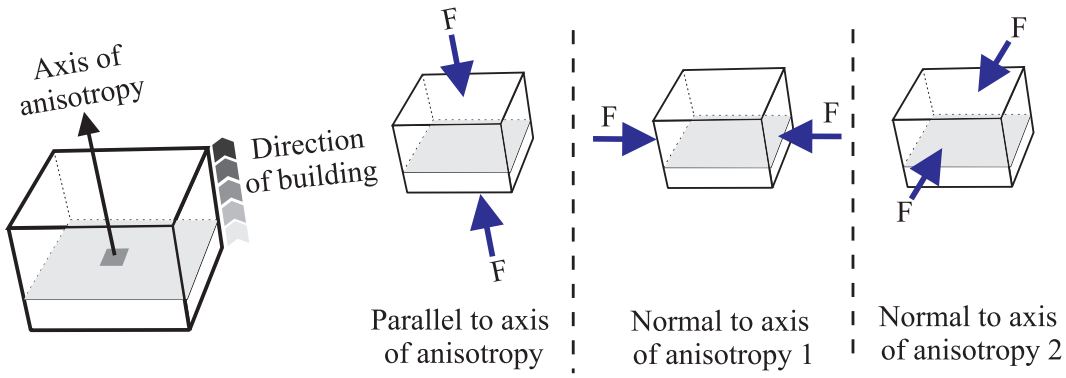

Figure 6.2: Testing anisotropy of 3D-printed scaffolds. Different axis of compression for mechanical test

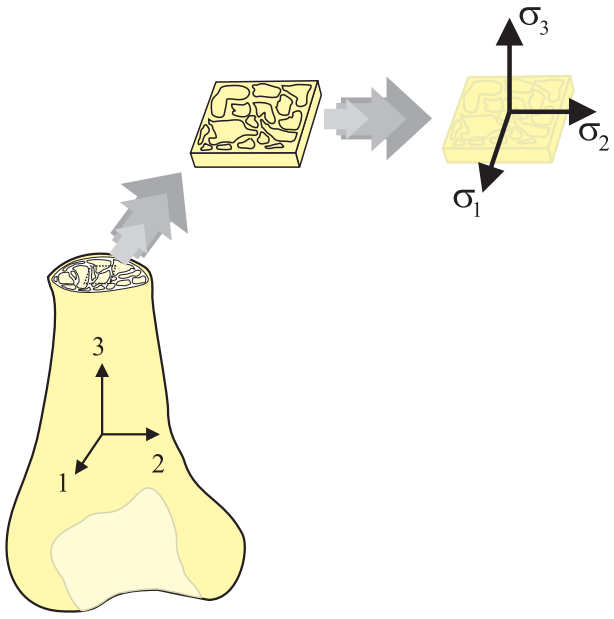

Figure 6.3: Relationship between bone and scaffold axis of compression with respect to trabecular feature

According to Equation 6.2, human bone performs better under compression but only if the axis of that compression is parallel to the longitudinal axis of the bone. In the case of Figure 6.3, that axis is labeled as 3. For our case, the trabecular feature of the bone was extracted from the natural anatomical position, just as Figure 6.3 is describing.

6.3 Compression test overview

To carry out all these comparisons in an organized and precise way, an international standard is followed. For this case, the chosen standard is ISO 604 [48], which is the standard for determination of compressive properties of plastics. We chose this standard based on the core material of our scaffolds. As stated before, two main comparison tests will be performed in the experiments using this standard:

(1) Flat scaffolds vs. trabecular scaffolds, only for non-treated specimens, and

(2) Treated vs. non-treated scaffolds.

ISO 604 has a detailed protocol including the dimension of the specimens and their number. Two different dimensions of specimens will be considered according to Table 6.1. Type A model is used to calculate the compressive modulus of scaffolds and type B model will allow us to obtain the compression strength. Also, Table 6.2 details the list of the number of specimens tested according to ISO 604 specifications[1] .

Type	Measurement	Length	Width	Thickness
A	Modulus	50 ± 2	10 ± 0.2	4 ± 0.2
B	Strength	10 ± 2	10 ± 0.2	4 ± 0.2

Table 6.1: Measures of scaffolds used in ISO 604 compression test. All values in *mm*

[1] Please refer to Figure 6.2 to check the specified directions of compressions

Type	Quantity	Configuration	Anisotropy approach
A	5	Flat	Parallel to axis
A	5	Trabecular	Parallel to axis
A	5	Flat	Normal to axis 1
A	5	Trabecular	Normal to axis 1
A	5	Flat	Normal to axis 2
A	5	Trabecular	Normal to axis 2
B	5	Flat	Parallel to axis
B	5	Trabecular	Parallel to axis
B	5	Flat	Normal to axis 1
B	5	Trabecular	Normal to axis 1
B	5	Flat	Normal to axis 2
B	5	Trabecular	Normal to axis 2

Table 6.2: Number of scpecimens per anisotropy testing approach

6.4 Test setup

MTEST Quattro (Admet, USA) compression testing system was used in accordance with IS0 604 to carry out scaffolds testings. Specimens were tested in unconstrained compression by positioning them in the center of two stainless steel plates as shown in Figure 6.4.

Surface finishing of specimens was enhanced prior to experiments using sandpaper in order to eliminate sharp edges and loose filaments formed due to the 3D printing process. All environmental conditions established by ISO 604 were accomplished, stainless steel plates parallelism was inspected and corrected before any run and every specimen was placed in the same position for any test to avoid discrepancies in results.

The speed for the tests varies depending on the outcome parameter and the dimension of the specimens. For our scaffolds, the following speeds were used as stated in ISO 604:

- 1 mm/min for modulus measurement
- 5 mm/min for strength measurement[2]

In order to present convincing evidence that, by inducing osteogenesis on cell-seeded specimens, the scaffolds will enhance their mechanical properties towards reaching similar trabecular bone properties, four rounds of experiments using seeded scaffolds were performed.

6.5 Results

For all tests, two main values were calculated: compression strength (σ_M) and compressive modulus (E_c). Definitions of these are readily presented in ISO 604 standard:

- **Compression strength (σ_M)**: maximum compressive stress sustained by the test specimen during a compressive test.

[2] This speed varies depending on the behaviour of the material under compression. Since ABS yields, ISO 604 requires to use 5 mm/min

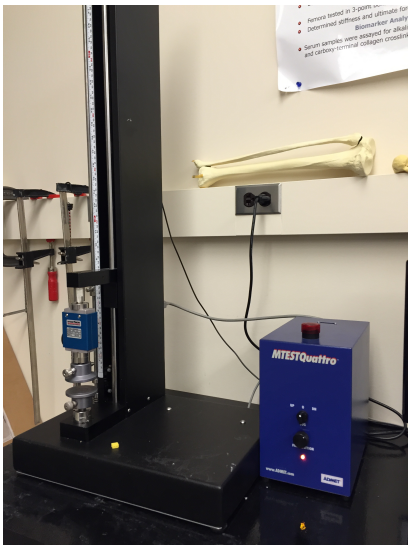

(*a*)

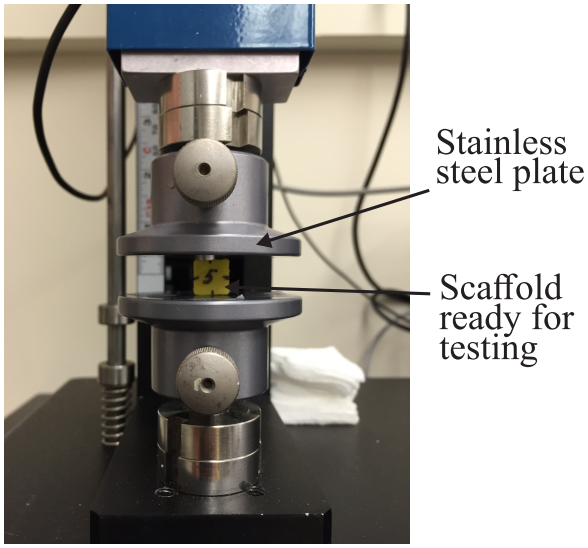

(*b*)

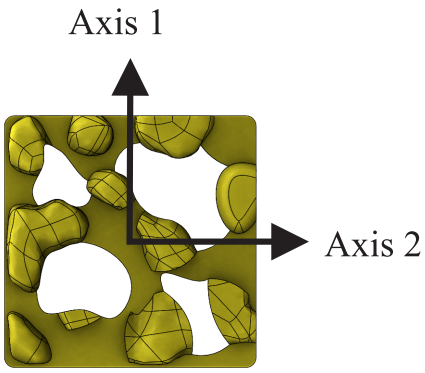

(*c*)

(*d*)

Figure 6.4: Compression test setup: (*a*) MTEST Quattro system used for compression, (*b*) scaffold in position between plates ready for compression, (*c*) schematic showing the axis of compression in the scaffold, and (*d*) comparison of ABS scaffold before and after compression test

- **Compressive modulus (E_c)**: ratio of the stress difference ($\sigma_2 - \sigma_1$) to the corresponding strain difference values (ε_2=0.0025 minus ε_1=0.005)

$$E_c = \frac{\sigma_2 - \sigma_1}{\varepsilon_2 - \varepsilon_1} \tag{6.3}$$

A first comparison between flat and trabecular scaffolds is presented in Figure 6.5. Averages values for each set of 5 tests were taken to construct stress vs. strain curves based on Equation 6.3. Values for σ_M and E_c are detailed in Table 6.3. For axis 1 and axis 2, flat scaffolds reported greater compressive strength and modulus, however, for axis 3, trabecular scaffolds exceeded flat specimens in the order of 20% for σ_M and 60% for E_c.

	Axis 1		Axis 2		Axis 3	
	Flat	Trabecular	Flat	Trabecular	Flat	Trabecular
σ_M	35.15 (4.2)	29.19 (3.8)	35.57 (2.2)	30.70 (3.4)	55.93 (3.3)	69.88 (2.1)
E_c	242.96 (12.5)	166.46 (8.5)	236.99 (11.4)	188.69 (9.7)	133.60 (9.4)	336.65 (10.1)

Table 6.3: Compression test results: Flat vs Trabecular scaffolds. Average values for σ_M and E_c for each axis of compression. Standard deviation values are shown in parenthesis. Values in MPa

Another way to compare the results is from the point of view of axis of compression, grouping only flat scaffolds or trabecular scaffolds. Figure 6.6 gathers these results and shows that for both cases, flat and trabecular, Equation 6.2 stands as the compressive strength in axis 3 is greater than axis 2 which is also greater than axis 1.

Finally, the contribution of cellular bone matrix for compression strength and modulus is also investigated and reported in Figure 6.7 presenting average results of all four rounds of performed experiments. For this case, only trabecular scaffolds were compressed in direction 2. Four cases are reported:

- **Unseeded, or untreated, scaffolds**: original specimens without any biological treatment or cell seeding.

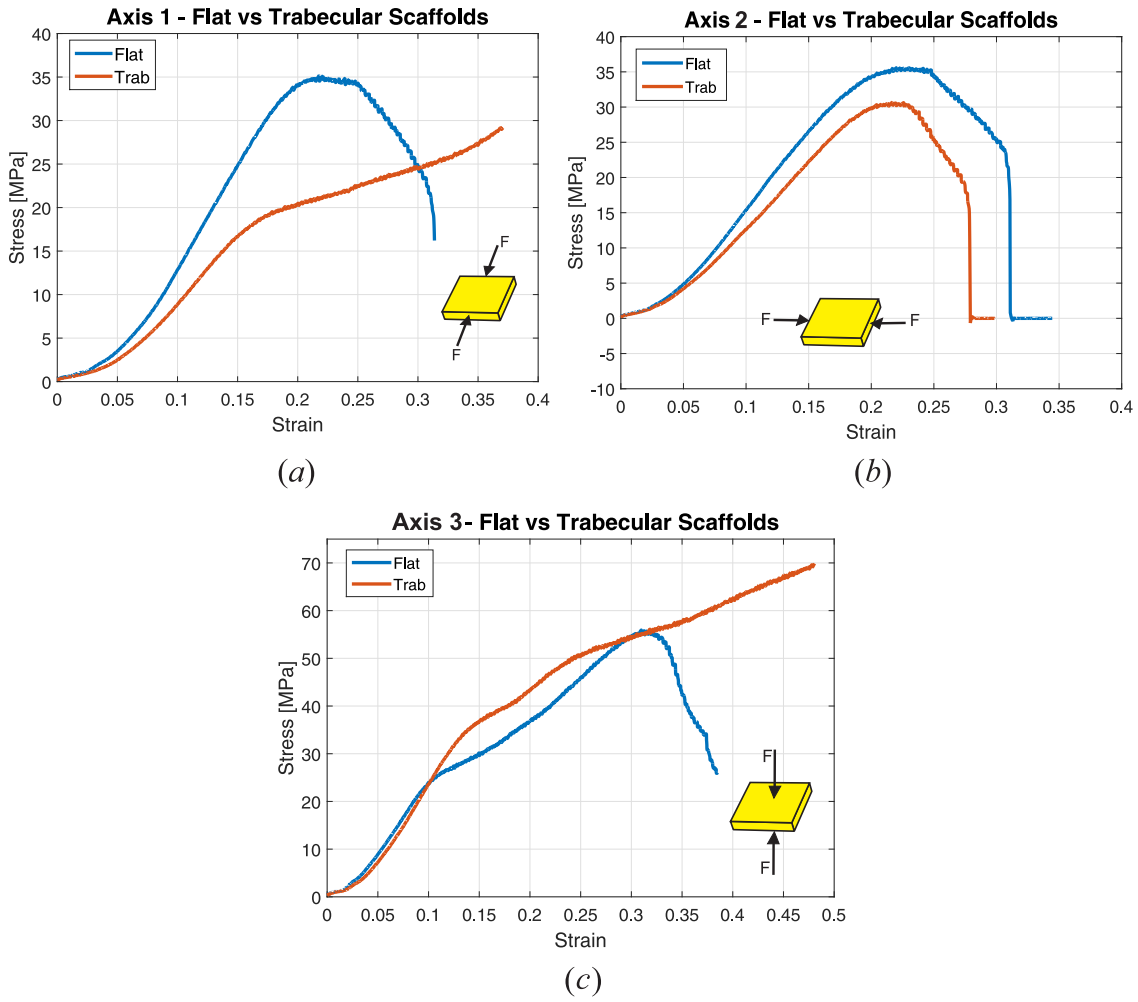

Figure 6.5: Compression test results: Flat vs. Trabecular scaffolds compressed through (*a*) axis 1, (*b*) axis 2, and (*c*) axis 3. Average values

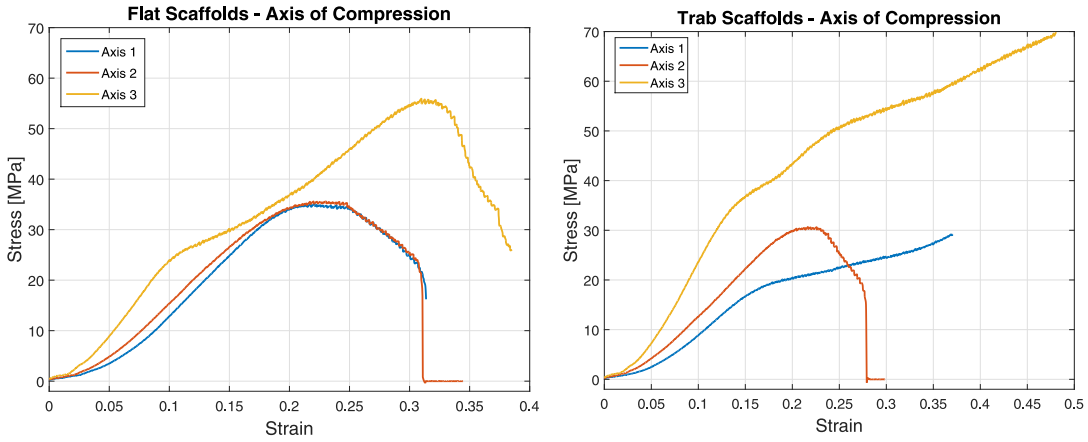

(*a*) (*b*)

Figure 6.6: Compression test results for different axis of compression for either (*a*) flat or (*b*) trabecular scaffolds. Average values

- **Control (only cells) scaffolds**: specimens with cells. Mineralization was not induced.
- **Cells + CRFP**: specimens with cells induced for mineralization by using CRFP.
- **Cells + G6P + AA**: specimens with cells induced for mineralization by using osteogenic reagents G6P and Ascorbic Acid (AA)
- **Cells + G6P + AA +CRFP**: specimens with cells induced for mineralization by using osteogenic reagents G6P, Ascorbic Acid (AA) and, also including, CRFP.

For all cases under mineralization, an increment in the compressive modulus is evident. Compressive strength also increased but not as dramatically as E_c. Table 6.4 gathers average values for each set of 5 compression tests recommended by ISO 604. Treating seeded scaffolds with CRFP significantly increased the compressive modulus compared to unseeded controls.

	Unseeded	Control (Only Cells)	Cells + CRFP	Cells + G6P + AA	Cells + G6P + AA + CRFP
σ_M	30.76 (3.1)	32.46 (3.3)	36.75 (3.7)	40.88 (4.1)	45.98 (2.9)
E_c	169.46 (12.7)	199.44 (11.4)	560.69 (10.4)	737.10 (9.7)	860.02 (13.1)

Table 6.4: Compression test results: treated vs untreated scaffolds. Standard deviation values are shown in parenthesis. Values in MPa

6.6 Discussion

Extracting trabecular pattern from microCT and including it in the scaffold's design, will allow us to enhance the strength of the scaffolds in physiologic load-bearing directions, according to the results of our compression test. Culturing these scaffolds with osteoblasts

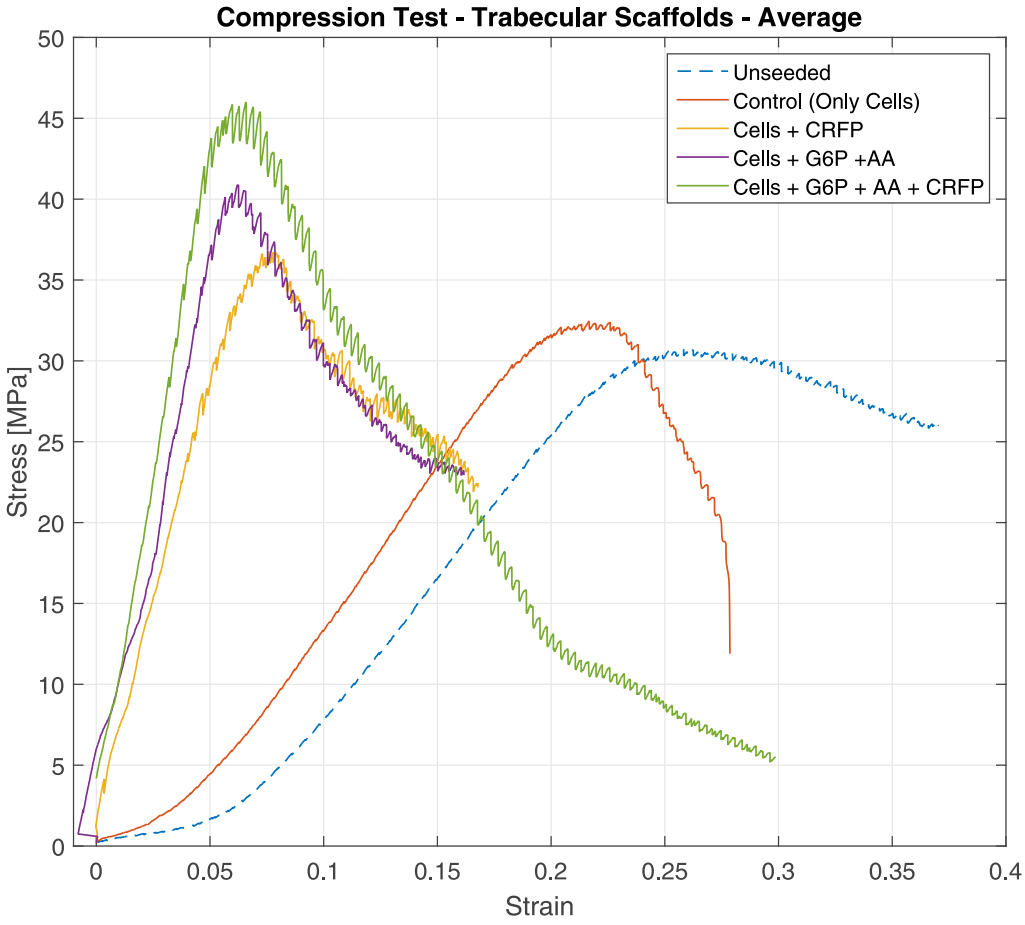

Figure 6.7: Compression test results: treated vs untreated scaffolds. Average values

leads to the production of mineralized matrix components that increase the stiffness and the strength of the scaffolds as well, which we already have shown in our series of experiments.

The type of osteogenic reagent used also showed differences. According to Table 6.4 introducing osteogenic agents and, therefore, bony cellular matrix dramatically increases the stiffness values (*i.e.* E_c), in average, for our specimens. If we only compare the values of E_c for the unseeded and treated cases (considering G6P+AA case) the increase is in the order of 400%, an appreciable difference in magnitude.

The use of CRFP requires a highlighted analysis. As we biochemically showed in Sections 5.5 and 5.5, CRFP contributed to increase in the expression of certain proteins related to bone formation. This enhancement is also shown in the results presenting in Figure 6.7. The mechanical compression strength of the treated scaffolds surpass the results for the untreated scaffolds, which report only the values of the ABS, reaching its peak in the case considering CRFP in addition to typical osteogenic agents used in the experiment. Even more important is the increase in the stiffness of the material, increasing from roughly 170 MPa up to around 860 MPa. The evidence of the potential of CRFP in bony production is presented.

6.7 Summary

During this chapter we have tested the mechanical properties of our 3D printed scaffolds under several conditions. We have proved that introduction of the trabeculae pattern of the bone increases the compression strength of these scaffolds in the direction of natural load bearing on the bone. We have also presented the differences in the mechanical strength of the scaffolds if we compressed them in different directions, showing that anisotropy must be considered in their design as well.

We have also proved that mineralization process over the scaffolds enhance their mechanical properties, such as compression strength and stiffness. This needs to be explored in the future in order to create implants with similar mechanical properties as human bone.

While the final use of these scaffolds in human patients is still a long way to go, these results open the possibilities for a new technique of producing scaffolds which, ultimately, will lay the ground work for biomimetic and biocompatible bone implants that overcome today's difficulties in the orthopedic reconstruction field.

Chapter 7

Concluding Remarks

We have proved, as described in Chapter 2, that the use of cutting guides increases the accuracy of resection as compared to manual resection. We have also showed in Chapter 3 that locating the guide in the correct place, over the bone, prior resection is a task that always introduces an error. Also, we have developed a mathematical model to quantify this error based on the location of the tumor, meaning that we are establishing limits on how much error could be introduced during guide placement. Therefore, it is crucial to apply this model during the surgery.

In Chapter 4 we have proved that image processing is a reliable way to calculate errors of positioning. After comparing the results of the experiments using image processing with those of Chapter 3 we can stated that still photos can be used in the OR to correct the position of the cutting guide.

Later, in Chapter 5, we demonstrated that ABS scaffolds admit cell seeding and growth and, finally, during Chapter 6 we confirm that trabecular pattern and bone matrix formation enhances the mechanical strength of scaffolds. Furthermore, bone matrix formation using CRFP increases up to five times the stiffness of the scaffolds.

The work presented in this document represents the effort to solve typical problems in orthopedic surgery using engineering tools.

Chapter 8

Proposed Future Work

8.1 Resection using 3D-printed cutting guides

Resection of bone sarcomas using 3D-printed cutting guides is a novel technique that increases the accuracy of resection as well as easing the procedure and reducing the surgery time span. One of the greatest challenges that our team has encountered developing this technique is to introduce it to surgeons as a way to improve their current procedures in the OR. In order to do so, we had to present evidence of the technique's reliability.

In Chapters 2 and 3 we evaluated the weakness of the cutting guide technique and provided means to solve them. The mathematical model developed to quantify the introduced error using cutting guides became a powerful tool that motivates the development of Chapter 4.

Although we have introduced a feasible technique to correct the positioning of the cutting guide intraoperatively, further work needs to be done to apply the image processing technique in a fast, reliable and affordable way. The development of smartphones applications nowadays has increased dramatically. Software is being developed for almost every aspect of our daily activities. The main reason is the relative easiness for coding and developing smartphones applications.

Current sensors and cameras included in a typical smartphone are, in most cases, of great quality and accuracy. If we analysed only photo capturing, the developing of point-

and-shoot cameras has been relegated to the increasing quality of nowadays smartphone-cameras. This is our starting point. To take advantage of this increasing technology which is, in most cases, is in our own hands.

Therefore we proposed, in future, to develop a smartphone application that every surgeon might upload to his/her device. With our image processing and boundary tracing code embedded in such application the surgeon would, potentially, take a picture of the cutting guide on top of the bone in order to assess how well did he/she positioned the guide. Not only that, as the boundary tracing code offers quantitative analysis, the application would potentially tell the surgeon in which plane he needs to correct the position and in what amount. All this, just with the information of a typical snapshot with a cell phone camera

8.2 Reconstruction using biomimetic implants

The use of Biomimetic implants has become a trending topic among the research community. Biologists, medical doctors, biomedical and mechanical engineers are all involved in obtaining the best solution to a typical problem.

We have introduced a technique that will allow us to create implants that will, potentially, allow for bone resorption and growth. The first step is to create the base of these implants, *i.e.* a scaffold. In Chapters 5 and 6 we have introduced the technique to create these scaffolds based on the patient's anatomy, specifically, the trabecular structure of the bone. Evidence was presented in two fields: biochemistry and mechanics.

Our trabecular scaffolds clearly have the capacity to promote cellular differentiation and osteogenesis and, in doing so, the mechanical properties of these scaffolds have changed dramatically as compare to untreated specimens.

These results leads to the next, natural, step: testing this technique in animal models. The objective of this aim is to compare the safety and efficacy of the 3D bone implant in a rat segmental defect model. This aim is intended to generate a comprehensive under-

standing of *in vivo* safety, osteoinductivity, and biomechanical performance of the artificial bone.

The biomechanics results for the implanted femurs will be normalized to those of their contralateral intact femurs and reported as percent of intact in order to reduce variability due to issues such as animal weight and size.

We believe that the promising clinical utility of this technology, combined with our focus on the critical path for clinical validation, makes this study an excellent opportunity to progress the development of biocompatible and biomimetic artificial bone scaffolds and improve the quality of patient care.

Bibliography

[1] F. Khan, A. Pearle, C. Ligthcap, P.J. Boland, and J.H. Healey. Haptic robot-assisted surgery improves accuracy of wide resection of bone tumors: A pilot study. *Clinical Orthopaedics and Related Research*, 471(3):851–9, 2013.

[2] D.S. Shin, P.F. Chong, E.Y. Chao, and F.H. Sim. Large tumor endoprosthesis and extracortical bone-bridging: 28 patients followed 10-20 years. *Acta Orthopaedica Scandinavica*, 71(3):305–11, 2000.

[3] H.J. Mankin, M.C. Gebhardt, L.C. Jennings, D.S. Springfield, and W.W. Tomford. Long-term results of allograft replacement in the management of bone tumors. *Clinical Orthopaedics and Related Research*, Mar(324):86–97, 1996.

[4] F. Khan, J.D. Lipman, A.D. Pearle, P.J. Boland, and J.H. Healey. Surgical technique: Computer-generated custom jigs improve accuracy of wide resection of bone tumors. *Clinical Orthopaedics and Related Research*, Jun;471(6):2007–16, 2013.

[5] S. Bose, S. Vahabzadeh, and A. Bandyopadhyay. Bone tissue engineering using 3d printing. *Materials Today*, 16(12):496–504, 2013.

[6] L. Dyrda. 10 predictions for the global orthopedic device market. *Beckers Orthopedic and Spine Review*, 2014.

[7] C. Chen, H. Li, J. Pan, Z. Yan, Z. Yao, W. Fan, and C. Guo. Biodegradable composite scaffolds of bioactive glass/chitosan/carboxymethyl cellulose for hemostatic and bone regeneration. *Biotechnology Letters*, Feb;37(2):457–65, 2015.

[8] Y. Khan, M.J. Yaszemski, A.G. Mikos, and C.T. Laurencin. Tissue engineering of bone: material and matrix considerations. *The Journal of Bone & Joint Surgery*, Feb;90 Suppl 1:36–42, 2008.

[9] K.C. Wong, S.M. Kumta, K.Y. Sze, and C.M. Wong. Use of a patient-specific cad/cam surgical jig in extremity bone tumor resection and custom prosthetic reconstruction. 17(6):284–293, 2012.

[10] O. Cartiaux, L. Paul, B.G. Francq, X. Banse, and P. Docquier. Improved accuracy with 3d planning and patient-specific instruments during simulated pelvic bone tumor surgery. 42(1):205–213, 2013.

[11] M. Kunz, J.F. Rudan, G.L. Xenoyannis, and R.E. Ellis. Computer-assisted hip resurfacing using individualized drill templates. 25(4):600–606, 2010.

[12] Hutmacher Dietmar W., Schantz Thorsten, Zein Iwan, Ng Kee Woei, Teoh Swee Hin, and Tan Kim Cheng. Mechanical properties and cell cultural response of polycaprolactone scaffolds designed and fabricated via fused deposition modeling. *Journal of Biomedical Materials Research*, 55(2):203–216, 2001.

[13] B. C. Tellis, J. A. Szivek, C. L. Bliss, D. S. Margolis, R. K. Vaidyanathan, and P. Calvert. Trabecular scaffolds created using micro ct guided fused deposition modeling. *Mater Sci Eng C Mater Biol Appl*, 28(1):171–178, 2009.

[14] F. Pati, T. Song, G. Rijal, J. Jang, S. Won Kim, and D. Cho. Ornamenting 3d printed scaffolds with cell-laid extracellular matrix for bone tissue regeneration. *Biomaterials*, 37:230–241, 2015.

[15] R.C. Marcove, V. Mike, J.V. Hajek, A.G., and R.V.P. Hutter. Osteogenic sarcoma under the age of twenty-one. *The Journal of Bone & Joint Surgery*, 52(3):411–423, 1970.

[16] A.J. Chou, E.S. Kleinerman, M.D. Krailo, Z. Chen, D. Betcher, J. Healey, E.U. Conrad, M.L. Nieder, M.A. Weiner, R.J. Wells, R.B. Womer, Paul A. Meyers, and on behalf of the Children's Oncology Group. Addition of muramyl tripeptide to chemotherapy for patients with newly diagnosed metastatic osteosarcoma. *Cancer*, 115(22):5339–5348, 2009.

[17] P Meyers et al. Osteosarcoma: A randomized, prospective trial of the addition of ifosfamide and/or muramyl tripeptide to cisplatin, doxorubicin, and high-dose methotrexate. *Journal of Clinical Oncology*, 23(9):2004–2011, 2005.

[18] A. Arkader, D. Viola, C. Morris, P. Boland, J. Patrick, and J. Healey. Coaxial extendible knee equalizes limb length in children with osteogenic sarcoma. *Clinical Orthopaedics and Related Research*, 459:60–65, 2007.

[19] D.R. Epari, W.R. Taylor, M.O. Heller, and G.N. Duda. Mechanical conditions in the initial phase of bone healing. *Clinical Biomechanics (Bristol, Avon)*, 21(6):646–55, 2006.

[20] C.A. Engh, J.D. Bobyn, and A.H. Glassman. Porous-coated hip replacement. the factors governing bone ingrowth, stress shielding, and clinical results. *The Journal of Bone & Joint Surgery*, 69(1):45–55, 1987.

[21] R. Hobbie and B.J. Roth. *Intermediate physics for medicine and biology*. Springer, 4th edition, 2007.

[22] M. Williams, H.R. Lissner, and B.F. LeVeau. *Williams and Lissner Biomechanics of human motion*. 2nd edition.

[23] S. Amornsamankul, B. Wiwatanapataphee, and K. Kaorapapong. Three-dimensional simulation of the femur bone using finite element method, 2010.

[24] J.J. Craig. *Introduction to Robotics*. Pearson, 3rd edition, 2005.

[25] G. R. Wilensky. Robotic surgery: An example of when newer is not always better but clearly more expensive. *The Milbank Quarterly*, 94(1):43–46, 2016.

[26] G. Dougherty. *Medical image processing : techniques and applications*. Springer, New York, 2011.

[27] G. Dougherty. Image analysis in medical imaging: recent advances in selected examples. *Biomed Imaging Interv J*, 6(3), 2010.

[28] R. M. Nishikawa, Y. Jiang, M. L. Giger, K. Doi, C. J. Vyborny, and R. A. Schmidt. Computer-aided detection of clustered microcalcifications, Oct 1992.

[29] V. Kraus, S. Feng, S. Wang, S. White, M. Ainslie, A. Brett, A. Holmes, and H. C. Charles. Trabecular morphometry by fractal signature analysis is a novel marker of osteoarthritis progression. *Arthritis and Rheumatism*, 60(12):3711–3722, 2009.

[30] Y. G. Wolf, M. Tillich, W.A. Lee, G. D. Rubin, T. J. Fogarty, and C. K. Zarins. Impact of aortoiliac tortuosity on endovascular repair of abdominal aortic aneurysms: Evaluation of 3d computer-based assessment. *Journal of Vascular Surgery*, 34(4):594 – 599, 2001.

[31] J. Cheung, D.J. Wever, A.G. Veldhuizen, J.P. Klein, B. Verdonck, R. Nijlunsing, J.C. Cool, and J.R. Van Horn. The reliability of quantitative analysis on digital images of the scoliotic spine. *European Spine Journal*, 11(6):535–542, 2002.

[32] R. Meder, S.K. de Visser, J.C. Bowden, T. Bostrom, and J.M. Pope. Diffusion tensor imaging of articular cartilage as a measure of tissue microstructure. *Osteoarthritis and Cartilage*, 14(9):875 – 881, 2006.

[33] B. Leukers et al. Hydroxyapatite scaffolds for bone tissue engineering made by 3d printing. *Journal of Materials Science: Materials in Medicine*, 16(12):1121–24, 2005.

[34] M.O. Wang et al. Evaluating 3d-printed biomaterials as scaffolds for vascularized bone tissue engineering. *Advance Materials*, 27(1):138–144, 2015.

[35] S. Wu, X. Liu, K. W.K. Yeung, C. Liu, and X. Yang. Biomimetic porous scaffolds for bone tissue engineering. *Materials Science and Engineering R*, 80:1–36, 2014.

[36] D. Komatsu, M. Hadjiargyrou, S. Udin, N. Trasolini, and S. Pentyala. Identification and characterization of a synthetic osteogenic peptide. *Calcified Tissue International*, pages 1–13, 2015.

[37] H.C. Tenenbaum, M. Torontali, and B. Sukhu. Effects of bisphosphonates and inorganic pyrophosphate on osteogenesis in vitro. *Bone*, 13(3):249–255, 1992.

[38] R.T. Franceschi, B.S. Iyer, and Y. Cui. Effects of ascorbic acid on collagen matrix formation and osteoblast differentiation in murine mc3t3-e1 cells. *Journal of Bone and Mineral Research*, 9(6):843–854, 1994.

[39] P. Orcel, H. Tajima, Y. Murayama, T. Fujita, S.M. Krane, E. Ogata, S.R. Goldring, and T. Nishimoto. Multiple domains interacting with gs in the porcine calcitonin receptor. *Molecular Endocrinology*, 14(1):170–182, 2000.

[40] R. Civitelli. Cell–cell communication in the osteoblast/osteocyte lineage. *Archives of biochemistry and biophysics*, 473(2):188–192, 2008.

[41] M. Pondel. Calcitonin and calcitonin receptors: bone and beyond. *International journal of experimental pathology*, 81(6):405–422, 2000.

[42] M. Zaidi. Skeletal remodeling in health and disease. *Nature medicine*, 13(7):791–801, 2007.

[43] R.R. Cline and M.M. Worley. Osteoporosis health beliefs and self-care behaviors: an exploratory investigation. *Journal of the American Pharmacists Association*, 46(3):356–363, 2006.

[44] K.P. Mishra. *Radiobiology and Biomedical Research*. Narosa Publishing House, 2004.

[45] B. Hoyer, A. Bernhardt, S. Heinemann, I. Stachel, M. Meyers, and M. Gelinsky. Biomimetically mineralized salmon collagen scaffolds for application in bone tissue engineering. *Biomacromolecules*, 13(4):1059–1066, 2012.

[46] K.H. Wlodarski, P.K. Wlodarski, and R. Galus. Bioactive composites for bone regeneration. review. *Ortopedia, traumatologia, rehabilitacja*, 10(6):201–210, 2012.

[47] S.C. Cowin and S.B Doty. *Tissue Mechanics*. Springer, 2nd edition, 2007.

[48] ISO 604. Plastics - determination of compressive properties, 2002.